

CENTRO DE CIÊNCIAS EXATAS E DE TECNOLOGIA
DEPARTAMENTO DE QUÍMICA

UNIVERSIDADE FEDERAL DE SÃO CARLOS

PROGRAMA DE PÓS-GRADUAÇÃO EM QUÍMICA

**“EMPREGO DE AGENTE COMPLEXANTE E
IRRADIAÇÕES POR FEIXE DE ELÉTRONS E LASER
FEMTOSEGUNDOS COMO ESTRATÉGIAS PARA
ALTERAÇÕES DA PROPRIEDADE
FOTOLUMINESCENTE DO α -Ag₂WO₄”**

Lílian Cruz Santos*

Tese apresentada como parte dos requisitos para obtenção do título de DOUTORA EM CIÊNCIAS, área de concentração: QUÍMICA.

Orientador: Prof. Dr. Elson Longo

*** bolsista CNPq**

**São Carlos - SP
2023**



UNIVERSIDADE FEDERAL DE SÃO CARLOS

Centro de Ciências Exatas e de Tecnologia
Programa de Pós-Graduação em Química

Folha de Aprovação

Defesa de Tese de Doutorado da candidata Lílian Cruz Santos, realizada em 22/06/2023.

Comissão Julgadora:

Prof. Dr. Elson Longo da Silva (UFSCar)

Prof. Dr. Juan Manuel Andrés Bort (UJI/Espanha)

Prof. Dr. Mário Lúcio Moreira (UFPEl)

Prof. Dr. Miguel Ángel San-Miguel Barrera (UNICAMP)

Prof. Dr. Miguel Adolfo Ponce (U del Mar)

O Relatório de Defesa assinado pelos membros da Comissão Julgadora encontra-se arquivado junto ao Programa de Pós-Graduação em Química.

Dedicatória

Dedico este trabalho:

À Rute minha mãe querida e
aos meus irmãos
Jéssica e Jonatã.

“Suba o primeiro degrau com fé. Não é necessário que você veja
toda a escada. Apenas dê o primeiro passo”

Martin Luther King

Agradecimentos

Ao Dr. Elson Longo, pela orientação, ensinamentos, confiança, paciência, amizade e todo incentivo dado.

Ao Liec por toda estrutura fornecida para a realização deste trabalho, e ao Corpo de Suporte à Pesquisa, em especial Rorivaldo Camargo, Sandra Belline, Daniela Caceta e Luma Garcia.

Ao Programa de Pós-Graduação em Química da Universidade Federal de São Carlos (PPGQ-UFSCar), pela oportunidade de cursar o doutorado.

Ao Conselho Nacional de Desenvolvimento Científico e Tecnológico - CNPq pela bolsa de estudos concedida.

A todos os componentes do grupo de pesquisa, em especial Mayara Mondego, Vinicius Teodoro e Letícia Laier pela ajuda e amizade.

À Rute, minha mãe, à Jéssica e ao Jonatã, meus irmãos, e familiares por todo amor, apoio e confiança.

Lista de Tabelas

Table 2.1 Identification of α -Ag ₂ WO ₄ samples and variation of reaction conditions.....	16
Table 2.2 Lattice parameters and unit cell volumes obtained by Rietveld refinement for the α -Ag ₂ WO ₄ samples.....	20
Table 2.3 Surface energy values (E_{surf} , J m ⁻²), the contribution of the surface area by the total area (C_i , %), and the polyhedron energy (E_{poly} , J m ⁻²) of each intermediate morphology to obtain the WE0.5 sample (α -Ag ₂ WO ₄).....	33
Table 3.1 Calculated density broken bond (nm ⁻²), surface energy (E_{surf} , Jm ⁻²), surface band gap (E_{gap}^{surf} , eV), percentage of contribution of each surface in the total area (% C_i) and polyhedron band gap energy for the morphologies of α -Ag ₂ WO ₄	52
Table A.1 Statistical parameters obtained by Rietveld refinement of the Ag/ α -Ag ₂ WO ₄ samples.....	81
Table A.2 Bond angles of [AgO _y] (Card ICSD n0. 4165)1, 2, 3.....	81
Table A.3 Bond angles of [WO ₆] (Card ICSD n0. 4165)1, 2, 3.....	83
Table A.4 Peak locations relative to the α -Ag ₂ WO ₄ micro-Raman spectroscopy analysis.....	84
Table B.1 Rietveld refinement and unit cell parameters of CP, MAH, EI, and FI samples.[a].....	93
Table B.2 Ag–O bond distances (Å) on the [Ag(6)O2], [Ag(4)O4], [Ag(5)O4], [Ag(3)O6], and [WO6] clusters.....	94
Table B.3 Theoretical and Experimental Raman modes (in cm ⁻¹) of α -Ag ₂ WO ₄ , compared to the literature.....	97
Table B.4 CIE chromaticity coordinates x and y for the CP, MAH, EI, and FI samples.....	100

Lista de Figuras

Figure 2.1 XRD patterns of the α -Ag ₂ WO ₄ samples synthesized by the MAH method.....	19
Figure 2.2 XPS spectra for the α -Ag ₂ WO ₄ samples. (a) survey spectra, b), Ag 3d, c) AgM ₄ N ₄₅ N ₄₅ , d) O 1s and e) W 4f core level spectra.....	23
Figure 2.3 a) W-L1 edge XANES spectra of the α -Ag ₂ WO ₄ samples and b) XANES spectra of the WE0.5 and the reference samples (Na ₂ WO ₄ , m-WO ₃ and WO ₂).....	24
Figure 2.4 Raman spectra of the α -Ag ₂ WO ₄ samples synthesized via the MAH method.....	26
Figure 2.5 FE-SEM Micrographs of the α -Ag ₂ WO ₄ microcrystals synthesized via the MAH method. The inset shows the FE-SEM images at low magnifications. A) W, b) WE0.25 and c) WE0.5.....	26
Figure 2.6 Distribution of the α -Ag ₂ WO ₄ particle sizes: a) W, b) WE0.25 and c) WE0.5.....	27
Figure 2.7 HR-TEM image of the a) WE0.25 sample and magnified regions corresponding to α -Ag ₂ WO ₄ (b–e) and to Ag NPs (f and g).....	27
Figure 2.8. Deconvolution of PL spectra. (Insets) The percentage of the color area corresponds to the emission peak of microcrystals a) W, b) WE0.25, c) WE0.5 and d) the CIE chromaticity diagram of α -Ag ₂ WO ₄ samples.....	36
Figure 2.9 a) Photocatalytic activities of samples in degradation of RhB under ultra-violet light irradiation, and b) corresponding plot of $-\ln(C/C_0)$ versus time.....	38
Figure 3.1 Scheme with steps of a) Synthesis by CP method, b) Treatment by MAH method, c) Electron beam irradiation, and d) Femtosecond laser irradiation; to obtain α -Ag ₂ WO ₄ samples.....	47
Figure 3.2 FE-SEM images of α -Ag ₂ WO ₄ particles of MAH, EI, and FI. (a-e) heterogeneous morphology obtained after treatment with MAH at different treatment times (2, 4, 8, 16, and 32 min) with the cubes highlighted in orange color and the rods-like in blue color; (f-j) rods-like with homogeneous morphology after EI indicated by green color; (k-o) heterogeneous morphology	

of rods in violet color and spheres in yellow color after FI.....	49
Figure 3.3 Wulff construction for α -Ag ₂ WO ₄ . For comparison, experimental FE-SEM images are shown. E_{surf} values are given in Jm^{-2}	51
Figure 3.4 a) EDS elemental mapping of the FI-8 sample of Si K α , O K α , W L α , and Ag L α . b) FI-8 sample analyzed by EDS, highlighting the rod- and sphere-like morphologies. c) Rod-like region 1 and d) Sphere-like region 2.....	54
Figure 3.5 The geometry of a) <i>opt</i> - α -Ag ₂ WO ₄ , b) CP, and c) irradiated (MAH-8, EI-8, and FI-8) structures.....	57
Figure 3.6 High-resolution XPS spectra of O 1s for the MAH-8, EI-8, and FI-8 samples.....	59
Figure 3.7 Partial density of states projected on the 4 <i>d</i> , 5 <i>d</i> , and 2 <i>p</i> orbitals of Ag, W, and O atoms, respectively, for a) <i>opt</i> - α -Ag ₂ WO ₄ , b) CP, and c) irradiated (MAH-8, EI-8, and FI-8) samples.....	62
Figure 3.8 PL spectra of the samples obtained by a) the CP method, treated with MAH, and irradiated by b) EI and c) FI.....	63
Figure 3.9 The total density of states for the (010), (100), (001), (011), (101), and (110) surfaces of α -Ag ₂ WO ₄	65
Figure 3.10 (a) PL spectra and maximum emission centers of the CP, MAH-8, EI-8, and FI-8 samples. (b) Comparative diagram of the band gap value of the optimized structure (3.42 eV) and band gap values for (100), (010), (001), and (101) surfaces.....	66
Figure A.1 Rietveld refinement plot of α -Ag ₂ WO ₄ samples prepared by the MAH method: a) W, b) WE0.25 and c) WE0.5.....	80
Figure A.2 TEM images of samples exposed to a 200 kV electron beam. a, b) W; c, d) WE0.25 and e, f) WE0.5.....	87
Figure A.3 Low-resolution TEM analysis of the WE0.5 sample of the α -Ag ₂ WO ₄ and Ag NPs at a) at time zero and b) 10 seconds later.....	88
Figure B.1 Micrograph of the CP sample obtained by the CP method.....	92
Figure B.2 High-resolution XPS spectra of a) Ag3 <i>d</i> and b) W 4 <i>f</i> of the α -Ag ₂ WO ₄ samples obtained by the MAH method in the synthesis time of 8 min	

(MAH-8), and treated by electron irradiated (EI-8) and femtosecond laser irradiated (FI-8).....	95
Figure B.3 Raman spectra of the α -Ag ₂ WO ₄ samples obtained by a) CP method and treated by b) MAH method and irradiated by c) EI and d) FI. e) Comparison the theoretical and experimental Raman mode.....	96
Figure B.4 XANES spectra W L ₁ -edge of the samples a) CP, MAH, EI, FI, and b) MAH-2 sample and patterns (Na ₂ WO ₄ , WO ₂ , and m-WO ₃).....	98
Figure B.5 UV-vis diffused reflectance spectroscopy of the α -Ag ₂ WO ₄ samples obtained by a) CP sample and treated by b) MAH method and irradiated by c) EI, and d) FI.....	99
Figure B.6 CIE chromaticity diagram at the sample obtained by a) CP method and treated by MAH method at the times: 2, 4, 8, 16, and 32 min, and irradiated by b) EI, and c) FI.....	100

Lista de Esquemas

Scheme 2.1 Schematic representation of the crystalline unit cell of α -Ag ₂ WO ₄ (bulk).....	21
Scheme 2.2 Schematic representation of the angular deviation of [AgO _y] (y = 2, 4, 6 e 7) and [WO ₆] clusters.....	22
Scheme 2.3 Schematic illustration of the proposed growth mechanism leading to the formation of α -Ag ₂ WO ₄ samples: a) WE0.25 and b) WE0.5.....	30
Scheme 2.4 Crystallographic structure and morphologies of the WE0.5 sample, with crystal planes (101), (100), (001), (110), (010), and (011). Surface energy is in Jm^{-2} . Experimental FE-SEM images of the WE0.5 samples obtained at different times of the MAH method are included for comparison.....	32
Scheme 2.5 Schematic representation of the energy profile to obtain the WE0.5 morphology. The intermediate morphologies are indicated as A - D, obtained by variations the E _{surf} values.....	34

Resumo

EMPREGO DE AGENTE COMPLEXANTE E IRRADIAÇÕES POR FEIXE DE ELÉTRON E LASER FEMTOSEGUNDOS COMO ESTRATÉGIAS PARA ALTERAÇÕES DA PROPRIEDADE FOTOLUMINESCENTE DO α -Ag₂WO₄. A descoberta da fotoluminescência a temperatura ambiente impulsionou o desenvolvimento de diversos aparelhos óptico-eletrônicos, motivou a busca por novos materiais fotoluminescentes e estimulou a modelagem dessa propriedade, mediante uma série de alterações no meio sintético. Devido à sua intrínseca fotoluminescência, o alfa-tungstato de prata (α -Ag₂WO₄), tem sido extensivamente estudado com o intuito de melhorar e modificar o seu emprego em dispositivos eletrônicos. As alterações morfológicas, estruturais, e também, a formação de heteroestruturas entre semicondutores e nanopartículas metálicas, têm se mostrado eficientes no modelamento e melhoramento da fotoluminescência. Desta forma, este estudo tem como principal objetivo a formação de heteroestruturas constituídas por microcristais de α -Ag₂WO₄ e nanopartículas de Ag, modificação morfológica e estrutural do α -Ag₂WO₄. As nanopartículas de prata foram obtidas por 3 vias: 1) método químico, no qual empregou-se o etilenodiamino que atuou como complexante, modelador da morfologia e redutor do cátion Ag⁺, 2) irradiação por feixe de elétrons e 3) irradiação por laser femtosegundos. Como resultados destacamos, o êxito na modelagem estrutural, morfológica e fotoluminescente, a partir das estratégias utilizadas. Foi elucidado o mecanismo de crescimento de partículas em meio contendo etilenodiamino e discutiu-se a influência da morfologia, do band gap superficial e da microestrutura sobre a fotoluminescência, frente à ação das irradiações empregadas. Ao utilizar etilenodiamino na síntese de α -Ag₂WO₄, observou-se uma relação direta entre concentração de etilenodiamino e quantidade de nanopartículas de prata superficiais. E como consequência da densidade eletrônica das superfícies que constituem cada morfologia e dos defeitos estruturais, observamos centros de emissão fotoluminescente diferentes ao empregar as estratégias selecionadas.

Abstract

EMPLOYMENT OF COMPLEXING AGENT AND IRRADIATION BY ELECTRON BEAM AND FEMTOSECOND LASER AS STRATEGIES FOR CHANGING THE PHOTOLUMINESCENT PROPERTY OF α -Ag₂WO₄. The discovery of room temperature photoluminescence has driven the development of various optical-electronic devices, motivated the search for new photoluminescent materials, and stimulated the modeling of this property through series of changes in synthesis medium. Due to its intrinsic photoluminescence, alpha-silver tungstate (α -Ag₂WO₄) has been extensively studied with the aim of improving and modifying its use in electronic devices. Morphological and structural modifications, as well as the formation of heterostructures between semiconductors and metallic nanoparticles have been shown to be efficient in photoluminescence modeling and enhancement. Thus, this study aimed at the formation of heterostructures composed of microcrystals of α -Ag₂WO₄ and Ag nanoparticles, and the morphological and structural modifications of α -Ag₂WO₄. The silver nanoparticles were obtained by 3 methods: 1) chemical method, in which ethylenediamine was employed as a complexing agent, morphology controller and reducer of Ag⁺ cation, 2) electron beam irradiation and 3) femtosecond laser irradiation. As results the study highlights the successful structural, morphological and photoluminescence modeling based on the strategies used. The mechanism of particle growth in medium containing ethylenediamine was elucidated and the influence of morphology, surface band gap and microstructure on photoluminescence was discussed according to irradiations employed. Regarding ethylenediamine in the synthesis of α -Ag₂WO₄, a direct relationship between ethylenediamine concentration and amount of surface silver nanoparticles were observed. And as a consequence of the electronic density of the surfaces constituting each morphology and structural defects, different photoluminescent emission centers were observed for selected strategies.

Sumário

1 – Introduction	1
1.1 – Publications	8
1.2 – References	9
2 – Multi-dimensional architecture of Ag/α-Ag₂WO₄ crystals: insights into microstructural, morphological, and photoluminescence properties	12
2.1 – Introduction	13
2.2 – Experimental section	15
2.3 – Results and discussion	19
2.4 – Conclusions	38
2.5 – References	39
3 – α-Ag₂WO₄ under microwave, electron beam and femtosecond laser irradiations: Unveiling the relationship between morphology and photoluminescence emissions	42
3.1 – Introduction	43
3.2 – Experimental section	45
3.3 – Results and discussion	47
3.4 – Conclusions	68
3.5 – References	69
4 – Conclusions	77
Apêndice A Supplementary Information for Multi-dimensional architecture of Ag/α-Ag₂WO₄ crystals: insights into microstructural, morphological, and photoluminescence properties	78
A.1 - Characterizations	78
A.2 – References	87
Apêndice B Supplementary Information for α-Ag₂WO₄ under microwave, electron beam and femtosecond laser irradiations: Unveiling the relationship between morphology and photoluminescence emissions	90
B.1 - Characterizatons	90
B.2 – References	101

Capítulo 1

Introduction

The development of photoluminescent materials with superior performance is very important due to their use in various devices such as TVs, computers, calculators, LED screens and diodes. Photoluminescence spectroscopy is a powerful tool used to observe separation of photoinduced charge carriers, recombination processes in nanometric semiconductors and order/disorder in the short (2-5 Å) and medium (5-20 Å) ranges, typical of cluster distortions, surface defects, distortions of oxygen bonds, oxygen vacancies, surface states (MOTTA et al., 2009), (TEIXEIRA et al., 2012). Structural order/disorder affects the electronic and optical properties of materials, resulting in interesting technological applications. It is known that the more disordered the structure of a material, the greater the intensity of its photoluminescent emission. (ORHAN et al., 2005) However, an optimum emission is obtained when there is both order and disorder in the compound, thus causing a charge gradient, which contributes to the trapping of electrons and holes in the crystalline lattice. Accordingly, the reconfiguration of the crystal structure enables modulation of the photoluminescent property of ceramic solids. For this purpose, the structure of a material can be modified by varying synthesis conditions, doping, among other factors (ROCHA et al., 2016).

Photoluminescence occurs when a higher energy photon is absorbed with the emission of a lower energy photon. This phenomenon in materials is linked to structural and electronic properties, particle morphology and cluster organization. According to Blasse and Grabmaier, (BLASSE and GRABMAIER, 1994), a multilevel and multiphoton photoluminescence known as broadband, occurs when

relaxation after excitement follows several paths, involving additional energy states within the band gap of the material, resulting in several emission bands from different regions of the electromagnetic spectrum (ROCHA et al., 2016).

The multilevel process is typical of disordered materials at short and medium ranges since disorder promotes the orbital overlap of elements that form the material. When orbitals overlap, they generate intermediate energy levels in the forbidden band and a charge gradient in the unit cell, which allow the trapping of electrons, and forbidden radiative decay through several routes (ROCHA et al., 2016), (MOURA et al. al., 2013). It is a consensus that energy states farther from the valence or conduction bands produce lower energy emissions, and defects that cause this behavior are called deep defects. However, levels closer to the valence or conduction bands produce higher energy emissions, and this type of defect is called a shallow defect (SANTANA, de et al., 2014), (SOUZA et al., 2016).

Silver tungstate (Ag_2WO_4) has three polymorphs that are synthesized by controlling synthesis temperature and pressure: α - Ag_2WO_4 , β - Ag_2WO_4 and γ - Ag_2WO_4 with orthorhombic, hexagonal and cubic structure, respectively (BASTOS et al., 2022). α - Ag_2WO_4 is thermodynamically stable and has several applications highlighted as follows: bactericidal and antimicrobial agent, catalyst, sensor, photoluminescent material, electrocatalyst, photocatalyst and dye adsorbent (PINATTI et al., 2019), (ABREU et al., 2022), (ADIB et al., 2021). The crystalline lattice of silver tungstate in the orthorhombic form presents distorted octahedral tungsten clusters [WO_6] and silver clusters [AgO_x] ($x = 2, 4, 6$ and 7): distorted deltahedral [AgO_7], distorted octahedral [AgO_6], distorted tetrahedral [AgO_4] and angular [AgO_2]. The heterogeneity of the crystal lattice and its associated anisotropy are responsible for the multifunctionality of α - Ag_2WO_4 (CAVALCANTE et al., 2012).

Several methods have been employed to prepare α - Ag_2WO_4 , such as chemical precipitation, (SREEDEVI et al., 2015) conventional hydrothermal method, (YU et al., 2003) microwave-assisted

hydrothermal method, (SILVA, et al., 2016) simple ion exchange, (WANG et al., 2019) sonochemical method, (XAVIER et al., 2019) among others. In addition to the methodology employed, factors controlled in the synthesis methods such as: time, temperature and reaction pH, presence and concentration of organic ligands, source and concentration of lattice former and modifier, solvent, ionic strength, among others, directly affects the lattice structure, morphology, particle size, and other properties. Neto and collaborators synthesized α -Ag₂WO₄ using chemical precipitation, polyvinylpyrrolidone as a surfactant and different reaction temperatures. They observed that higher temperatures resulted in elongated nanorods with a change in cross-section from hexagonal to square, and the particles presented surface irregularities. They also found that photocatalytic activity against methylene blue dye improved, and attributed the performance to the change in morphology and increase in surface contact due to surface irregular. (ANDRADE NETO et al., 2019)

On the surfaces, some clusters, which constitute the crystalline lattice, are sub-coordinated, that is, the expected number of oxygen atoms around the cation is reduced. Thus, considering that each surface can present a different number of broken bonds, then each surface can also present an electronic density different from the average value measured experimentally. (GOUVEIA et al., 2022), (LAIER et al., 2020) Therefore, a material whose surface (a higher proportion) has high electronic density, that is, a particle with a certain morphology, will present different performances for a desired application. Roca and colleagues synthesized α -Ag₂WO₄ using a microwave-assisted hydrothermal method which involved the variation of temperature and the use of sodium dodecyl sulfate as surfactant. They observed a variation in the exposed faces of the phase according to change in temperature and a dependence of photocatalytic activity on the predominantly exposed faces. This dependence was related to the presence of unsaturated Ag and W sites with affinity for H₂O, O₂ and OH* and O₂H* radicals. Therefore, these photocatalytic activities are closely related to the organization of atoms on the surface of the

particles and the proportion of the active surface according to the morphology of the material. (ROCA et al., 2015)

One of the strategies used to favor the growth of specific surfaces is the use of complexing agents, which are known to: a) bind to cationic ions, thus control nucleation, and consequently the size of the particles; (RIBEIRO et al., 2022) b) they preferentially bind to certain crystalline faces due to the affinity of functional groups to molecules present on that surface, thus influencing the morphology of particles (DING et al., 2018) and c) in some cases, they reduce cationic ions, forming, for example, metallic nanoparticles (RAJESH et al., 2016). Ribeiro and collaborators synthesized α -Ag₂WO₄ with different morphologies and particle sizes via a sonochemical method with different complexing agents. These researchers also observed improved photocatalytic activity when employing citric acid in the reaction medium, due to particle size reduction. (RIBEIRO et al., 2022). Wang and researchers used the mirror silver reaction and the complexant ethylenediamine to deposit and control silver nanoparticles on the surface of TiO₂ nanocrystals. The Ag-TiO₂ system showed excellent catalytic activity for the reduction of p-nitrophenol. (WANG et al., 2017)

In order to modify the properties of materials, several ligands have been used. Among them, one can cite: ethylenediamine (WANG et al., 2017), citric acid (MAIA, ASSAF and ASSAF, 2012), ethylenediaminetetraacetic acid (MO et al., 2022), cetyltrimethylammonium bromide (LAI et al., 2014) and polyvinylpyrrolidone (SEO et al., 2019).

Metallic nanoparticles combined with semiconductors result in materials with optimized properties due to synergistic effects, metal-semiconductor coupling and interfacial structure. In addition, the physical-chemical properties of the individual components contribute to improved properties. (LV, DUAN and WANG, 2020) Metal-semiconductor systems can be applied in: catalysis, photocatalysis, electrocatalysis, solar cells and energy storage. (LV, DUAN and WANG, 2020) The combination with noble metal particles adds several benefits as regards material properties such as: active sites, electronic traps and plasmonic

surface resonance. (LIAO, NEHL and HAFNER, 2006) Semiconductors containing silver nanoparticles have been extensively studied because they present multiple functionalities in areas such as bactericidal applications, bioimaging, sensing, photocatalysis, optics, etc. (LOU et al., 2017), (HUANG et al., 2017), (FENG et al., 2018) As mentioned in the previous paragraph, one of the possible alternatives for obtaining metallic nanoparticles are the use of complexing agents with a reducing effect. Other recurrent pathways are electron beam and femtosecond laser irradiation, which act by propelling internal atoms to the surface and subsequent production of nanoparticles on the surface of the material, metal/semiconductor interface and internal metallic vacancies. (ASSIS et al., 2020), (ASSIS et al., 2018) Longo and colleagues synthesized α -Ag₂WO₄ by microwave-assisted hydrothermal method, using the surfactant polyvinylpyrrolidone, after which the as-synthesized sample was subjected to electron irradiation. They observed: 1) the growth of silver on the surface of α -Ag₂WO₄, 2) structural and electronic disorder caused by the electron beam, and 3) improved antimicrobial activity. (LONGO et al., 2014) Using femtosecond laser as a source of irradiation, Assis and collaborators also grew Ag on the surface of α -Ag₂WO₄ crystals and observed an improvement in bactericidal activity. (ASSIS et al., 2018)

Concerning the strategies that can be used to change the properties of materials, we highlight the microwave-assisted hydrothermal method, whose advantages are: thermal gradient elimination, direct, quick and selective heating of the reaction system, increased productivity and selectivity of the synthesis, resulting in particles with homogeneous morphologies and narrow size distribution (LIU et al., 2022), (SIVASUBRAMANIAN et al., 2022). The heating mode is a result of the direct interaction between the dipole moments of polar substances (solvent, precursors and ions) and alternating electromagnetic field of microwave irradiation that produces rotations and collisions of the substances contained in the reaction medium and ionic conduction. (CHEN et al., 2022), (SIVASUBRAMANIAN et al., 2022), (KUMARI et al., 2022) It is important to note that only dipolar or

charge-carrying substances are capable of absorbing and converting microwave radiation into heat.(LIU et al., 2022), (BECERRA-PANIAGUA et al., 2022) Using the microwave hydrothermal method, L. O. Laier obtained α -Ag₂WO₄ microrods and observed that the time of exposure to microwave radiation modified the surface areas of the particles, generating density of broken bonds, which can function as an active site in catalyzed reactions.(LAIER et al., 2020)

To reduce non-radiative transition and thus improve emissive transition, a low phonon energy is necessary. This characteristic is typical of tungstates, which are considered self-activated phosphors because of [WO₆] clusters that efficiently transfer energy within the lattice through charge transfer from O to W.(THONGTEM, PHURUANGRAT and THONGTEM, 2008), (KAUR et al., 2020), (HUANGFU et al., 2022) The charge transfer transition in [WO₆] clusters and intrinsic defects produce two bands in the photoluminescence spectra: one in the blue-violet and the other in the yellow-green regions, respectively. The higher energy emission of silver tungstates is associated with the electronic transitions that occur between the hybridized Ag 4d and O 2p orbitals, which form the valence band, and the delocalized s and p orbitals of the W 5d conduction band. Cavalcante and colleagues synthesized α -Ag₂WO₄ by three methods and observed an increase in photoluminescence intensity associated with higher structural disorder of the lattice. (CAVALCANTE et al., 2012) Through chemical precipitation, Sreedevi and collaborators obtained α -Ag₂WO₄ and calcined the same for 3h, at 500, 550 and 600 °C. They found an increase in photoluminescent intensity with an increase in calcination temperature. This effect was also associated with an increase in structural defects. (SREEDEVI et al., 2015)

In this context, the objective of this work was to investigate and relate the structural, morphological and optical properties of the Ag/ α -Ag₂WO₄ system, varying the method of obtaining silver nanoparticles. The highlights of the study were the synthesis of multidimensional particles using ethylenediamine as a complexing agent, the modulation of photoluminescent emission and the correlation shown between

photoluminescence and particle surface, corroborated by theoretical calculations.

1.1 - Publications

Thesis Publication

1 - Lillian Cruz, Mayara M. Teixeira, Vinícius Teodoro, Natalia Jacomaci, Leticia O. Laier, Marcelo Assis, Nadia G. Macedo, Ana C. M. Tello, Luís F. da Silva, Gilmar E. Marques, Maria A. Zaghete, Márcio D. Teodoro and Elson Longo. Multi-dimensional architecture of Ag/ α -Ag₂WO₄ crystals: insights into microstructural, morphological, and photoluminescence properties. *CrystEngComm*, 2020, 22, 7903-7917.

2 - Mayara Mondego Teixeira, Lillian Cruz Santos, Ana Cristina Mora Tello, Priscila Barros Almeida, Jussara Soares da Silva, Leticia Laier, Lourdes Gracia, Marcio Daldin Teodoro, Luís Fernando da Silva, Juan Andrés, and Elson Longo. α -Ag₂WO₄ under microwave, electron beam and femtosecond laser irradiations: Unveiling the relationship between morphology and photoluminescence emissions. *J. Alloys Compd*, 2022, 903, 163840.

1.2 - References

- ANDRADE NETO, N. F. et al. Effect of temperature on the morphology and optical properties of Ag_2WO_4 obtained by the co-precipitation method: Photocatalytic activity. **Ceramics International**, v. 45, n. 12, p. 15205–15212, 2019.
- ASSIS, M. et al. Towards the scale-up of the formation of nanoparticles on $\alpha\text{-Ag}_2\text{WO}_4$ with bactericidal properties by femtosecond laser irradiation. **Scientific Reports**, v. 8, n. 1, p. 1–11, 2018.
- ASSIS, M. et al. Unconventional Magnetization Generated from Electron Beam and Femtosecond Irradiation on $\alpha\text{-Ag}_2\text{WO}_4$: A Quantum Chemical Investigation. **ACS Omega**, 5, 10052–10067, 2020.
- BECERRA-PANIAGUA, D. K. et al. Nanostructured metal sulphides synthesized by microwave-assisted heating: a review. **Journal of Materials Science: Materials in Electronics**, v. 33, n. 29, p. 22631–22667, 2022.
- CAVALCANTE, L. S. et al. Cluster Coordination and Photoluminescence Properties of $\alpha\text{-Ag}_2\text{WO}_4$ Microcrystals. **Inorganic Chemistry**, v. 51, n. 20, p. 10675–10687, 2012.
- CHEN, L. et al. Facile Access to Fabricate Carbon Dots and Perspective of Large-Scale Applications. **Small**, 2206671, 2022.
- DING, J. et al. Controlled synthesis of CeVO_4 hierarchical hollow microspheres with tunable hollowness and their efficient photocatalytic activity. **CrystEngComm**, v. 20, n. 31, p. 4499–4505, 2018.
- FENG, J. et al. Hydrothermal Cation Exchange Enabled Gradual Evolution of Au@ZnS-AgAuS Yolk-Shell Nanocrystals and Their Visible Light Photocatalytic Applications. **Advanced Science**, v. 5, n. 1, p. 1–7, 2018.
- GOUVEIA, A. F. et al. Ag_2WO_4 as a multifunctional material: fundamentals and progress of an extraordinarily versatile semiconductor. **Journal of Materials Research and Technology**, 21, p. 4023–4051, 2022.
- HUANG, S. et al. Synergistically Enhanced Electrochemical Performance of $\text{Ni}_3\text{S}_4\text{-PtX}$ (X = Fe, Ni) Heteronanorods as Heterogeneous Catalysts in Dye-Sensitized Solar Cells. **ACS Applied Materials and Interfaces**, v. 9, n. 33, p. 27607–27617, 2017.
- HUANGFU, Z. et al. Comparative analysis of the emission of Eu^{3+} doped in α - and β - Ag_2WO_4 . **Journal of Molecular Structure**, v. 1269, p. 133734, 2022.
- KAUR, P. et al. Structural and optical characterization of Eu and Dy doped CaWO_4 nanoparticles for white light emission. **Journal of Alloys and Compounds**, v. 834, p. 154804, 2020.
- KUMARI, N. et al. Zirconia-based nanomaterials: recent developments in synthesis and applications. **Nanoscale Advances**, v.4, n. 20, p. 4210–4236, 2022. Falta o volume
- LAI, H. et al. CTAB assisted hydrothermal preparation of $\text{YPO}_4\text{:Tb}^{3+}$ with controlled morphology, structure and enhanced photoluminescence. **Materials Science and Engineering B: Solid-State Materials for Advanced Technology**, v. 179, n. 1, p. 66–70,

2014.

LAIER, L. O. et al. Surface-dependent properties of α - Ag_2WO_4 : a joint experimental and theoretical investigation. **Theoretical Chemistry Accounts**, v. 139, n. 7, p. 1–11, 2020.

LIAO, H.; NEHL, C. L.; HAFNER, J. H. Biomedical applications of plasmon resonant metal nanoparticles. **Nanomedicine**, v. 1, n. 2, p. 201–208, 2006.

LIU, L. et al. Solvothermal synthesis of zirconia nanomaterials: Latest developments and future. **Ceramics International**, v. 48, n. 22, p. 32649–32676, 2022.

LONGO, V. M. et al. Potentiated electron transference in α - Ag_2WO_4 microcrystals with Ag nanofilaments as microbial agent. **Journal of Physical Chemistry A**, v. 118, n. 31, p. 5769–5778, 2014.

LOU, Y. et al. Application of $\text{Cu}_3\text{InSnSe}_5$ Heteronanostructures as Counter Electrodes for Dye-Sensitized Solar Cells. **ACS Applied Materials and Interfaces**, v. 9, n. 21, p. 18046–18053, 2017.

LV, Y.; DUAN, S.; WANG, R. Structure design, controllable synthesis, and application of metal-semiconductor heterostructure nanoparticles. **Progress in Natural Science: Materials International**, v. 30, n. 1, p. 1–12, 2020.

MAIA, T. A.; ASSAF, J. M.; ASSAF, E. M. Steam reforming of ethanol for hydrogen production on $\text{Co}/\text{CeO}_2\text{-ZrO}_2$ catalysts prepared by polymerization method. **Materials Chemistry and Physics**, v. 132, n. 2–3, p. 1029–1034, 2012.

MO, Y. et al. In-situ constructing and EDTA-enhancing of meta-aluminate passivation films on electroplated zinc surfaces. **Colloids and Surfaces A: Physicochemical and Engineering Aspects**, v. 657, n. PA, p. 130573, 2022.

RAJESH, K. M. et al. Synthesis of copper nanoparticles and role of pH on particle size control. **Materials Today: Proceedings**, v. 3, n. 6, p. 1985–1991, 2016.

RIBEIRO, L. K. et al. Tug-of-War Driven by the Structure of Carboxylic Acids: Tuning the Size, Morphology, and Photocatalytic Activity of α - Ag_2WO_4 . **Nanomaterials**, v. 12, n. 19, p. 1–12, 2022.

ROCA, R. A. et al. Facet-dependent photocatalytic and antibacterial properties of α - Ag_2WO_4 crystals: combining experimental data and theoretical insights. **Catalysis Science and Technology**, v. 5, n. 8, p. 4091–4107, 2015.

SEO, K. et al. Polyvinylpyrrolidone (PVP) Effects on Iron Oxide Nanoparticle Formation. **Mater. Lett.** 215, 203–206, 2018.

SIVASUBRAMANIAN, P. D. et al. A review on bismuth-based nanocomposites for energy and environmental applications. **Chemosphere**, v. 307, n. P1, p. 135652, 2022.

SREEDEVI, A. et al. Chemical synthesis, structural characterization and optical properties of nanophase α - Ag_2WO_4 . **Indian Journal of Physics**, v. 89, n. 9, p. 889–897, 2015.

THONGTEM, T.; PHURUANGRAT, A.; THONGTEM, S. Characterization of MeWO_4 (Me = Ba, Sr and Ca) nanocrystallines prepared by sonochemical method. **Applied Surface Science**, v. 254, n. 23, p. 7581–7585, 2008.

XU, W. L. et al. Porous layered $\text{La}_{0.6}\text{Sr}_{0.4}\text{Co}_{0.2}\text{Fe}_{0.8}\text{O}_3$ perovskite with enhanced catalytic activities for oxygen reduction. **J. Cent. South Univ**, 28, p. 1305–1315, 2021.

WANG, X. et al. Highly active Ag-TiO₂ nanocomposite from atom deposition in ethylenediamine-complexing silver mirror reaction. **Journal of Nanoscience and Nanotechnology**, v. 17, n. 5, p. 3111–3116, 2017.

Capítulo 2

Multi-dimensional architecture of Ag/ α -Ag₂WO₄ crystals: insights into microstructural, morphological, and photoluminescence properties

Lílian Cruz,^{*a} Mayara M. Teixeira,^a Vinícius Teodoro,^a Natalia Jacomaci,^b Leticia O. Laier,^b Marcelo Assis,^a Nadia G. Macedo,^c Ana C. M. Tello,^a Luís F. da Silva,^d Gilmar E. Marques,^d Maria A. Zaghete,^b Márcio D. Teodoro^d and Elson Longo^{*a}

^aCenter of Development of Functional Materials, Federal University of São Carlos, Rod. Washington Luiz, km 235, 13565-905, São Carlos, SP, Brazil. E-mail: elson.liec@gmail.com.

^bInterdisciplinary laboratory of ceramic studies, São Paulo State University, 14800-900, Araraquara, SP, Brazil.

^cDepartment of Physical Chemistry, Institute of Chemistry, State University of Campinas, 13083-970, Campinas, SP, Brazil.

^dDepartment of Physics, Federal University of São Carlos, Rod. Washington Luiz, km 235, 13565-905, São Carlos, SP, Brazil.

ABSTRACT: In this study, we report the potential of ethylenediamine (En) in the modification of the morphological, structural, optical and catalytic properties of α -Ag₂WO₄ crystals decorated with Ag nanoparticles (Ag NPs). Experimental techniques were used to characterize the as-synthesized samples such as X-ray diffraction, Raman, electron microscopy, X-ray photoelectron spectroscopy, X-ray absorption spectroscopy, and photoluminescence spectroscopy. The results confirmed the efficiency of En in the decoration with the formation of Ag/ α -Ag₂WO₄ crystals and also the

modification of α -Ag₂WO₄ morphology that indicated its influence on the crystal growth mechanism via self-assembly and Ostwald ripening. En affects the degree of order/disorder of the crystalline structures in long and short-ranges. In addition, photoluminescence measurements revealed a blue shift of the optical emission caused by a reduction of oxygen vacancies and an increase in structural disorder due to the En concentration used in the synthesis processes. Regarding the photocatalysis experiments, the reduction in oxygen vacancies also caused a decrease in the photoactivity of α -Ag₂WO₄ against the rhodamine B dye, thus confirming the relevance of oxygen vacancies for the development of α -Ag₂WO₄ photocatalysts.

Keywords: Optical Properties, Photocatalytic Activity, Alpha-Ag₂WO₄, Tungstate, Silver, Ag, Microcrystals, Growth, Ions, Glasses

2.1 - Introduction

Material properties are determined based on various factors such as defects, particle size, morphology, crystal structure, and the combination of materials. Morphology is governed by surface anisotropic properties which, consequently, are controlled by growth and dissolution rates, wettability, surface energy, cohesion, adhesion, etc.¹ Several chemical synthesis methodologies have been applied to obtain compounds that exhibit distinct crystal shapes due to the direct relationship between the morphology of the materials, the physicochemical properties, and their functional applications.² This occurs because the morphology is directly linked to short-, medium-, and long-range crystal lattice ordering caused by the presence of reactive surfaces and the contact area, directly influencing the material properties.³ Such factors are controlled by the synthesis methodology; therefore, it is of great importance to understand the factors that are linked to the manifestation of a specific property to develop a suitable synthesis methodology.

In addition to their efforts to control morphology, many researchers have dedicated themselves to the development of multifunctional materials, through the suitable combination of their constituents. In particular, the combination of semiconductors with metallic nanoparticles, due to the catalytic and electronic characteristics that culminate in materials with

unique optical, magnetic, physicochemical, catalytic, and plasmonic properties. Silver-containing materials have been widely studied, due to their several applications, such as in antibacterial^{4,5} materials, bioimaging,⁶ sensors,⁷ heterogeneous catalysis,⁸⁻¹⁰ and optics.¹¹⁻¹³ As can be found in the work conducted by Barreca et al.,¹² silica-supported silver nanoparticles were obtained by radio frequency (rf) sputtering from Ar plasma, under soft conditions. The authors observed modifications in the optical properties of the material, such as increased absorption in the visible region, due to surface-plasmon resonance, widening of the band due to the increase in particle size and shape distribution, in addition to the red effect, caused by the particle coalescence. On another occasion, Barreca et al.¹³ used the same rf-sputtering method to prepare Ag–Au alloys supported on silica. They analyzed the control of the size, shape, structure, and dispersion of the particles and concluded that the control of reaction conditions and thermal treatment function makes it possible to fine-tune the optical properties.

Our research group has studied the silver tungstate (α -Ag₂WO₄) compound synthesized by different methodologies.^{14,15} Significant interest in α -Ag₂WO₄ has recently developed because it presents interesting applications for sensors,¹⁶ light-emitting diodes (LEDs),¹⁷ degradation of organic contaminants,¹⁸ and inhibition/destruction of pathogenic microorganisms.¹⁹ These applications depend on the method utilized to obtain the α -Ag₂WO₄ compound. Different methodologies have been used to synthesize α -Ag₂WO₄, such as coprecipitation (CP),¹⁶ the conventional hydrothermal (CH) method,²⁰ the microemulsion method,¹¹ and the microwave-assisted hydrothermal (MAH)²¹ method, among others.

To get decorated semiconductors, Koyappayil et al. synthesized Ag@Ag₂WO₄ nanorods via the hydrothermal route, using cetyltrimethylammonium bromide (CTAB) in the reaction medium. They observed an excellent ability to detect hydrogen peroxide and glucose.⁷ Meanwhile, Liu et al. obtained Ag₂WO₄ nanowires decorated with Ag NPs, but by the hydrothermal method followed by the chemical reduction process, verifying good semiconductor stability and improvement of the photoactivity in the visible region due to the high production of OH* radicals and the effects of plasmon resonance of the surface.²² Although these works present simple

methodologies for the preparation of Ag/Ag₂WO₄ crystals, few simple methods promote a suitable control of the morphological and structural properties of the semiconductor decorated with (or without) Ag NPs.

Recently, the modifier En has gained attention due to its bidentate complexing properties, which include high polarity, high chelating power, alkalinity, and the ability to act as a reducing agent.²³ In this study, we analyzed the synthesis of α -Ag₂WO₄ via the MAH method with two concentrations of the complexing agent, En, investigating its influence on short-, medium-, and long-range ordering, morphology, optical, and photocatalytic properties.

Also, the formation of Ag NPs on the surface of α -Ag₂WO₄ was verified due to the use of En in the synthesis, without additional processes. This manuscript addresses a strategy for obtaining multidimensional and functionalized architectures with metallic nanoparticles and also provides an understanding of the factors that fine-tune the optical and photocatalytic properties of α -Ag₂WO₄.

2.2 - Experimental section

Preparation of Ag/ α -Ag₂WO₄ crystals: In two separate beakers, a solution of 0.5 mmol of En (C₂H₈N₂, 99.8%, Sigma-Aldrich) and 2 mmol of silver nitrate (AgNO₃, 99.8%, Cennabras), dissolved in 10 mL of deionized water at room temperature, was prepared. Then, an AgNO₃ solution was added to the En solution and was continuously stirred for 1 h, yielding a brown suspension, which, after 15min, turned black. Separately, 1 mmol of sodium tungstate (Na₂WO₄·2H₂O, 99%, Stream Chemicals) was dissolved in 80 mL of deionized water, which was added to the mixture containing En and AgNO₃, resulting in an instantly formed white precipitate. This solution was continuously stirred for 10 min. The same procedure was followed for the second sample using 1 mmol instead of 0.5 mmol of En. The suspension obtained was transferred to a Teflon vessel (100 mL) and then treated in an MAH reactor at 160 °C for 32 min. The resultant black powder was centrifuged 3 times with acetone, 3 times with ethyl alcohol, 4 times with distilled water, and then dried at 60 °C for 12 h. The variations of the reaction conditions are

shown in **Table 2.1**. For the synthesis without En, the procedure was the same except AgNO_3 was dissolved in 20 mL of deionized water, and the powder obtained exhibited a light pink color. The samples were named W for the sample without En and WE0.25 and WE0.5 for the En/ Ag^+ ratios of 0.25 and 0.50, respectively.

To investigate the growth and formation of the morphology, the WE0.25 and WE0.5 syntheses were performed for the following time durations: 2, 4, 8, and 16 min. The 5 min time duration in WE0.5 was added because of a morphological change observed between 4 and 8 min.

Table 2.1 Identification of $\alpha\text{-Ag}_2\text{WO}_4$ samples and variation of reaction conditions.

Samples	n° mmol WO_4^{2-}	n° mmol Ag^+	n° mmol En*	En*/ Ag^+	[En*] mmol/L
W	1.0	2.0	0	0	0
WE0.25	1.0	2.0	0.5	0.25	5.0
WE0.5	1.0	2.0	1.0	0.50	10.0

Photocatalytic measurements: The photocatalytic activity of the as-synthesized samples was probed by quantifying the removal of rhodamine B (RhB; 95%, Mallinckrodt) dye in aqueous solution under UV irradiation. The samples (50 mg) were immersed in 50 mL of RhB solution (1×10^{-5} mol L^{-1}). Before illumination, the suspensions were sonicated for 5 min in an ultrasonic bath (Branson, model 1510; frequency 42 kHz), then stored in the dark for 30 min to allow for saturated adsorption of RhB onto the catalyst. The beaker was then placed in a photoreactor kept at 20 °C and illuminated by six UV lamps (TUV Phillips, 15 W, and maximum intensity of 254 nm). At 5 and 15 min intervals, an aliquot of 0.5 mL was removed and then centrifuged at 10 000 rpm for 2 min to remove the sample from the suspension. Finally, the removal of dye was monitored using a spectrometer (Jasco V-660) to measure, at 554 nm, the intensity of the RhB characteristic absorption peak.

Computational methods: The polyhedron energy, E_{poly} , was calculated using eqn (1), and the energy profile, which allows the connection of the ideal morphology with the final experimental morphology, was constructed.

$$E_{poly} = \sum C_i \cdot E_{surf}^{(hkl)} \quad (1)$$

where C_i is the percent contribution of the surface area to the total area of a polyhedron ($C_i = A^{(hkl)} / A^{(poly)}$) and $E_{surf}^{(hkl)}$ is the surface energy.²⁴

Characterization techniques: The X-ray powder diffraction technique (XRD) was employed to evaluate the crystalline structure in the long-range, the composition phase and the lattice parameters of the sample Ag/ α -Ag₂WO₄, using a diffractometer (Shimadzu, model XRD 6000) with Cu-K α radiation ($\lambda = 1.5406 \text{ \AA}$) in the 2θ range from 5° to 110° with a step of 0.02° and a scanning speed of $0.2^\circ \text{ min}^{-1}$. The Rietveld refinement method was employed to verify the bond angle, the quantitative analysis phase, and the lattice parameters.²⁵ Refinement calculations were performed using TOPAS Academic (v.5.4) software. The parameters refined were the scale factor, background (polynomial 6 terms), sample shift, crystal lattice, anisotropic peak broadening, preferential orientation, and isotropic thermal parameters. The background was corrected by the Chebyshev function with a polynomial of 10 terms. The peak profile was modeled by Finger et al.,²⁶ a function for the correction of peak asymmetry due to axial divergence. The anisotropic broadening of the sample was modeled using Stephens's model.²⁷ The weight fraction W_α of the crystalline phases present in the heterostructure Ag/ α -Ag₂WO₄ is estimated using Hill and Howard's²⁸ relationship:

$$W_\alpha = \frac{S_\alpha(ZMV)_\alpha}{\sum_{i=1}^n S_i(ZMV)_\alpha} \quad (2)$$

where n , S , Z , M and V are the number-phase in the sample, the scale factor, the number of formula units per unit cell, the mass of the formula unit and the unit-cell volume, respectively. Since all the phases are crystalline in the sample, α is the j value for a specific phase (Ag or Ag₂WO₄) among the total phase in the heterostructure.²⁸ In other words, the amount phase is relative and not absolute; for this reason, the structural quality of the sample in refinement is fundamental. The structural quality and the performance of the calculation are guaranteed by R_{wp} , which is the percentagem difference of the calculated intensity observed point by point; R_{exp} , which is the best

statistically expected value for R_{wp} ; Gof^2 (goodness of fit), which represents the ratio between R_{wp} and R_{exp} ; and R_{Bragg} , which indicates the quality of the refined structural model and also the good visual agreement between the adjustments made.^{25,29} The morphological properties were analyzed using field emission scanning electron microscopy, FE-SEM (Philips-FEIInspect F50) and transmission electron microscopy, TEM (FEI-Tecnai G2 F20 operating at 200 kV). High-resolution transmission electron microscopy (HRTEM) measurements were performed to investigate the planes and assign them to the possible phases present in the as-synthesized samples. Raman spectra were collected using an Ar ion laser (Horiba Jobin-Yvon iHR550, $\lambda = 514.5$ nm, 20 mW) as an excitation source, with a scanning range from 50 to 1100 cm^{-1} . Room-temperature photoluminescence (PL) measurements were performed using a 355 nm laser (Cobol/Zouk) as an excitation source focused on a 200 μm spot with a constant power of 5 mW. The luminescence signal was dispersed by a 19.3 cm spectrometer (Andor/Kymera) and detected by a Si charge-coupled device (Andor/Idus BU2). The electronic and local atomic structures around the tungsten atoms were probed using X-ray absorption near-edge structure (XANES). The W-L edge XANES spectra of the α - Ag_2WO_4 samples were collected at the XAFS2 beamline at the Brazilian Synchrotron Light Laboratory (LNLS). The XANES spectra were collected at the W-L1 edge in a transmission mode at room temperature. The spectra were recorded using energy steps of 1.0 eV before and after the edge, and 0.7 and 0.9 eV near the edge-region for the L1 edge. For the XANES analysis, the background was removed from all the spectra, and normalized using as the unit of measurement the first extended X-ray absorption fine structure (EXAFS) oscillation, using MAX software.³² The X-ray photoelectron spectroscopy, XPS, measurements were made using a Scienta Omicron ESCA+ with a monochromatic X-ray source (Al K α , $h\nu = 1486.7$ eV). Peak deconvolution was performed using a Voigt line shape with a Shirley nonlinear sigmoid-type baseline and all binding energies were calibrated with reference to the surface adventitious C 1s peak at 284.8 eV as an internal standard.

2.3 - Results and discussion

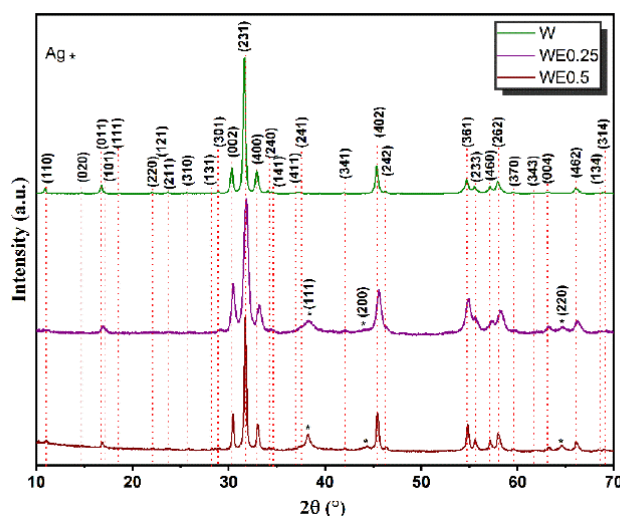


Figure 2.2 XRD patterns of the α - Ag_2WO_4 samples synthesized by the MAH method.

Figure 2.1 shows the XRD patterns of the α - Ag_2WO_4 powder prepared by the MAH method. The orthorhombic structure was confirmed in all patterns associated with α - Ag_2WO_4 (space group $\text{Pn}2\text{n}$), according to Inorganic Crystal Structure Database (ICSD) card no. 4165.^{3,30,33} The WE0.25 and WE0.5 samples also showed reflections at 38.20° , 44.40° , and 64.60° , which were indexed to crystallographic planes (111), (200), and (220), related to the cubic structure of metallic Ag (ICSD, card no. 64997).^{31,34} The lattice parameters of the samples estimated from the Rietveld refinement are presented in **Table 2.2**. As can be seen, the results are similar to those reported in previous studies,³⁰ and no significant variation between the samples was found. Furthermore, as a result of the use of En in the synthesis procedure, we observed the presence of two crystalline phases: α - Ag_2WO_4 and metallic Ag.

The obtained cell volumes of the W, WE0.25, and WE0.5 samples were 767.5 , 772.0 , and 771.1 \AA^3 , respectively, which differ from each other and are smaller than that previously reported by Skarstad et al.,³⁰ i.e., a cell volume of 775.56 \AA^3 . The cell volume contraction is related to the synthesis method utilized. The CH method reported by Skarstad et al.³⁰ is similar to the method employed here. However, compared to the MAH method, the CH method employs lower heating rates, which influences the speed of crystallization and nucleation. The MAH method uses a high-heating rate, which causes atomic

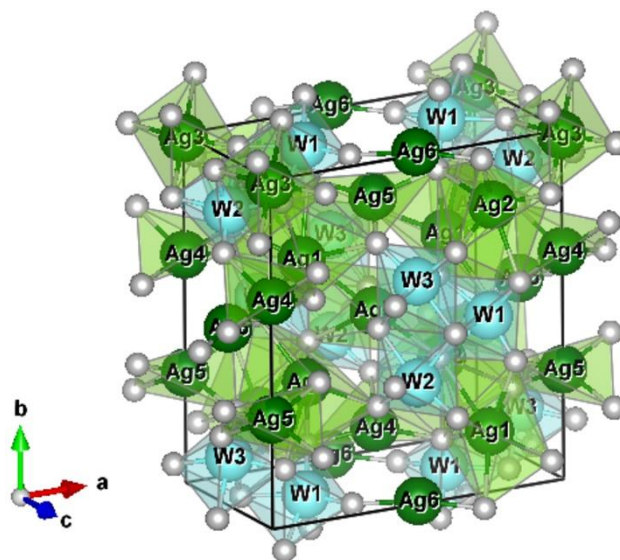
stacking of the crystalline structure, promoting the formation of vacancies, which culminates in shrinkage of the complex unit cell. However, the samples that were obtained with En showed an expansion of the unit cell concerning the pristine sample caused by the complexing agent acting on the synthesis control, which also decreases the nucleation rate. In the WE0.25 and WE0.5 samples, beyond the α -Ag₂WO₄ phase, a secondary phase related to metallic Ag (Ag⁰) was found. Its lattice parameters are similar to values reported in previous studies, i.e., $a = 4.08 \text{ \AA}$ (ICSD card no. 64997).^{31,34} As shown in **Table 2.2**, the quantitative phase analysis of the WE0.25 and WE0.5 samples presented approximately 19% and 31% of metallic Ag. As previously mentioned, the formation of metallic Ag is related to En. Additionally, the WE0.5 sample exhibited a significant increase in the Ag content compared to the WE0.25 sample, suggesting that the concentration of En also influences the amount of metallic Ag in the sample.

Table 2.2 Lattice parameters and unit cell volume obtained by Rietveld refinement for the α -Ag₂WO₄ samples.

		Samples				
		References	W	WE0.25	WE0.5	
α -Ag ₂ WO ₄	LP (Å)	a	10.89(2) ³⁰	10.8707(4)	10.876(2)	10.892(1)
		b	12.03(2) ³⁰	11.9931(5)	12.038(3)	12.018(2)
		c	5.92(2) ³⁰	5.8865(3)	5.902(1)	5.8909(9)
		V (Å ³)	775.56(*) ³⁰	767.45(6)	772.0(3)	771.1(2)
	Content (%)		100	100	81(1)	69.3(9)
Ag ⁰	LP(Å)	a	4.07724(4) ³¹	-	4.086(1)	4.0865(7)
		V (Å ³)	67.78(*) ³¹	-	68.26(7)	68.24(3)
		Content (%)	100	0	18.(1)	30.6(9)

LP: Lattice Parameters. (*) Not indicated in the cif

The unit cell illustrated in **Scheme 2.1** represents the arrangement of [AgO_y] ($y = 2, 4, 6,$ and 7) and [WO₆] constituent clusters of α -Ag₂WO₄. This

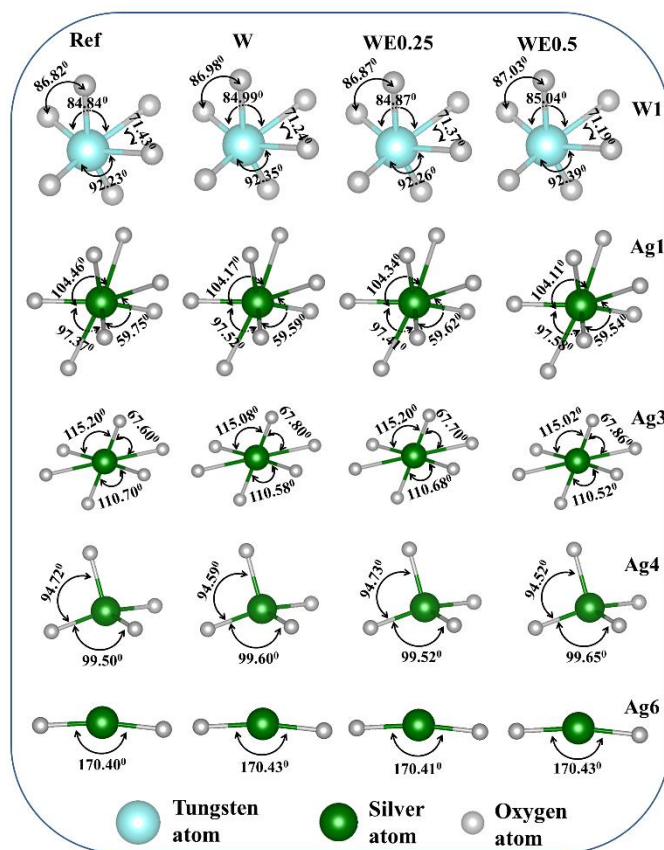


Scheme 2.1 Schematic representation of the crystalline unit cell of α - Ag_2WO_4 (bulk)

unit cell was constructed from the lattice parameters and atomic coordinates obtained by the Rietveld refinement utilizing the Visualization for Electronic and Structural Analysis (VESTA) software.³⁵ The $[\text{AgO}_y]$ ($y = 2, 4, 6,$ and 7) clusters have distorted angles and different coordination numbers, and the W clusters are coordinated by six oxygen atoms and also have distorted angles.

It can be observed from **Scheme 2.2** that the O–Ag–O and O–W–O bond angles of the W and WE0.5 samples present greater deviations compared to the angles in the reference clusters,^{30,33} following the order WE0.25 < W < WE0.5. As can be seen, the addition of En caused structural organization up to the limit, causing more significant structural disorders than those observed for sample W. The increase in the En concentration then caused a local organization in the Ag–O and W–O bonds, and the distortion of these bonds in the WE0.25 and WE0.5 samples, respectively.

These measurements were performed to verify the chemical composition and oxidation states of the constituent elements on the surface of the samples. **Figure 2.2(a)** displays the survey spectra, where it is possible to observe the presence of the elements Ag, W, and O in the samples. The presence of extra elements was not identified, suggesting that the syntheses employed were successful. Note that the presence of C is inherent to the equipment and was observed in all the samples.



Scheme 2.2 Schematic representation of the angular deviation of $[\text{AgO}_y]$ ($y = 2, 4, 6$ e 7) and $[\text{WO}_6]$ clusters.

The high-resolution XPS spectra of the Ag 3d region of the W, WE0.25, and WE0.5 samples were assigned to the doublets, $3d_{3/2}$ and $3d_{5/2}$, due to the spin-orbit coupling, as shown in **Figure 2.2(b)**. These peaks can be deconvoluted into two peaks that correspond to metallic silver and ionic silver. However, as there is an overlap between deconvoluted peaks, it is recommended to measure the Auger parameter, since it confirms the presence of different oxidation states.¹² The Auger parameter was calculated by the sum of the binding energy of Ag 3d and the kinetic energy of Auger MNN (KE) (= BE (Ag $3d_{5/2}$) + KE (Auger (M $_4$ N $_{45}$ N $_{45}$)) (characteristic energy, eV)).³⁶ By amplifying the survey in the Auger Ag M $_4$ N $_{45}$ N $_{45}$ region, the graph shown in **Figure 2.2(c)** was obtained. The Auger parameter values obtained for W, WE0.25, and WE0.50 samples were 724.08, 724.46, and 724.83 eV. Since the Auger parameter for ionic silver is 724.0 eV and for metallic silver is 726.0 eV, such findings indicate the presence of a mixture of silver species exhibiting different oxidation states.³⁷ It was again observed that the concentration of En in the

syntheses favored the formation of metallic Ag on the α -Ag₂WO₄ surface, because the increase in the proportion of the complexing agent modified the proportion of Ag species on the surface of the particles.

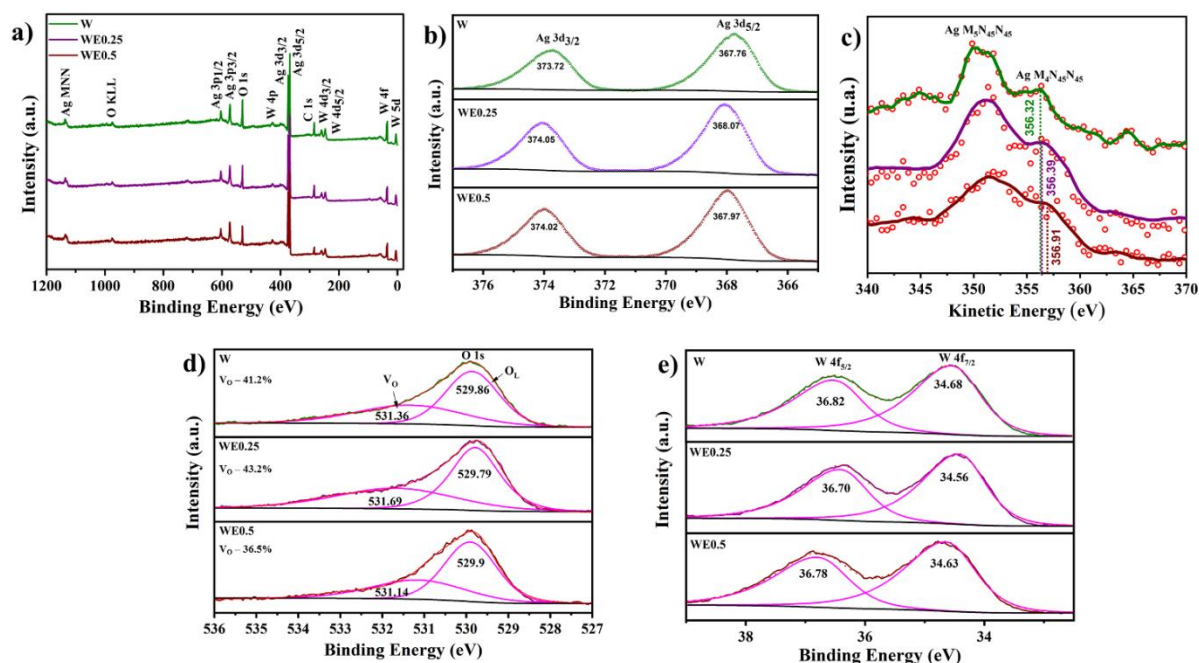


Figure 2.2 XPS spectra for the α -Ag₂WO₄ samples. (a) survey spectra, b), Ag 3d, c) AgM₄N₄₅N₄₅, d) O 1s and e) W 4f core level spectra.

Furthermore, the high-resolution XPS spectra in the O 1s region, shown in **Figure 2.2(d)**, were deconvoluted into two peaks. The peak at approximately 529.9 eV refers to lattice oxygen; the other peak at approximately 531.4 eV is characteristic of oxygen vacancies.^{38,39} It is noted that the sample WE0.5 showed a considerable reduction in oxygen vacancies. This behavior can be linked to the increase in the percentage of metallic Ag found by the XRD refinement analyses. As illustrated in **Figure 2.2(e)**, the high-resolution XPS spectra in the W4f region show two peaks at approximately 34.7 eV and 36.8 eV, which are associated with W4f_{7/2} and W4f_{5/2}, referring to the 6+ oxidation state of W.^{40,41}

This spectroscopy technique was used to obtain information of the local structure around the W atoms in the α -Ag₂WO₄ samples. **Figure 2.3(a)** shows the W L1-edge XANES spectra of α -Ag₂WO₄. **Figure 2.3(b)** displays the W L1-edge XANES spectra of the α -Ag₂WO₄ samples and the following

references, WO_2 , $m\text{-WO}_3$, and Na_2WO_4 . From **Figure 2.3(a)** it can be observed that the spectra present similar characteristics (pre- and post-edge regions), indicating that the samples have a similar local structure. Moreover, the addition of En did not affect the environment around the W atoms. Since the local structures of the $\alpha\text{-Ag}_2\text{WO}_4$ samples are similar, we compared only the spectrum of the WE0.5 sample with reference standards (WO_2 , $m\text{-WO}_3$, and Na_2WO_4), as seen in **Figure 2.3(b)**. From this figure, we observed a difference in the spectra, particularly in the pre-edge region, where P1 is located, which is known to be sensitive to the local symmetry of the absorber atoms.^{42,43} We verified that the WE0.5 spectrum is similar to the spectrum of the $m\text{-WO}_3$ reference, which means that these compounds have similar local symmetry.

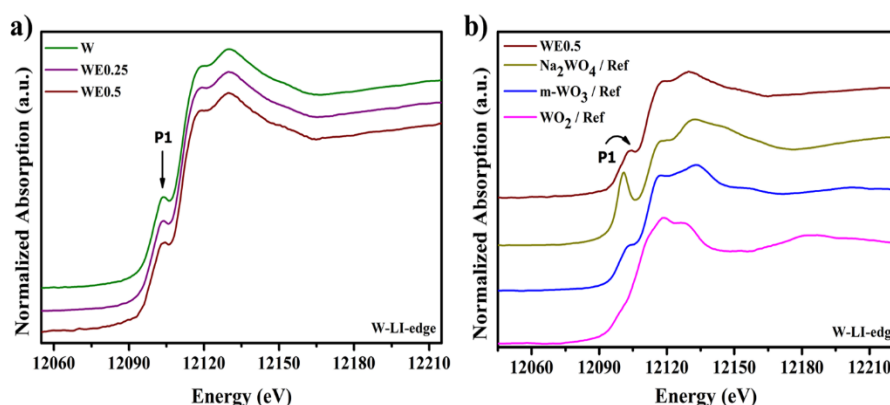


Figure 2.3 a) W-L1 edge XANES spectra of the $\alpha\text{-Ag}_2\text{WO}_4$ samples and b) XANES spectra of the WE0.5 and the reference samples (Na_2WO_4 , $m\text{-WO}_3$ and WO_2).

According to the literature, the physical origin of the P1 peak is an electronic transition from $2s(\text{W}) \rightarrow 5d(\text{W}) + 2p(\text{O})$.^{42,44} The transitions originating at the pre-edge peak are not allowed for regular octahedral symmetries (WO_6), but are allowed for distorted octahedral structures (WO_6).^{44,45} The spectrum of a compound exhibiting units with regular octahedral symmetry will not present a pre-peak, whereas units with distorted octahedral symmetry will have a small pre-edge peak, and units with tetrahedral symmetry will show an intense pre-peak in the XANES spectrum.⁴⁵

Figure 2.3(b) shows that the intensity of the P1 peak is higher for the Na_2WO_4 compound where W atoms exhibit regular tetrahedral coordination,

i.e., WO_4 units. However, a shoulder can be observed for the $m\text{-WO}_3$ reference and WE0.5 sample. Note that the pre-peak P1 is absent in compounds presenting regular WO_6 units; however, distortions in the octahedral symmetry are indicated by a shoulder in the pre-edge region, as presented in **Figure 2.3(b)**. Therefore, the XANES analyses revealed that the $\alpha\text{-Ag}_2\text{WO}_4$ samples are formed by distorted octahedral WO_6 clusters.

Structural order–disorder in a short-range can be analyzed by Raman spectroscopy. The micro-Raman spectra of the asobtained samples are presented in **Figure 2.4**. These spectra show the $\alpha\text{-Ag}_2\text{WO}_4$ vibrational modes in the range of 50 to 1100 cm^{-1} . The bands observed below 500 cm^{-1} are characteristic of the vibrational modes between silver clusters $[\text{AgO}_y]$ ($y = 7, 6, 4,$ and 2) and between Ag^+ and WO_4^{2-} ions in the Ag-O-W bond, known as external vibrational modes. Otherwise, the bands identified above 500 cm^{-1} are associated with internal vibrational modes and are derived from tungsten clusters $[\text{WO}_6]$. Thus, the most intense bands at 96 cm^{-1} and 871 cm^{-1} come from the symmetrical stretching of the $[\text{AgO}_y]$ and $[\text{WO}_6]$ clusters, respectively.^{46,47}

All the spectra presented in **Figure 2.4** show the modes obtained by theoretical calculations with some position deviations, which, according to the literature, are caused by different factors such as synthesis conditions, distortions of O-Ag-O or O-W-O bonds, interaction between ions, and average crystallite size.^{21,48} The W and WE0.25 samples showed similar Raman spectra, indicating that the En concentration used to synthesize the WE0.25 sample did not influence the ordering in a short-range of $\alpha\text{-Ag}_2\text{WO}_4$.

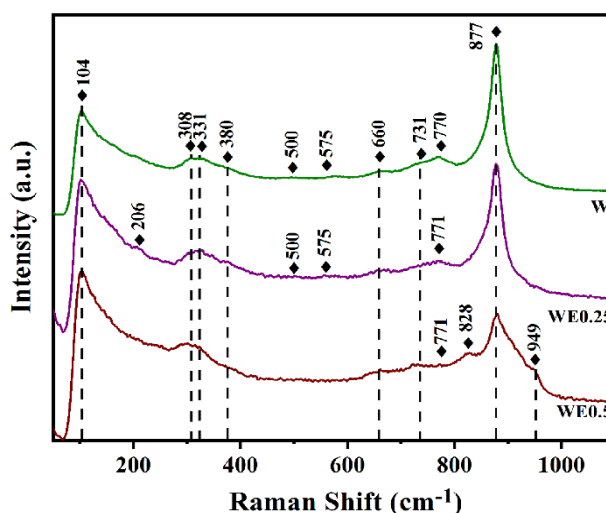


Figure 2.4 Raman spectra of the α - Ag_2WO_4 samples synthesized via the MAH method.

In addition to the expected theoretical modes, the WE0.5 sample presents 2 weak bands centered at 828 and 949 cm^{-1} , which are attributed to the WO_4^{2-} unit due to the stretch and bend deformations.^{33,49} This finding suggests that the use of high En concentrations is able to display vibrational modes that do not appear generally due to low intensity, and it is possible to observe the mode widening at 828 cm^{-1} , which indicates that the α - Ag_2WO_4 structure was disrupted at short distances.^{33,49}

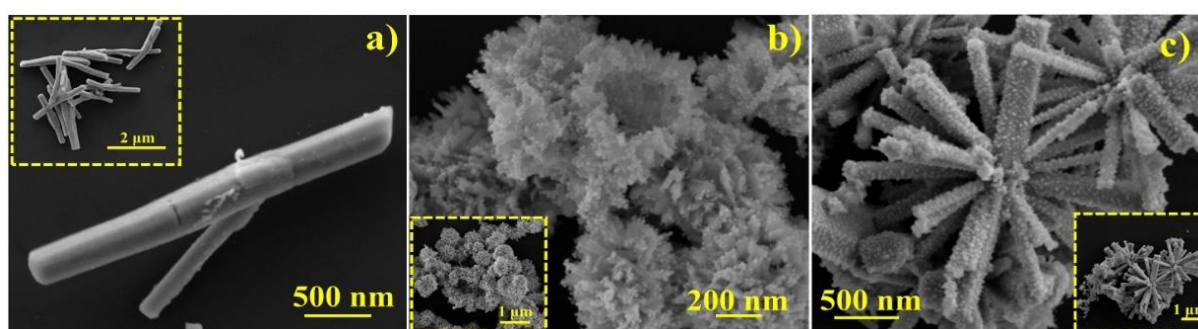


Figure 2.5 FE-SEM Micrographs of the α - Ag_2WO_4 microcrystals synthesized via the MAH method. The inset shows the FE-SEM images at low magnifications. a) W, b) WE0.25 and c) WE0.5

Figure 2.5 shows the FE-SEM images of the as-synthesized α - Ag_2WO_4 samples. It can be observed that the W sample exhibits a morphology similar

to microrods, **Figure 2.5(a)**, which is the most stable morphology for this material synthesized in an aqueous medium, as previously reported.¹⁵ The microrods obtained for the W sample had an average length of $2.12 \pm 0.13 \mu\text{m}$ and an average width of $0.26 \pm 0.01 \mu\text{m}$, as presented in **Figure 2.6(a)**.

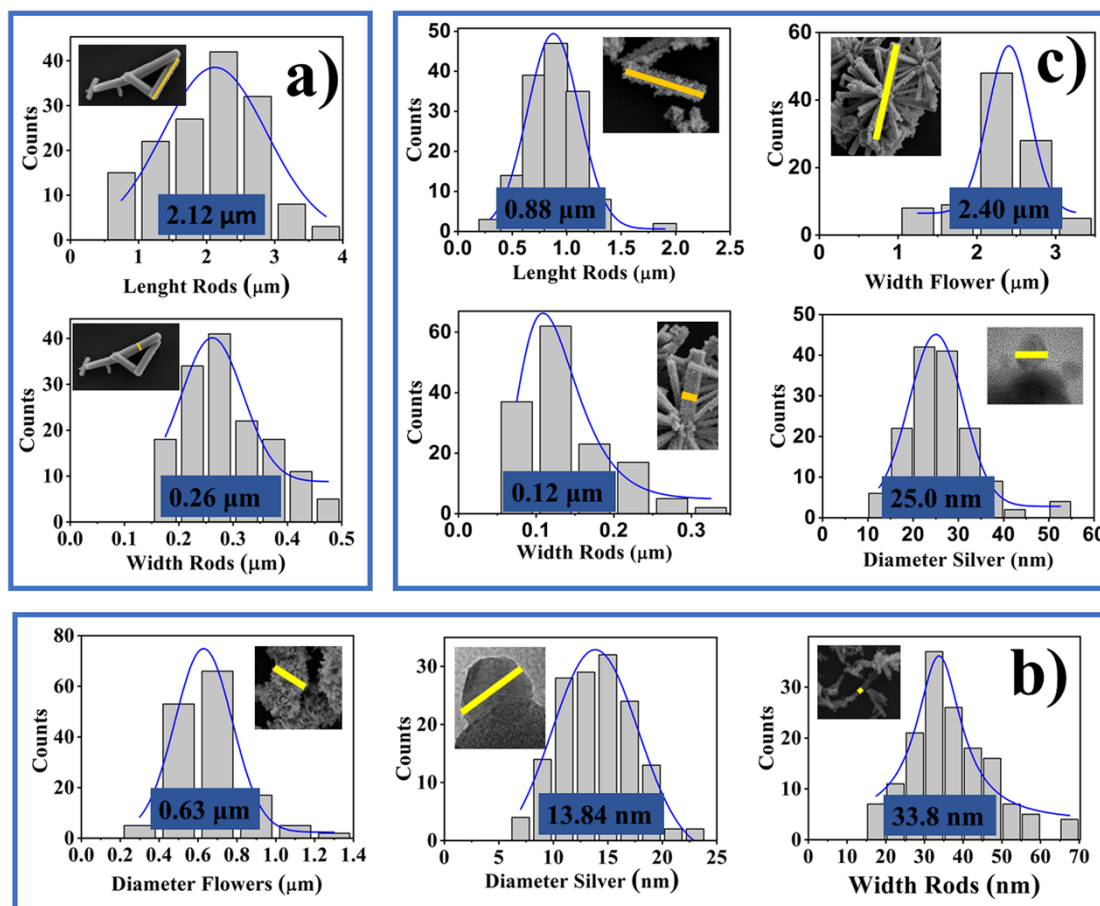


Figure 2.6 Distribution of the $\alpha\text{-Ag}_2\text{WO}_4$ particle sizes: a) W, b) WE0.25 and c) WE0.5.

In **Figure 2.5(b)**, nanorods organized in hollow microflowers and decorated with nanoparticles (NPs) are observed for the WE0.25 sample. The hollow microflowers (WE0.25) have an average width of $0.63 \pm 0.01 \mu\text{m}$, consisting of nanorods and NPs with an average width and diameter of $33.8 \pm 0.6 \text{ nm}$ and $13.8 \pm 0.2 \text{ nm}$, respectively, as presented in **Figure 2.6(b)**. The micrograph of the WE0.5 sample, **Figure 2.5(c)**, shows microrods organized in solid microflower structures also decorated with NPs. The solid microflowers (WE0.5) have a diameter of $2.41 \pm 0.03 \mu\text{m}$ and are composed of microrods with an average length of $0.88 \pm 0.01 \mu\text{m}$ and an average width of 0.12 ± 0.01

μm , decorated with NPs with an average diameter of 25.0 ± 0.2 nm, as observed in **Figure 2.6(c)**. Furthermore, it was verified that the concentration of En governs the achievement of nanorods or microrods, and hollow or solid microflowers.

Figure 2.7 shows the HR-TEM image with the corresponding interplanar distances of the particles that decorated the WE0.25 sample, which is a composite of $\alpha\text{-Ag}_2\text{WO}_4$ and Ag NPs, and presents a very stable behavior under the TEM electron beam. Crystal planes (411), (132), and (211) were identified, whose interplanar distances were 2.49 Å, 2.35 Å, and (3.83 Å and 3.75 Å), respectively (**Figure 2.7(b-e)**). These planes can be assigned to the $\alpha\text{-Ag}_2\text{WO}_4$ orthorhombic structure (ICSD, card no. 4165).^{30,33}

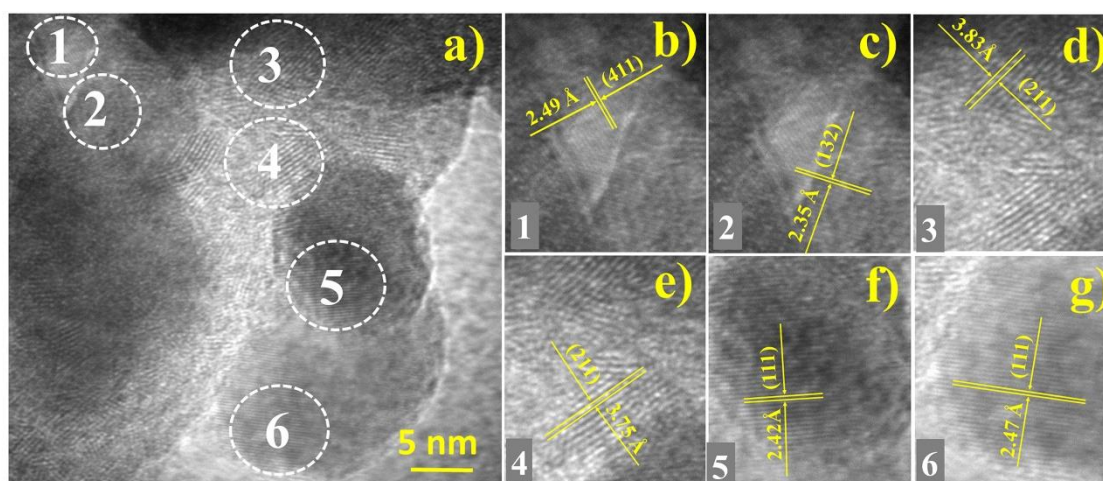
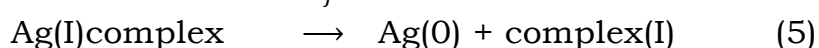
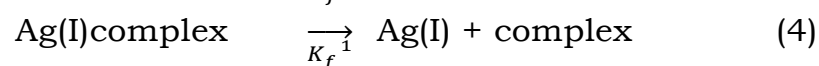
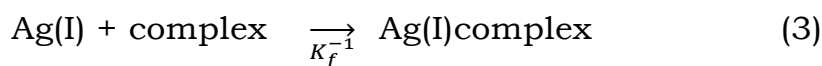


Figure 2.7 HR-TEM image of the a) WE0.25 sample and magnified regions corresponding to $\alpha\text{-Ag}_2\text{WO}_4$ (b–e) and to Ag NPs (f and g).

In addition, the interplanar distances were measured to be 2.42 Å and 2.47 Å (**Figure 2.7(f and g)**), and can be indexed to the (111) family of planes in metallic Ag with a cubic structure (ICSD card no. 64997).^{31,34} Therefore, it is possible to conclude that the NPs that decorate the WE0.25 and WE0.5 samples are Ag metallic NPs.

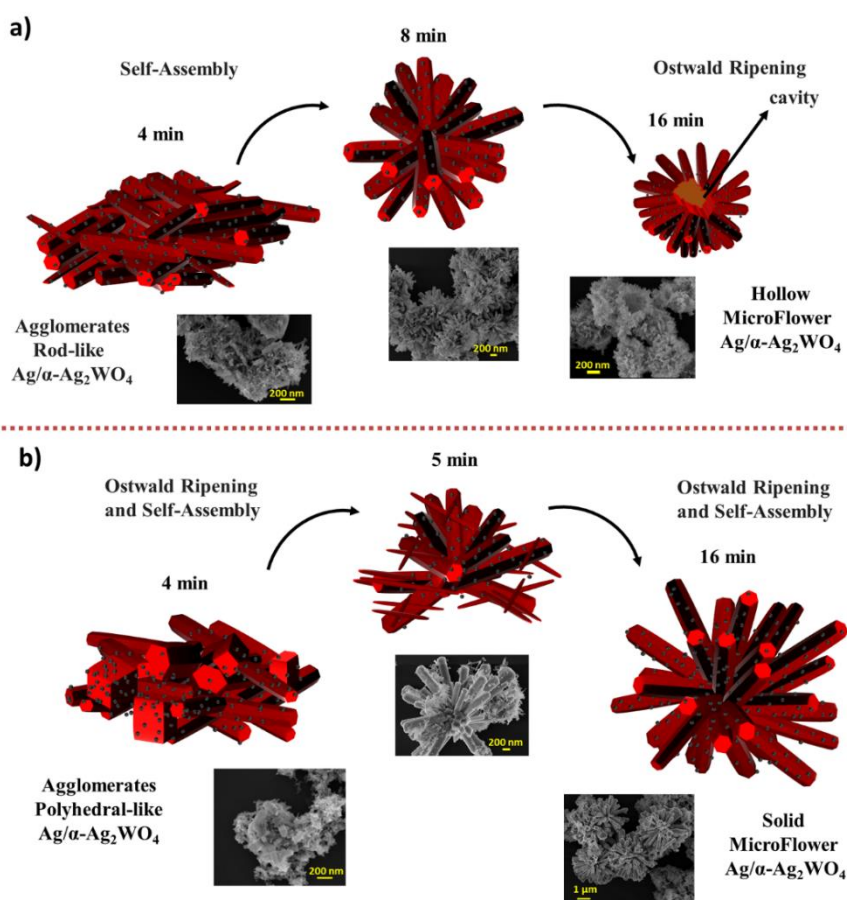
In the absence of En, the Ag^+ and WO_4^{2-} ions precipitate as $\alpha\text{-Ag}_2\text{WO}_4$, leading to preferential surface growth (010) and microrod formation, as presented in **Figure 2.5(a)**. A morphological change was observed by introducing En to the synthesis, due to the formation of the Ag(I) complex (see eqn (3) and (4)). To understand how the hierarchical formation of the

structures occurred, a time-dependent experiment was performed and the intermediate products were analyzed. The FE-SEM images of the intermediates from different reaction times are shown in **Scheme 2.3**. In the first 4 min of MAH synthesis of the WE0.25 sample, rod agglomerates were observed. After 8 min of MAH treatment, they self-organized into hierarchical solid microflowers and, after 16 min of MAH treatment, these structures evolved into hierarchical hollow structures (see **Scheme 2.3(a)**). For the synthesis of the WE0.5 sample, in the first 4 min of the reaction, polyhedron agglomerates are observed, which after 5 min solubilize, recrystallize, and selforganize into an unfinished solid. Then, after 16 min of MAH treatment, well-defined rods and hierarchical solid microflowers are observed, as shown in **Scheme 2.3b**.



When $K_f = 5.01 \times 10^7$ and $K_f^{-1} = 1.99 \times 10^{-8}$

An analogous process was discussed by Ding et al.⁵⁰ in the synthesis of CeVO_4 via the conventional hydrothermal route using L-aspartic acid (L-Asp) as a capping and complexing agent. These researchers concluded that the formation of hollow or solid beads of CeVO_4 depends on the presence and amount of L-Asp used. From their observations, they suggested that the particles grow according to the Ostwald ripening mechanism and that the morphology is defined by the self-assembly process. According to Ding et al., L-Asp influenced the solubility of the particles present inside the newly formed CeVO_4 spheres, which reprecipitated on the outer particles, forming larger particles and hollow microspheres, by the Ostwald ripening process. In addition, L-Asp can be selectively adsorbed to different surfaces, causing different growth rates, which results in cubic structures, and directs the organization of these cubes into spheres, a phenomenon known as self-assembly. This mechanism can be extended to the case of $\alpha\text{-Ag}_2\text{WO}_4$, Where the En acts as L-Asp, resulting in new morphologies through self-assembly and Ostwald ripening.



Scheme 2.3 Schematic illustration of the proposed growth mechanism leading to the formation of α -Ag₂WO₄ samples: a) WE0.25 and b) WE0.5.

Scheme 2.3 illustrates the growth mechanism proposed for the WE0.25 and WE0.5 samples. Based on the above discussion, the formation of the morphology for the WE0.25 sample was proposed to proceed by self-assembly followed by the Ostwald ripening process, as presented in **Scheme 2.3(a)**. The model proposes that addition of En influences the solubility of the small and less crystallized particles present inside the newly formed microflower α -Ag₂WO₄, which reprecipitated on the outer, larger and more crystallized particles, forming larger particles and hollow structures, in addition to guiding the organization of nanorods and forming the hollow microflower, as shown in **Figure 2.5(b)**.⁵¹ However, as depicted in **Scheme 2.3(b)**, by increasing the concentration of En in the reaction medium, a solid, not a hollow structure, was observed. It is suggested that, during the formation of the solid microflower, the redissolution of α -Ag₂WO₄ occurs from the smaller external

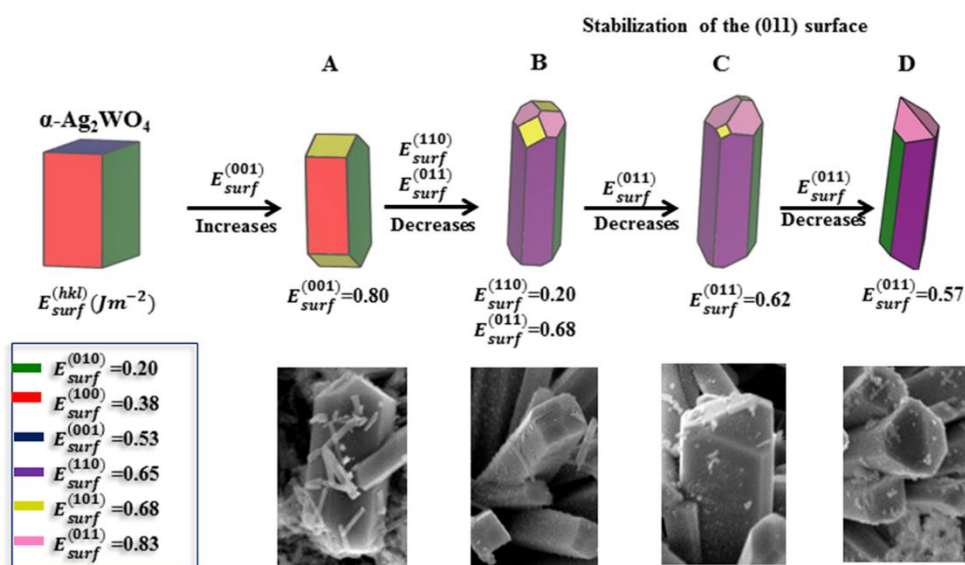
particles, different from the sample WE0.25 in which redissolution occurs from the internal particles, as we observed in **Scheme 2.3(b)**, in the image referring to the 5 min mark, where we see nanorods recrystallizing over the pre-existing microrods. In this way, we obtained particles with diameters and lengths greater than the rods that constitute the WE0.25 sample, as a result of the Ostwald ripening process. We also observed that the particles are recrystallized, organized, and oriented by En, as proposed by Ding et al.,⁵⁰ by the self-assembly mechanism. Therefore, to obtain the WE0.5 sample, it was proposed that the Ostwald ripening and self-assembly mechanisms occur at the same time.

Concomitant to the Ag⁺ ion complexation and particle growth orientation processes, En reduces Ag⁺ ions (eqn (5)) and consequently, decorates the nanorods and microrods of the WE0.25 and WE0.5 samples with Ag NPs, respectively. Wang et al. used En to obtain copper crystals exhibiting different morphologies. To attain this objective, they modified the conditions in the synthesis methodology, in which the reduction of the Cu²⁺ ions occurred due to the decrease in the bond distance between the Cu²⁺ ions and the N in the [Cu(En)₂]²⁺ complex, which enabled the electron transfer from N to Cu²⁺.²³

The equilibrium form of a crystal is defined by the free energies of its faces. Thus, by the Wulff construction principle and the theoretical values of the surface energy E_{surf} ,⁴¹ obtained in a fixed volume, it is possible to predict the different morphologies that a material can possess.¹ Starting from an ideal morphology, and assuming that the crystal morphology is controlled by the lower-energy faces, which are the most stable, a map of the possible morphologies is obtained by adjusting the E_{surf} of the different faces. Subsequently, a comparison between theoretical and experimental morphologies, obtained using FE-SEM images, can be realized.⁴⁸

In the case of α -Ag₂WO₄, consistent with the Wulff construction principle and the surface energy previously reported,²⁴ the experimental FE-SEM images obtained in this work resemble their respective theoretically predicted morphologies, as shown in **Scheme 2.4**. Initially, the ideal morphology is a prism dominated by surfaces (010), (100), and (001). During the synthesis, morphology A (see the inset in **Scheme 2.4**) is obtained by increasing the E_{surf} of face (001) to 0.80 Jm⁻². When the energies of faces (110)

and (011) are decreased to 0.20 and 0.68 Jm^{-2} , respectively, morphology B (see inset in **Scheme 2.4**) is obtained. The C and D (**Scheme 2.4**) morphologies demonstrate the stabilization of face (011) by decreasing E_{surf} from 0.68 to 0.62 and 0.57 Jm^{-2} , which corresponds to the WE0.5 sample. The images illustrate the evolution of the stabilization of faces (110) and (011) over the synthesis time from 0 to 32 min, resulting in the final morphology of the WE0.5 sample, which contains faces (110), (011), and (010).



Scheme 2.4 Crystallographic structure and morphologies of the WE0.5 sample, with crystal planes (101), (100), (001), (110), (010), and (011). Surface energy is in Jm^{-2} . Experimental FE-SEM images of the WE0.5 samples obtained at different times of the MAH method are included for comparison.

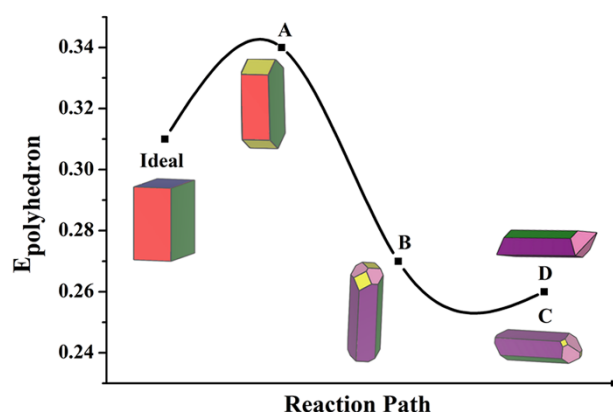
A pathway connecting the ideal morphology with pathways displaying excellent agreement with the experimental morphologies was calculated and is depicted in **Scheme 2.5**. The polyhedron energy (E_{poly}) calculated from eqn (1) for the selected morphology of $\alpha\text{-Ag}_2\text{WO}_4$ is summarized in **Table 2.3**. The energy profile was calculated by decreasing and/or increasing the E_{surf} values of a given surface of the polyhedron. An analysis of the energy profile shows a four step process in which the first step is achieved by increasing the E_{surf} of face (001) and favors the appearance of face (101), obtaining the intermediate A shape. A subsequent decrease in the E_{surf} value for (110) and (011), which

induces the formation of the B shape, predominantly exposes the (010) and (110) surface planes as well as the (011) surface plane. Finally, the decrease in E_{surf} for (011) leads to the end C and D shapes (**Scheme 2.5**).

Table 2.3 Surface energy values (E_{surf} , Jm^{-2}), the contribution of the surface area by the total area (C_i , %), and the polyhedron energy (E_{poly} , Jm^{-2}) of each intermediate morphology to obtain the WE0.5 sample ($\alpha\text{-Ag}_2\text{WO}_4$)

Surface	E_{surf} (C_i , %)				
	$\alpha\text{-Ag}_2\text{WO}_4$ (Ideal)	A	B	C	D
(010)	0.20(52.5)	0.20(56.0)	0.20(21.0)	0.20(20.3)	0.20(19.4)
(100)	0.38(27.6)	0.38(25.0)	0.38(0.00)	0.38(0.00)	0.38(0.00)
(001)	0.53(19.9)	0.80(0.00)	0.80(0.00)	0.80(0.00)	0.80(0.00)
(110)	0.65(0.00)	0.65(0.00)	0.20(64.5)	0.20(65.7)	0.20(64.3)
(101)	0.68(0.00)	0.68(19.0)	0.68(6.49)	0.68(0.15)	0.68(0.00)
(011)	0.83(0.00)	0.83(0.00)	0.68(8.00)	0.62(13.8)	0.57(16.3)
$E_{\text{polyhedron}}$	0.31	0.34	0.27	0.26	0.26

It is important to note that both theoretical morphologies labelled C and D herein correspond to a minimum in the reaction coordinate diagram depicted in **Scheme 2.5**, indicating that the reaction path is thermodynamically favorable. This procedure can be considered an effective tool to investigate the morphology transformation and crystal growth mechanisms from a thermodynamic and kinetic point of view.²⁴



Scheme 2.5 Schematic representation of the energy profile to obtain the WE0.5 morphology. The intermediate morphologies are indicated as A - D, obtained by variations the $E_{\text{surf.}}$ values.

These measurements were performed in order to investigate the influence of structural ordering and defects on the electronic energy level behavior. **Figure 2.8** shows the PL spectra of samples W, WE0.25, and WE0.5 at room temperature. The PL emission spectra of Ag_2WO_4 are generally deconvolved into two components, positioned in the blue and green-light regions.¹⁵ The PL spectra of the W and WE0.25 samples present a broadband profile in the visible spectral region with maximum emissions at 472 nm and 462 nm, respectively. The WE0.5 sample shows emission in the visible region between 400 nm and 650 nm with a maximum emission at 449 nm. The observed blue effect suggests that E_n causes distortions in the $[\text{WO}_6]$ clusters, as already discussed in **Scheme 2.2**, so the greater blue shift in the WE0.5 sample may be associated with the use of a higher concentration of the complexant.²¹ These broadband profiles suggest that the emission involves electronic transitions from additional energy states within the band gap, also known as multiphononic and multilevel processes, whose origins are due to the distortions and defects of the $[\text{AgO}_y]$ ($y = 2, 4, 6,$ and 7) and $[\text{WO}_6]$ clusters.³ These distortions and defects generate a high density of intermediate energy states between valence and conduction bands with a slight energy variation from each other. The excited electrons transit through these energy levels for relaxation of the electron momentum through several pathways, thus emitting phonons to the lattice for later emission of photons in a wide energy range.

The PL spectra of the W and WE0.25 samples (**Figure 2.8(a-b)**) were deconvoluted using three Gaussian functions at emission peaks centered at 448 nm (2.76 eV), 514 nm (2.41 eV), and 644 nm (1.93 eV). The spectrum of the WE0.5 sample (**Figure 2.8(c)**) was deconvoluted with four emission peaks centered at 425 nm (2.92 eV), 449 nm (2.76 eV), 475 nm (2.61 eV), and 534 nm (2.32 eV). The pie charts (see insets in **Figure 2.8(a-c)**) show the contribution percentage of each spectral region color. Emissions in the blue and green regions are due to the presence of distorted clusters, which produce more energetic emissions, 3.26–2.19 eV. Emissions in the red region are due to silver output and oxygen vacancies in the $[\text{AgO}_y]$ and $[\text{WO}_6]$ clusters, which in turn produce less energetic emissions, 2.19–1.59 eV.²¹ Emissions in higher energetic regions are caused by structural defects in the crystalline lattice or shallow defects, because they give rise to energy levels close to the valence band (VB) and conduction band (CB). Emissions on the low energy side are known as deep defects, because they cause energy levels closer to the center of the band gap.⁵²

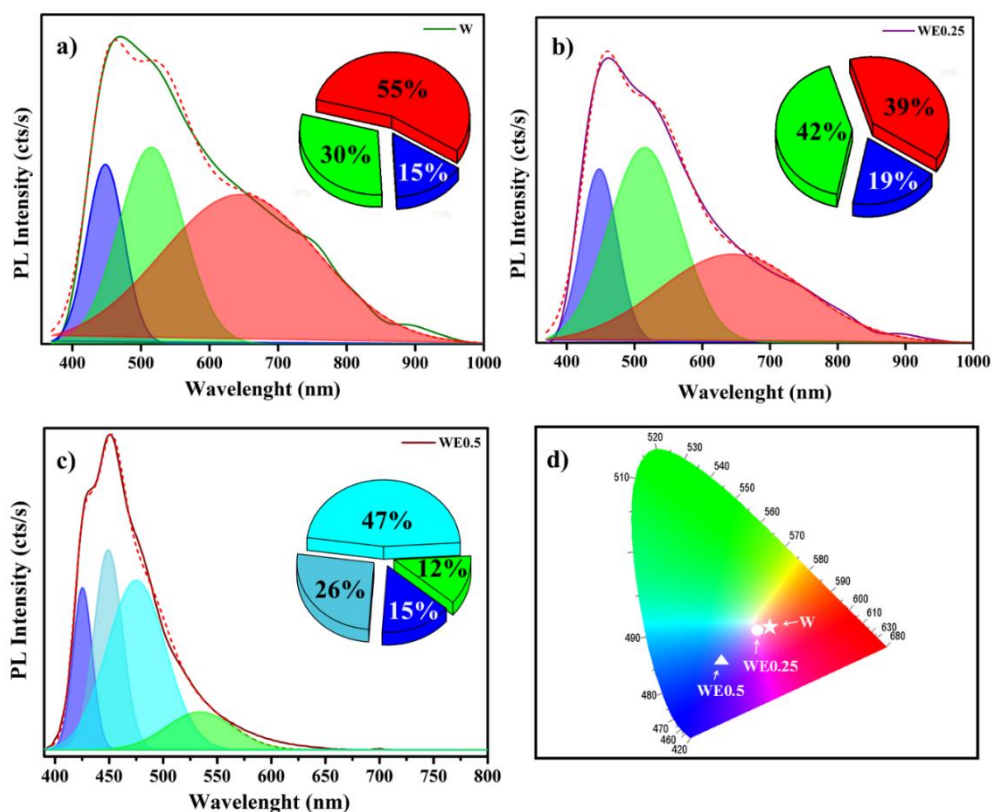


Figure 2.8. Deconvolution of PL spectra. (Insets) The percentage of the color area corresponds to the emission peak of microcrystals a) W, b) WE0.25, c) WE0.5 and d) the CIE chromaticity diagram of α -Ag₂WO₄ samples.

It was observed that the higher concentration of En complexing agent added to the synthesis results in a larger amount of structural defects being introduced. As can be seen in the pie charts included in **Figure 2.8(a-c)**, the contribution of the oxygen vacancy defects goes from 55% to 39% to 0% for samples W, WE0.25, and WE0.5, respectively, whereas structural defects present in the material increased from 45% to 61% to 100% for W, WE0.25, and WE0.5 samples, respectively. These results corroborate the results of XPS, through which there is a decrease in oxygen vacancies in the sense of increasing the concentration of En employed. A possible explanation for the increase in structural defects is the reduction reaction of the Ag⁺ ion caused by En. It was observed that the En complexing agent favoured the formation of metallic Ag, and may have contributed to the increase in the distortions of the lattice forming distorted [WO₆] clusters of the WE0.5 sample, resulting in more disorder in the medium range. Therefore, the PL spectra confirm the

oxygen vacancy disorders and structural defects for samples W and WE0.25, and structural defects for the WE0.5 sample due to the higher concentration of En.

The global PL emission of the samples is presented in the Diagram of the Commission International de L'Eclairage (CIE), chromaticity included, as shown in **Figure 2.8(d)**. The W sample presents emissions in the purplish pink color region with chromaticity coordinates $x = 0.40$ and $y = 0.32$, according to the literature.⁵² The samples obtained with the En complexing agent showed a remarkable displacement in the emission color. For example: the WE0.25 sample with chromaticity coordinates $x = 0.37$ and $y = 0.32$ presents an emission near the white region, with approximately 40% structural defects and 60% vacancy defects. The WE0.5 sample, which presented a 100% structural defect contribution, showed chromaticity coordinates at $x = 0.25$ and $y = 0.23$, with an emission in the blue region. Thus, the concentration of En significantly modified the overall PL emission of the samples. The NPs that were deposited on the surface constitute plasmon NPs. These surface plasmons involve electron motion in the metal, which allows light to be concentrated in nanometer-scale volumes or hot spots. This physics effect can lead to enhanced light-matter interactions at the PL. Knowing that ethylenediamine disorganizes tungstate clusters, it is possible to model the synthesis methodology to obtain other tungstates that emit in specific regions, such as, for example, white, controlling the disorder of the forming clusters, the network modifiers and the emission intensity, with the purpose of using these materials in LEDs.

The photocatalytic activity of the as-obtained samples was also analyzed, noting that the WE0.25 and WE0.5 samples showed low potential for photodegradation compared to sample W, as presented in **Figure 2.9(a and b)**. This behavior can be caused by two effects: 1) excess metallic Ag on the surface, and 2) reduction of oxygen vacancies in the material structure.

The amount of Ag metallic particles on the surface of α -Ag₂WO₄ followed the inverse order of photocatalytic activity $W < WE0.25 < WE0.5$. These results corroborate the investigation reported by Liu et al.²² who synthesized Ag/ α -Ag₂WO₄ utilizing the CH method, followed by the chemical reduction process. These researchers observed that the samples which presented excess Ag

metallic particles on the surface exhibited low photoactivity compared to the samples with a suitable amount of silver. The authors linked this phenomenon with the fact that the excess silver covers the surface available for the photochemical reaction and hinders the transfer of electrons to the outside, reducing the photocatalytic activity.

It is interesting to note that, although the samples obtained by Liu et al. are decorated with silver, their proportion is not detected by XRD. The samples obtained by this work, on the other hand, present two well-defined phases of α -Ag₂WO₄ and metallic Ag identified by XRD. Therefore, the proportion, as already estimated in the refinement calculations, is much higher than that obtained by Liu et al. As already mentioned, the excess of superficial silver hindered the performance of the samples.

In our work, the density of oxygen vacancies followed the direct order of the photocatalytic activity WE0.5 < WE0.25 < W. Different literature reports describe the photochemical reaction mechanism presented in this work, as shown in eqn (6)–(10).^{24,53} In this mechanism, the radical cluster [AOz]' interacts with water, producing, among other things, the hydroxyl radical, OH*, which is extremely oxidizing (eqn (8)). Meanwhile, electrons [AOz]' react with O₂ producing O₂' which, when interacting with the H' species, produces the peroxide radical HO*₂ (see eqn (7) and (9)). As previously discussed, the PL graphs in **Figure 2.8** showed that the complexing agent hindered the participation of oxygen vacancies in electronic transitions; therefore, the production of hydroxyl radicals is reduced in the WE0.25 sample and virtually eliminated in the WE0.5 sample. However, the reaction of electrons with O₂

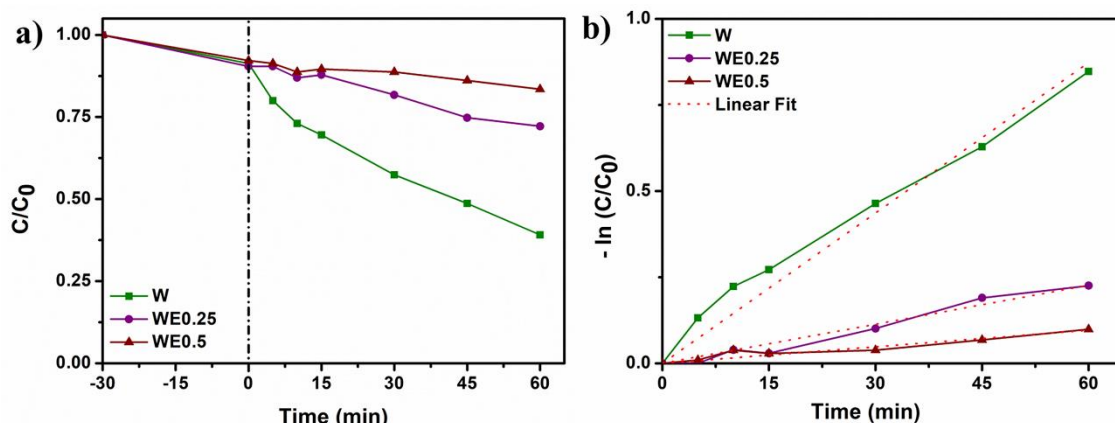
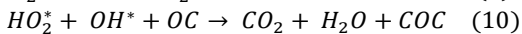
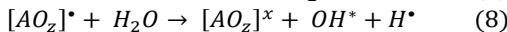
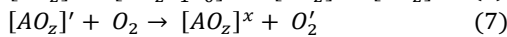
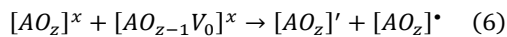


Figure 2.9 a) Photocatalytic activities of samples in degradation of RhB under ultra-violet light irradiation, and b) corresponding plot of $-\ln(C/C_0)$ versus time.

still occurs, leading to the minor photocatalytic activity of the material, and the low effectiveness due to metallic Ag, which prevents the transfer of electrons to the outside, making them unavailable for the photocatalytic reaction.



When A = W, z = 6 or A = Ag, z = 2, 4, 6 or 7

OC = organic compounds and COC = colorless organic compounds.

It is also possible to adjust the proportion of ethylenediamine used in the synthesis, to obtain Ag/Ag₂WO₄ with better photocatalytic performance.

2.4 - Conclusions

In conclusion, Ag/ α -Ag₂WO₄ was successfully obtained via the MAH method. For the first time, the ethylenediamine (En) complexing agent was used to control the morphological characteristics, structural order/disorder, optical properties, and photocatalytic performance of α -Ag₂WO₄ crystals. En also reduced Ag⁺ in the synthesis process proposed in this work, playing a fundamental role in the decoration of Ag NPs. Also observed was a favorable emission near the white light (WE0.25) and blue light (WE0.5) regions. The photocatalytic tests confirmed that the excess surface metallic silver and the removal of oxygen vacancies were essential for a good photocatalytic performance of α -Ag₂WO₄. Our investigation showed that En can modulate the structural, morphological, and optical properties of α -Ag₂WO₄, and also decorate it with Ag NPs. This semiconductor framework represents a promising alternative to metals, as its plasmon frequency can be controlled in the crystal formation step by blocking certain positions of the primary clusters. Therefore, it represents a type of tunable, high-quality material for plasmonic applications. Finally, the growth mechanism of the particles, which results in interesting multidimensional structures, together with the decoration of Ag NPs, indicates the possibility of obtaining structures with

modeled optical and photocatalytic properties, by controlling the concentration of the complexing agent.

2.5 - References

- 1 J. Andrés, L. Gracia, A. F. Gouveia, M. M. Ferrer and E. Longo, *Nanotechnology*, 2015, 26, 405703.
- 2 Y. Bi, H. Hu, S. Ouyang, G. Lu, J. Cao and J. Ye, *Chem. Commun.*, 2012, 48, 3748–3750.
- 3 M. D. P. Silva, R. F. Gonçalves, I. C. Nogueira, V. M. Longo, L. Mondoni, M. G. Moron, Y. V. Santana and E. Longo, *Spectrochim. Acta, Part A*, 2016, 153, 428–435.
- 4 J. L. Cerrillo, A. E. Palomares and F. Rey, *Microporous Mesoporous Mater.*, 2020, 305, 110367.
- 5 M. Asghar, S. Habib, W. Zaman, S. Hussain, H. Ali and S. Saqib, *Microsc. Res. Tech.*, 2020, 1–12.
- 6 X. Xin, Y. Gao, Q. Zhang, Z. Wang, D. Sun, S. Yuan and H. Xia, *Soft Matter*, 2018, 14, 8352–8360.
- 7 A. Koyappayil, S. Berchmans and M. H. Lee, *Colloids Surf., B*, 2020, 189, 110840.
- 8 D. Liu, W. Huang, L. Li, L. Liu, X. Sun, B. Liu, B. Yang and C. Guo, *Nanotechnology*, 2012, 28, 1–10.
- 9 K. Dai, J. Lv, L. Lu, C. Liang, L. Geng and G. Zhu, *Mater. Chem. Phys.*, 2016, 177, 529–537.
- 10 S. Li, W. Jiang, S. Hu, Y. Liu and J. Liu, *Mater. Lett.*, 2018, 224, 29–32.
- 11 D. Xu, B. Cheng, J. Zhang, W. Wang, J. Yu and W. Ho, *J. Mater. Chem. A*, 2015, 3, 20153–20166.
- 12 D. Barreca, A. Gasparotto, C. Maragno, E. Tondello and S. Gialanella, *J. Appl. Phys.*, 2005, 97, 054311.
- 13 D. Barreca, A. Gasparotto, C. Maragno, E. Tondello and S. Gialanella, *J. Nanosci. Nanotechnol.*, 2007, 7, 2480–2486.
- 14 L. F. Da Silva, A. C. Catto, W. Avansi, L. S. Cavalcante, J. Andrés, K. Aguir, V. R. Mastelaro and E. Longo, *Nanoscale*, 2014, 6, 4058–4062.
- 15 L. S. Cavalcante, M. A. P. Almeida, W. Avansi, R. L. Tranquilin, E. Longo, N. C. Batista, V. R. Mastelaro and M. S. Li, *Inorg. Chem.*, 2012, 51, 10675–10687.
- 16 A. Sreedevi, K. P. Priyanka, S. C. Vattappalam and T. Varghese, *J. Electron. Mater.*, 2018, 47, 6328–6333.
- 17 A. Sreedevi, K. P. Priyanka, K. K. Babitha, N. Aloysius Sabu, T. S. Anu and T. Varghese, *Indian J. Phys.*, 2015, 89, 889–897.
- 18 C. H. B. Ng and W. Y. Fan, *CrystEngComm*, 2016, 18, 8010–8019.

- 19 F. X. Nobre, I. S. Bastos, R. O. dos Santos Fontenelle, E. A. A. Júnior, M. L. Takeno, L. Manzato, J. M. E. de Matos, P. P. Orlandi, J. de Fátima Souza Mendes, W. R. Brito and P. R. da Costa Couceiro, *Ultrason. Sonochem.*, 2019, 58, 104620.
- 20 Y. Lu, Y. J. Deng, X. Y. Zhang and J. K. Liu, *Mater. Technol.*, 2017, 32, 178–185.
- 21 E. Longo, D. P. Volanti, V. M. Longo, L. Gracia, I. C. Nogueira, M. A. P. Almeida, A. N. Pinheiro, M. M. Ferrer, L. S. Cavalcante and J. Andrés, *J. Phys. Chem. C*, 2014, 118, 1229–1239.
- 22 D. Liu, W. Huang, L. Li, L. Liu, X. Sun, B. Liu, B. Yang and C. Guo, *Nanotechnology*, 2017, 28, 1–10.
- 23 X. Wang, K. Han, F. Wan, Y. Gao and K. Jiang, *Mater. Lett.*, 2008, 62, 3509–3511.
- 24 N. G. Macedo, A. F. Gouveia, R. A. Roca, M. Assis, L. Gracia, J. Andrés, E. R. Leite and E. Longo, *J. Phys. Chem. C*, 2018, 122, 8667–8679.
- 25 H. M. Rietveld, *J. Appl. Crystallogr.*, 1969, 2, 65–71.
- 26 L. W. Finger, D. E. Cox and A. P. Jephcoat, *J. Appl. Crystallogr.*, 1994, 27, 892–900.
- 27 P. W. Stephens, *J. Appl. Crystallogr.*, 1999, 32, 281–289.
- 28 R. J. Hill and C. J. Howard, *J. Appl. Crystallogr.*, 1987, 20, 467–474.
- 29 H. M. Rietveld, *Acta Crystallogr.*, 1967, 22, 151–152.
- 30 P. M. Skarstad and S. Geller, *Mater. Res. Bull.*, 1975, 10, 791–799.
- 31 R. Becherer and G. Ifland, *Naturwissenschaften*, 1954, 4, 471.
- 32 M. Alain, M. Jacques, M. B. Diane and P. Karine, *J. Phys.: Conf. Ser.*, 2009, 190, 012034.
- 33 D. Stone, J. Liu, D. P. Singh, C. Muratore, A. A. Voevodin, S. Mishra, C. Rebholz, Q. Ge and S. M. Aouadi, *Scr. Mater.*, 2010, 62, 735–738.
- 34 P. Demokritou, R. Bchel, R. M. Molina, G. M. Deloid, J. D. Brain and S. E. Pratsinis, *Inhalation Toxicol.*, 2010, 22, 107–116.
- 35 K. Momma and F. Izumi, *J. Appl. Crystallogr.*, 2008, 41, 653–658.
- 36 C. Hu, Y. Lan, J. Qu, X. Hu and A. Wang, *J. Phys. Chem. B*, 2006, 110, 4066–4072.
- 37 D. Chen, Y. Zhang, T. Bessho, J. Sang, H. Hirahara, K. Mori and Z. Kang, *Chem. Eng. J.*, 2016, 303, 100–108.
- 38 J. Lv, K. Dai, J. Zhang, L. Lu, C. Liang, L. Geng, Z. Wang, G. Yuan and G. Zhu, *Appl. Surf. Sci.*, 2017, 391, 507–515.
- 39 M. Pirhashemi and A. Habibi-Yangjeh, *J. Colloid Interface Sci.*, 2017, 491, 216–229.
- 40 M. Blais-Roberge, M. Rioux, Y. Ledemi and Y. Messaddeq, *J. Non-Cryst. Solids*, 2017, 470, 61–69.

- 41 F. Y. Xie, L. Gong, X. Liu, Y. T. Tao, W. H. Zhang, S. H. Chen, H. Meng and J. Chen, *J. Electron Spectrosc. Relat. Phenom.*, 2012, 185, 112–118.
- 42 G. Poirier, F. C. Cassanjes, Y. Messaddeq, S. J. L. Ribeiro, A. Michalowicz and M. Poulain, *J. Non-Cryst. Solids*, 2005, 351, 3644–3648.
- 43 R. V. Vedrinskii, V. L. Kraizman, A. A. Novakovich, P. V. Demekhin and S. V. Urazhdin, *J. Phys.: Condens. Matter*, 1998, 10, 9561–9580.
- 44 A. Kuzmin and J. Purans, *Radiat. Meas.*, 2001, 33, 583–586.
- 45 S. Yamazoe, Y. Hitomi, T. Shishido and T. Tanaka, *J. Phys. Chem. C*, 2008, 112, 6869–6879.
- 46 S. K. Gupta, K. Sudarshan, P. S. Ghosh, S. Mukherjee and R. M. Kadam, *J. Phys. Chem. C*, 2016, 120, 7265–7276.
- 47 A. Turkovic, L. Fox, J. F. Scott, S. Geller and G. F. Ruse, *Mater. Res. Bull.*, 1977, 12, 189–196.
- 48 V. M. Longo, C. C. De Foggi, M. M. Ferrer, A. F. Gouveia, R. S. André, W. Avansi, C. E. Vergani, A. L. Machado, J. Andrés, L. S. Cavalcante, A. C. Hernandez and E. Longo, *J. Phys. Chem. A*, 2014, 118, 5769–5778.
- 49 H. Feilchenfeld and O. Siiman, *J. Phys. Chem.*, 1986, 90, 4590–4599.
- 50 J. Ding, X. Liu, M. Wang, Q. Liu, T. Sun, G. Jiang and Y. Tang, *CrystEngComm*, 2018, 20, 4499–4505.
- 51 Z. Wang and R. Yu, *Adv. Mater.*, 2019, 31, 1–34.
- 52 M. Mondego, R. C. de Oliveira, M. Penha, M. S. Li and E. Longo, *Ceram. Int.*, 2017, 43, 5759–5766.
- 53 L. S. Cavalcante, J. C. Sczancoski, N. C. Batista, E. Longo, J. A. Varela and M. O. Orlandi, *Adv. Powder Technol.*, 2013, 24, 344–353

Capítulo 3

α -Ag₂WO₄ under microwave, electron beam and femtosecond laser irradiations: Unveiling the relationship between morphology and photoluminescence emissions

Mayara Mondego Teixeira,^{‡a*} LÍlian Cruz Santos,^{‡a} Ana Cristina Mora Tello,^{‡a*} Priscila Barros Almeida,^{‡a} Jussara Soares da Silva,^{‡a} Letícia Laier,^{‡b} Lourdes Gracia,^{c,d} Marcio Daldin Teodoro,^e Luís Fernando da Silva,^e Juan Andrés,^c and Elson Longo,^{a*}

^aDepartamento de Química, CDMF, Universidade Federal de São Carlos, 13565-905 São Carlos, São Paulo, Brazil.

^bLaboratório Interdisciplinar em Cerâmica, Departamento de Físico-Química, Instituto de Química, UNESP, 14800-900, Araraquara, São Paulo, Brazil.

^cDepartamento de Química Física i Analítica, University Jaume I, 12071, Castelló de la Plana, Spain.

^dDepartamento de Química Física, Universitat de València, 46100, Burjassot, Spain.

^eDepartamento de Física, Universidade Federal de São Carlos, 13565-905, São Carlos, São Paulo, Brazil.

ABSTRACT. In this study, the α -Ag₂WO₄ samples were successfully synthesized combined two methods, co-precipitation and microwave-assisted hydrothermal. Later, two different irradiation processes: electron beam and femtosecond laser are applied. Unit cell changes were shown by X-ray measurements and Rietveld analysis and compared with the results obtained for first-principles calculations. The formation of oxygen vacancies on the surface of the particles after the irradiation process was revealed by XPS measurements. Electron beam and femtosecond laser irradiations were found

to cause expansion of the unit cell, form oxygen vacancies on the surface, change the angle and distance between O–Ag and O–W bonds, and modify the particle morphology to rod-, cube- and sphere-like. The XANES measurements confirm that the local order of the W atoms is maintained along the different irradiation processes. Based on the theoretical analysis of surfaces investigation and Wulff construction, the contribution of (010) and (101) surfaces at the emission centers in 550 and 733 nm associated with the PL spectrum of α -Ag₂WO₄, was established.

KEYWORDS: α -Ag₂WO₄; electron beam irradiation; femtosecond laser irradiation; photoluminescence; morphology; surface band gap.

3.1 - Introduction

Recently, alpha-silver tungstate (α -Ag₂WO₄) has attracted increasing attention from scientists due to its several unique characteristics. Among them, we can cite its nontoxicity [1–3], photoluminescence properties [4,5], and photocatalytic applications [1–6]. These properties can be improved according to the obtained morphologies by different synthesis methodologies, such as simple co-precipitation [6–8], conventional hydrothermal [9,10], or microwave-assisted hydrothermal (MAH) method [11].

When it comes to time-saving synthesis, the MAH method is considerably more advantageous than other methodologies [12–15] since the use of microwave irradiation triggers different processes between the forming clusters and the electromagnetic waves, culminating in the formation of more oxygen defects and more structural/electronic disorder effects in the structure of the material [16].

The properties derived from the interaction between electromagnetic waves and the material have been studied for several decades. It is known that the characterization of structure or property responses of the material to these stimuli from the surrounding environment plays a key role in the understanding and rationalization of the structure-property relationship function in modern science and engineering [17,18]. In a recent study conducted by our group, α -Ag₂WO₄ was obtained by the MAH method. It was

observed that the photoluminescence of these samples migrated from red to blue, according to the morphology and structural disorder presented [19].

It is also known that factors such as temperature, time of synthesis, and presence of surfactants among others can alter the lattice structural properties of α -Ag₂WO₄ as well [6,20,21]. Regarding the influence of time of exposure to MAH, in a recent study performed by Laier et al. (2020) [20] both experimental and computational results revealed that at certain times of operation of the MAH system it was possible to obtain samples with the highest active surface composition since they showed a higher density of broken bonds and greater surface energy. The irradiation of electron beam and femtosecond laser on the α -Ag₂WO₄ structure has attracted attention [10,11,22–32], where the main focus is to elucidate the mechanism of growth of Ag nanoparticles on the surface α -Ag₂WO₄ and the effects on the photoluminescence emissions [22, 32-35].

In this work, we have tried to understand the phenomena provoked by the interaction between α -Ag₂WO₄ and electron beam and femtosecond laser irradiation, which were found to be able to promote changes in the lattice parameters, structure, and morphology of the crystal. All of these changes alter the material properties, for example, its electronic and magnetic properties, [22,34,35], photoluminescence emissions, and consequently its physical, chemical, and/or biological applications [6,20,31,36,37]. Therefore, it is possible to adjust the morphology, lattice, and electronic structures of α -Ag₂WO₄ materials resulting from these modifications [19,38].

It should be noted that alterations in the lattice structure of the crystal may directly contribute to the variation in the number of vacancies. Once there is a critical correlation among lattice parameters, structural stability, electronic structure, band gap, and photoluminescence properties, it is important to have a broad understanding at the atomic-level of its bulk and surface.

In summary, this article came to increase knowledge about this structure and bring newness through the approach of explaining photoluminescence (PL), showing the surface that contributes to the property. It is well known that PL emission is the concentration of different defects: intrinsic (bulk and surface), extrinsic under interface, and structural order-

disorder [32,39]. However, the surface contribution is still little known for the α -Ag₂WO₄ structure. For this purpose, we synthesized α -Ag₂WO₄ using the coprecipitation (CP) method, followed by the MAH method as a function of the synthesis time (2, 4, 8, 16, and 32 min) and electron beam and femtosecond laser irradiations. The crystals were characterized by different structural techniques, and their optical and PL properties were investigated. Theoretical calculations at the density functional theory (DFT) level were performed to obtain atomic information of the electronic structure of the material after irradiation. In addition, to understand the relationship between PL emissions of the α -Ag₂WO₄ exposed surfaces, the corresponding band gap was analyzed. The paper is organized as follows: section 3.2 describes the experimental procedure (synthesis, characterization, and irradiation methods) and the theoretical method, whereas section 3.3 shows the results and discussion on the structure, morphology, and optical properties of α -Ag₂WO₄. Finally, we present our main conclusions in section 3.4.

3.2 - Experimental Section

Synthesis of α -Ag₂WO₄ crystals: The α -Ag₂WO₄ samples were synthesized by the CP method, similar to the description made by Foggi, *et al.* (2017) [40], being considered a volume of 30 mL of ethanol, then kept under continuous stirring for 10 min; the as-obtained sample was denoted as CP. The suspension followed by treatment in the MAH method (**Figure 3.1 a,b**) under the previous studies by [4,5,20,41], considering the treatment times of 2, 4, 8, 16, and 32 min. These samples were denoted as MAH-2, MAH-4, MAH-8, MAH-16, and MAH-32.

Irradiated samples (EI and FI): To obtain the irradiated samples, the set of MAH samples were submitted to two different irradiations: electron beam irradiation (EI) (**Figure 3.1 c**) and femtosecond laser irradiation (FI) (**Figure 3.1 d**). The EI process was conducted in a field emission scanning electron microscope (Supra 35-VP; Carl Zeiss – Germany), using an acceleration voltage of 30 kV for 2 minutes, the parameters were selected based on experiments reported in the references [24,28,30]. The samples obtained through this process were denoted as EI-2, EI-4, EI-8, EI-16, and EI-32.

Regarding the femtosecond laser irradiation, the procedure is according to Protocol I reported in reference [29], using a titanium/sapphire laser (Femtopower Compact Pro, Femto Lasers) with pulses of 30 fs of full width at half maximum, the wavelength of 800 nm, the repetition rate of 1 kHz and fluence of 60 J/cm² in diameter of the order of 20 μm. The obtained samples were denoted as FI-2, FI-4, FI-8, FI-16, and FI-32. Experimental characterizations of the samples are in Supplementary Information.

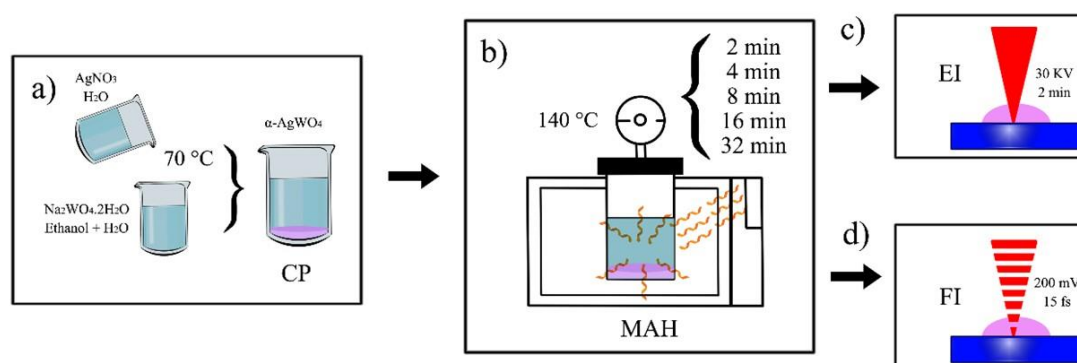


Figure 3.1 Scheme with steps of a) Synthesis by CP method, b) Treatment by MAH method, c) Electron beam irradiation, and d) Femtosecond laser irradiation; to obtain α-Ag₂WO₄ samples.

Model Systems and Theoretical Methods: Density functional theory (DFT) calculations were performed with the CRYSTAL17 program [42]. The B3LYP hybrid functional [43] was used for described the electron-electron interactions combined with the effective core pseudopotentials (ECP) derived by Apra [44] and Corà [45] which have been chosen for described silver and tungsten, respectively, while the oxygen was described with the 8-411d11G basis set [46]. From the experimental results of Rietveld refinements of the CP sample, we derived a theoretical reference model (**opt** – α-Ag₂WO₄) by full optimization of the structural parameters of α-Ag₂WO₄. The accuracy in the evaluation of the Coulomb and exchange was controlled by a set of tolerances with values of 10⁻⁸, 10⁻⁸, 10⁻⁸, 10⁻⁸, and 10⁻¹⁶. A total mesh of 125 *k*-points was employed to sample uniformly the irreducible part of the Brillouin zone. The vibrational modes at the Γ point were calculated by using the numerical second derivatives of the total energy. On the other hand, for the set of MAH,

EI, and FI samples, only the atomic positions were allowed to relax. The relaxed structures were used for the electronic structure calculations. Visualization of the unit cells was performed using the VESTA program [47].

The electronic structure of the (010), (100), (001), (011), (101), and (110) surfaces of α -Ag₂WO₄ were discussed from band gap energy values and the density of states (DOS). Details computational for the calculations of the surface can be found in previous studies [48].

The density broken bonds in the surfaces α -Ag₂WO₄ were calculated as

$$D_b = N_b/A, \quad \text{Eq. 1}$$

where N_b is the number of broken bonds and A is the surface area. The number of broken bonds for each surface was taken from reference [21].

The polyhedron energy band gap energy value for the morphologies of α -Ag₂WO₄ was calculated as follows

$$E_{ap}^{polyhedron} = \sum_i C_i \times E_{gap}^{surf} \quad \text{Eq. 2}$$

where $C_i = A^{surf}/A^{polyedron}$ is the ratio of the surface area (A^{surf}) to the total surface area of the polyhedron ($A^{polyedron}$) and E_{gap}^{surf} is the energy value of the corresponding surface.

3.3 - Results and Discussion

α -Ag₂WO₄ samples obtained by the CP method using 70% of water and 30% of ethanol, followed by treatment with MAH and exposure to EI and FI irradiations, were investigated by FE-SEM, as shown in **Figure B.1** and **Figure 3.2**. Through the CP method, only hexagonal rod-like morphologies were observed, with preferential growth on the y-axis in the (010) direction (**Figure B1**). These characteristics were previously studied by our research group and are reported in reference [48]. In this method, the clusters of silver and tungsten ions solvated with water and ethanol interact randomly in a polarization process of complex clusters, depending on the moment of the permanent dipole of the neighboring clusters. This short-range interaction induces the first links between the crystal symmetry and its order/disorder. Then, to increase the symmetry and order of the crystal, there is a correlation

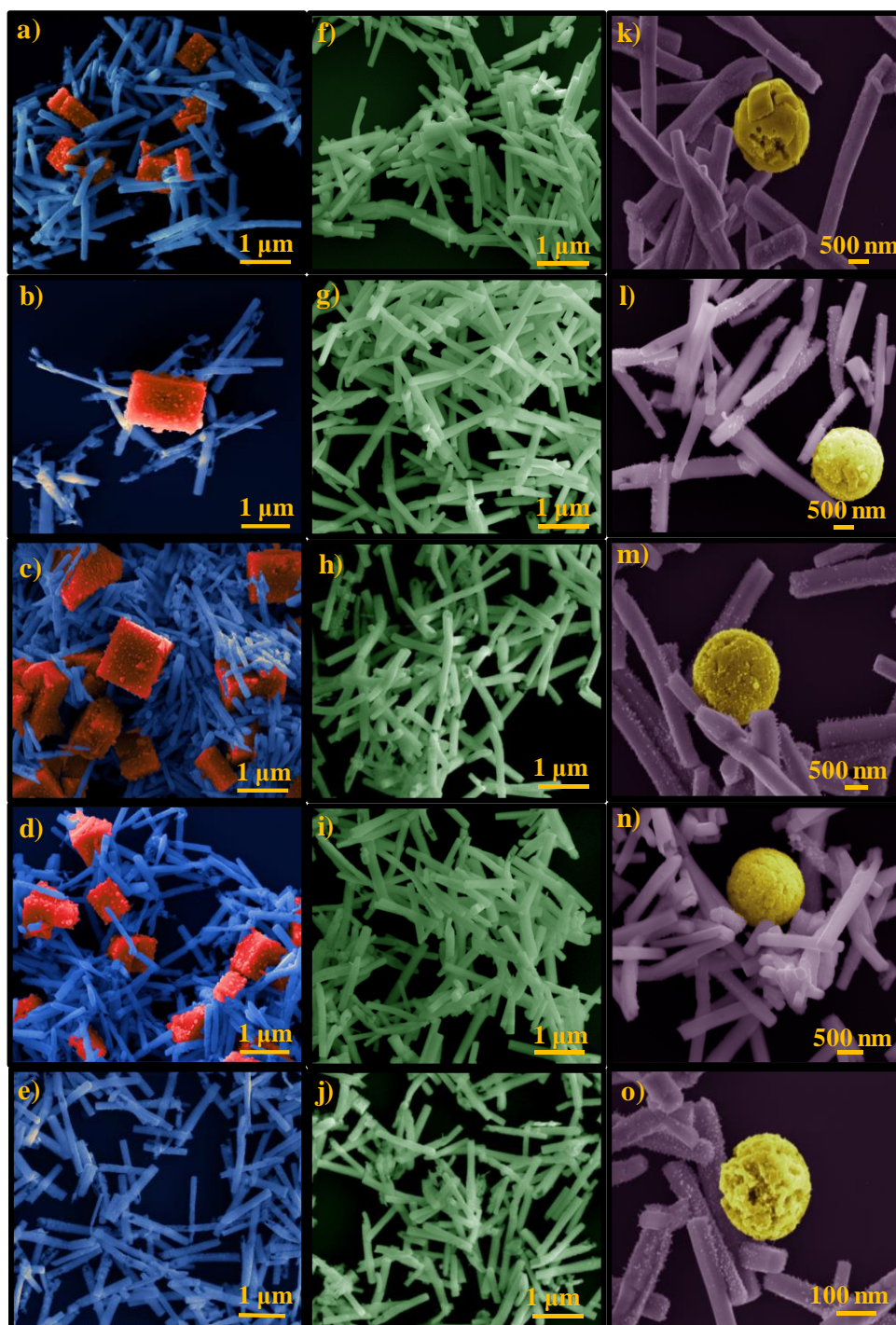


Figure 3.2 FE-SEM images of α - Ag_2WO_4 particles of MAH, EI, and FI. (a-e) heterogeneous morphology obtained after treatment with MAH at different treatment times (2, 4, 8, 16, and 32 min) with the cubes highlighted in orange color and the rods-like in blue color; (f-j) rods-like with homogeneous morphology after EI indicated by green color; (k-o) heterogeneous morphology of rods in violet color and spheres in yellow color after FI.

between the rotation motions of permanent moments in the different complex clusters of silver and tungstate to form the different surfaces.

Theoretical calculations reported in the literature show that the morphological shapes of α -Ag₂WO₄ are formed by the combination of the (010), (100), (001), (110), (101), and (011) surfaces [21,48]. Although the theoretical results establish an ideal parallelepiped-like morphology for α -Ag₂WO₄, characterized by the presence of (010), (100), and (001) surfaces with predominant contributions of the (010) and (100) surfaces and a minor proportion of the (001) surface, experimentally a hexagonal rod-like morphology was observed (**Figure B.1**). **Table 3.1** presents the values of E_{surf} according to R. A. Roca and et al. [48], as well as the surface band gap energy (E_{gap}^{surf}) and the percentage of contribution (% C_i) for each morphology of α -Ag₂WO₄.

The experimental rod-like morphology of α -Ag₂WO₄ for the CP sample composed of the (010), (100), and (101) surfaces were obtained by destabilizing the E_{surf} of the (010), (110), and (100) surfaces from 0.20 to 1.44 Jm^{-2} , 0.65 to 1.50 Jm^{-2} and 0.38 to 0.70 Jm^{-2} , respectively, as well as by stabilizing the (101) and (001) surfaces from 0.68 to 0.23 Jm^{-2} and 0.53 to 0.22 Jm^{-2} , respectively (see **Figure 3.3**).

In the MAH system, the monitoring of the experiment illustrated the time dependence in relation to the morphological evolution of α -Ag₂WO₄ (**Figures 3.2a-e**). Morphologies composed of cube-like (highlighted in orange) and rod-like (indicated in blue) were observed in the samples treated with MAH at 2, 4, 8, and 16 min. Theoretically, the cube-like morphology composed of the (010), (100), and (001) surfaces can be obtained by stabilizing the (100) and (001) surfaces (**Figure 3.3**).

At 32 min of treatment with MAH, a process of redissolution and stabilization of the (101) surface occurred, with concomitant destabilization of the (100) surface. This information allows us to understand how the time variation of the MAH treatment in an alcoholic environment influences particle growth. The microwave radiation induces a structural disorder through the modification of the bond distance, consequently altering the internal rotation barrier and vibration of molecules. In turn, the stabilization of previously

unstable surfaces results in a new morphology [7,9]. Thus, at the highest synthesis time (32 min) the MAH-32 sample (**Figure 3.2e**) presented no cubes – only rods behaving similarly to those obtained in the CP sample (**Figure B1**). It is then believed that at a longer exposure time to microwave irradiation, the cube-like morphology is rearranged to a rod-like morphology.

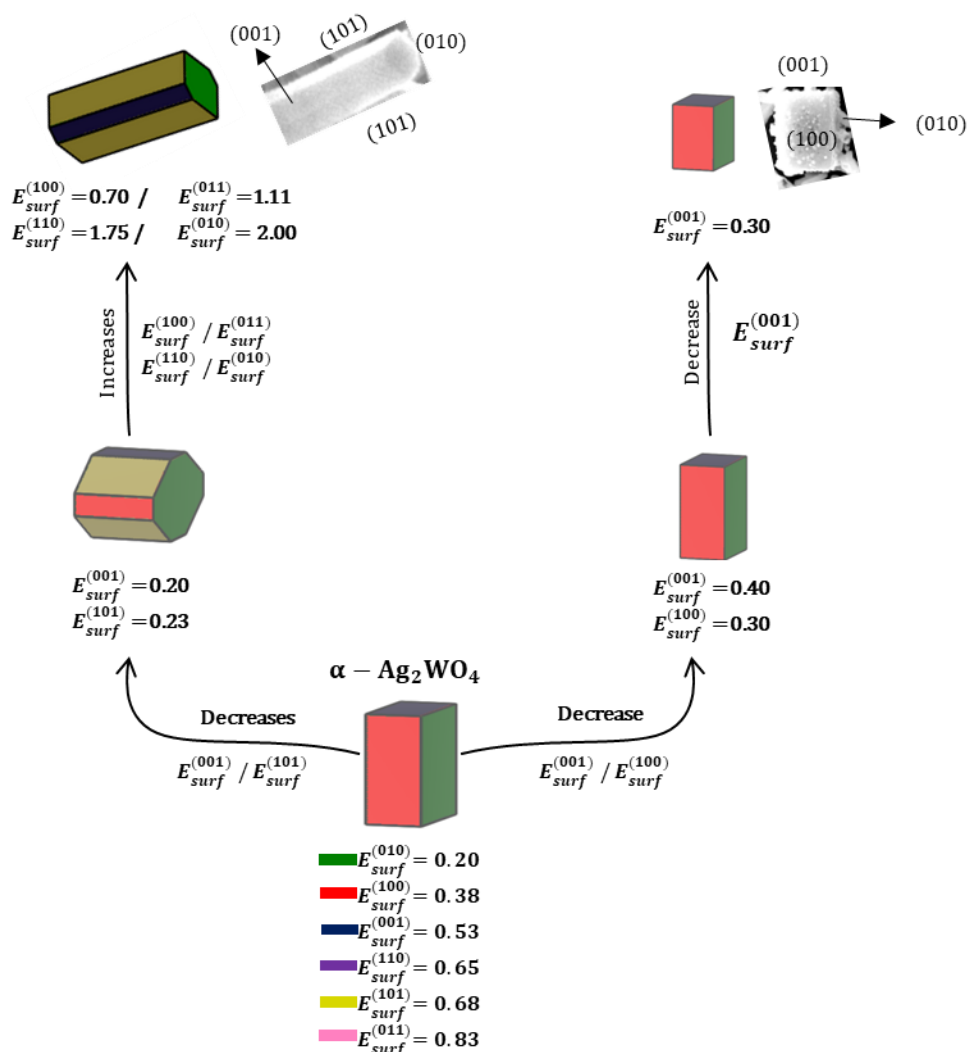


Figure 3.3. Wulff construction for $\alpha\text{-Ag}_2\text{WO}_4$. For comparison, experimental FE-SEM images are shown. E_{surf} values are given in Jm^{-2} .

It can be inferred that the microwave treatment directly interferes with the crystal morphology by either totally or partially dissolving the rod-like crystals or altering the internal rotation movements between the clusters. Thus, in the MAH method, the cube-like morphology is formed by the less energetic surfaces, i.e., (100) and (001), with a decrease in disorder and an increase in symmetry (**Figure 3.3**). The same behavior was observed in

reference [28], in which the MAH method is employed to synthesize α -Ag₂WO₄ and different morphologies were obtained: hexagonal rod-like elongated, cubic-like, and triangular-like shapes.

Table 3.1 Calculated density broken bond (nm^{-2}), surface energy (E_{surf} , Jm^{-2}), surface band gap (E_{gap}^{surf} , eV), percentage of contribution of each surface in the total area (% C_i) and polyhedron band gap energy for the morphologies of α -Ag₂WO₄.

Morphology	Surface	D_B	E_{surf}	% C_i	E_{gap}^{surf}	$E_{gap}^{polyhedron}$
Ideal α - Ag ₂ WO ₄	(010)	4.68	0.20	52.5	1.39	
	(100)	5.83	0.38	27.6	0.48	0.99
	(001)	6.04	0.53	19.8	0.65	
Rod-like α - Ag ₂ WO ₄	(010)	--	1.44	7.3	1.39	
	(001)	--	0.22	13.2	0.65	1.10
	(101)	8.75	0.23	79.4	1.15	
Cube-like α - Ag ₂ WO ₄	(010)	--	0.20	42.9	1.39	
	(100)	--	0.30	28.6	0.48	0.92
	(001)	--	0.30	28.6	0.65	

Under electron beam irradiation, these morphologies change to a unique rod-like morphology (EI samples indicated by green color in **Figures 3.2f-j**), whereas under femtosecond laser irradiation they change to the mixed rod- (violet color) and sphere-like morphologies (yellow color) (FI samples in **Figures 3.2k-o**). The n-type semiconductor, α -Ag₂WO₄, when irradiated with electrons, grows on its surface metallic silver nanowires [10,11,30], thus forming silver vacancies inside the particle and causing a variation in the surface energies of the crystalline structure. Therefore, the value of the (101) surface drops from 0.68 to 0.23 Jm^{-2} (**Figure 3.3**), becoming less energetic, while that of the (100) surface jumps from 0.38 to 0.70 Jm^{-2} , thus becoming more energetic. Even when varying the synthesis times, all samples exhibit

agglomerated nature with characteristics similar to those observed in the CP sample (**Figure B1**). In this micrograph, it can also be observed that the hexagonal rod-like morphology is better defined, with few imperfections. This fact can be considered an indication of the effect of electron beam irradiation on the morphology of α -Ag₂WO₄.

Under EI, the energy of the electron beam is transferred to the sample, causing different phenomena, such as atomic position change, surface distortions, electrostatic charge, and local heating in the crystals. Depending on the voltage and the type of sample electron beam will penetrate a few micrometers or nanometers deep into the sample. In our case, the voltage is 30 kV, whose penetration is in the order of nanometers, causing surface defects and atomic mobility that culminate in the formation of Ag nanoparticles on the surface of α -Ag₂WO₄ [11,49]. On the other hand, when a FI is applied, photons are absorbed by the sample to provoke excitation in the crystal system. To return to the ground state, the system segregates electrons, atoms, and ions from its structure, forming a plasma plume ablation, which is highly energetic. This plume interacts with the irradiated region, promoting energy exchanges, increasing temperature and pressure, accelerating the speed of movement of the species, and ejecting particles. After this highly energetic ablation process, the surface cools very quickly, which modifies the surface structure of the material [35,50].

Regarding the morphology obtained by the FI technique (**Figures 3.2k-o**), it is possible to observe in α -Ag₂WO₄ spherical particles with well-defined edges and irregular extensions, in addition to elongated and slightly curved rods. According to the elementary mapping performed on the FI-8 sample (**Figure 3.4**), both the spheres and the rods are composed of the same proportion of Ag, O, and W atoms, thus confirming the change in particle morphology composed of the same α -Ag₂WO₄ polymorph.

The application of the FI technique leads to the formation of a spherical morphology of α -Ag₂WO₄ powders due to when the femtosecond laser beam interacts with the α -Ag₂WO₄, a nonlinear and multiphoton ionization process occurs, which results in the formation of a plasma plume above the irradiated zone [31,51]. The highly energetic ablation process provokes the breaking of the bonds between the W-O and Ag-O atoms. Further, since the plasma itself

can reach temperature and pressure values of up to 1000 K and 10^{12} Pa, respectively [51], such extreme conditions can trigger the sintering of the material that reminds in contact with the plasma.

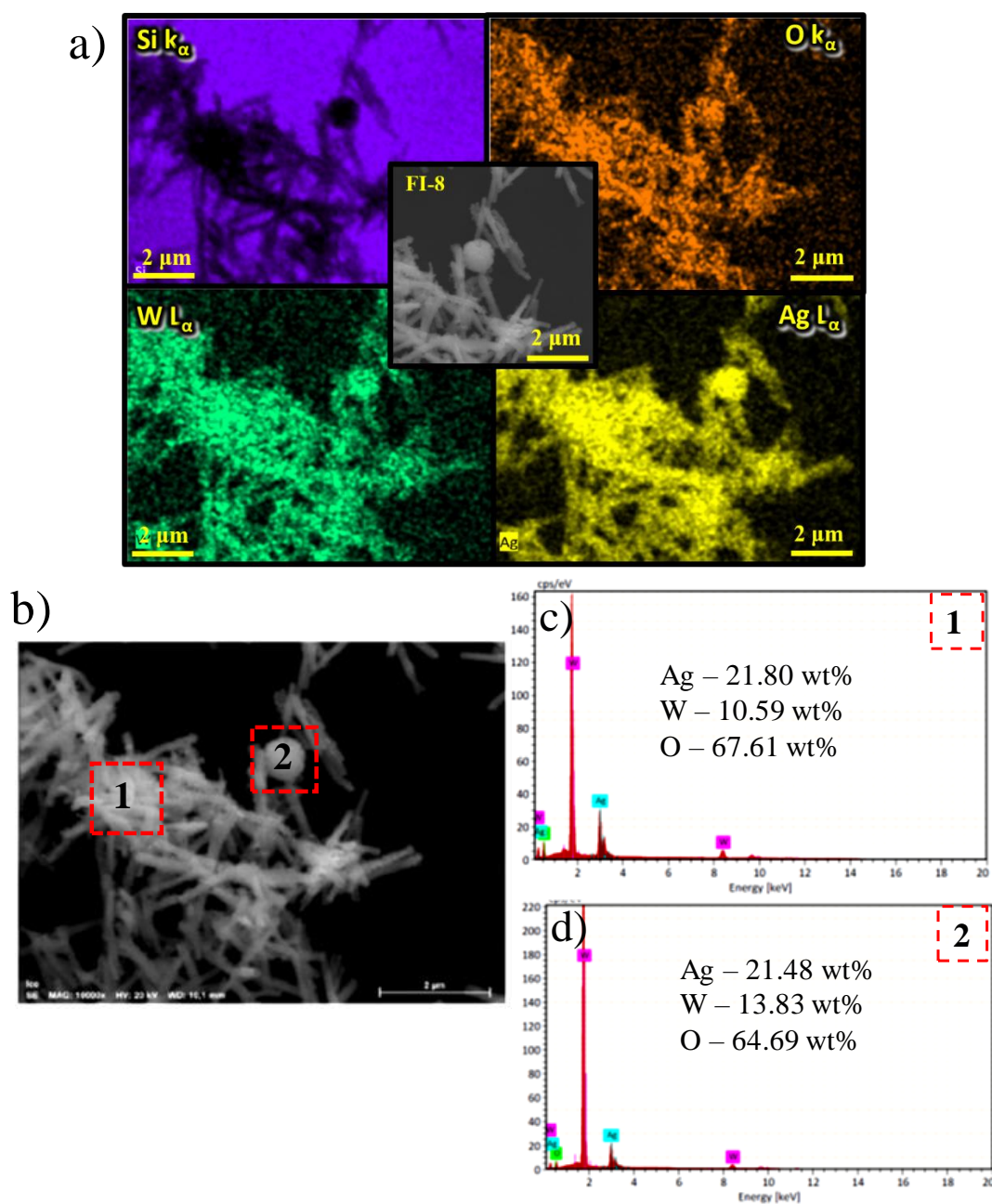


Figure 3.4 a) EDS elemental mapping of the FI-8 sample of Si K_{α} , O K_{α} , W L_{α} , and Ag L_{α} . b) FI-8 sample analyzed by EDS, highlighting the rod- and sphere-like morphologies. c) Rod-like region 1 and d) Sphere-like region 2.

Since the plasma plume, which reaches values up to 1000 K, has a lifetime in the region of the ns [52], the plasma can transfer heat to the material surrounding the irradiation zone. Thus, the material that did not undergo

sintering just experienced a melting process, resulting in the curvature of its edges. This effect is considered to favor the coalescence of the previously observed rods and cubes, giving rise to the morphology of the spheres.

The analysis in **Figure 3.2** suggests that in addition to the morphological changes already discussed, another relevant aspect is observed: the presence of silver nanoparticles on the surface of samples as a result of electron beam and femtosecond laser irradiations. This phenomenon has already been well discussed by our group [10,11,24,31,38–40]. These changes in sample morphologies allow us to understand how the surface structure can affect and modify the PL property of a semiconductor.

The result of Rietveld refinement (**Table B.1**) reveals that the lattice parameters and bond angle of all samples correspond to an orthorhombic structure and $Pn2n$ spatial group, which is in agreement with the crystallographic information file in ICSD 4165 card [53]. Moreover, the R_{Bragg} and χ^2 fitting parameters evidence the accordance between the calculated data and the observed XRD patterns. The Rietveld refinement data show the effect of irradiation on the parameters of the unit cell, which were found to change. In general, when all MAH samples are irradiated by EI and FI, there is an expansion in the cell volume, consequently altering the lattice of the samples.

Figure 3.5 brings a comparison among the geometries for optimized (*opt*- α -AWO), neutral (CP), and irradiated structures (MAH-8, EI-8, and FI-8). From this figure, it is possible to observe variations of the relative positions of the Ag, O, and W atoms on several different constituents $[\text{WO}_6]/[\text{AgO}_y]$ clusters ($y = 7, 6, 4,$ and 2) of α - Ag_2WO_4 . Since the $[\text{AgO}_2]$ and $[\text{AgO}_4]$ clusters are found in the shell of the unit cell, changes are expected as a result of the strong interaction caused by irradiation, leading to nucleation and formation of metallic Ag [24,25]. Thus, the comparison between the *opt*- α -AWO geometries and MAH-8 structures for the sample treated with MAH indicates variations in the Ag–O distances and O–Ag–O angles, mainly in the $[\text{AgO}_2]$ and $[\text{AgO}_4]$ clusters. In the $[\text{AgO}_2]$ cluster, Ag–O increases from 2.246 to 2.461 Å, while O–Ag–O decreases from 174.42 to 145.05°. In the case of the Ag–O bond in $[\text{AgO}_4]$ clusters, an increase in two bond distances is observed. When the MAH-8 sample is exposed to EI, both Ag–O distance and O–Ag–O angle in the $[\text{AgO}_2]$

cluster remain almost unchanged, going from 2.461 to 2.455 Å and from 145.05 to 147.42°, respectively, whereas the Ag–O distance in the [AgO₄] clusters undergoes increases. On the other hand, when a femtosecond laser is applied, the Ag–O distance in the [AgO₂] cluster decreases from 2.461 to 2.193 Å, while the O–Ag–O angle increases from 145.05 to 170.42°. Regarding the [AgO₄] clusters, it is possible to note a shortening average of the Ag–O distance. With respect to the different types of [WO₆] clusters, in all cases, the W–O bond distances of the irradiated samples undergo variations corresponding to W1, in which an average lengthening is observed.

A careful analysis of the Ag–O and W–O bond distances for all samples were performed, and the observed values are listed in **Table B.2**. From **Figure 3.5** and the values in **Table B.2**, we can infer that the MAH treatment induces a larger structural organization in the α -Ag₂WO₄, which is evidenced through the average lengthening of the Ag–O and W–O bonds in the [WO₆]/[AgO_y] clusters ($y = 7, 6, 4,$ and 2). Considering the EI, it can be noted that the irradiation with electrons leads to structural changes in the [AgO₄] and [W1O₆] clusters. On the other hand, FI induces an average shortening of Ag–O and an average lengthening of W1–O bond distances in the clusters of α -Ag₂WO₄ when compared with both MAH samples and the optimized system. These results explain the constant changes in the crystal lattice and the size reduction of [AgO_y] clusters proposed by our group [22], which may also be induced by rod-to-sphere morphology changes in the irradiated samples.

To investigate the effect of irradiation on the particle surface, XPS measurements were conducted. Such analyses were performed in the samples that had their morphology and the PL property changed, that is, MAH-8, EI-8, and FI-8.

Figure 3.6 shows the high-resolution spectra of O 1s, which were fitted with three components. The strong peak around 530.03 eV, 529.83 eV, and 530.07 eV for the MAH-8, EI-8, and FI-8 samples, respectively, are attributed to the O atom in the α -Ag₂WO₄ lattice.

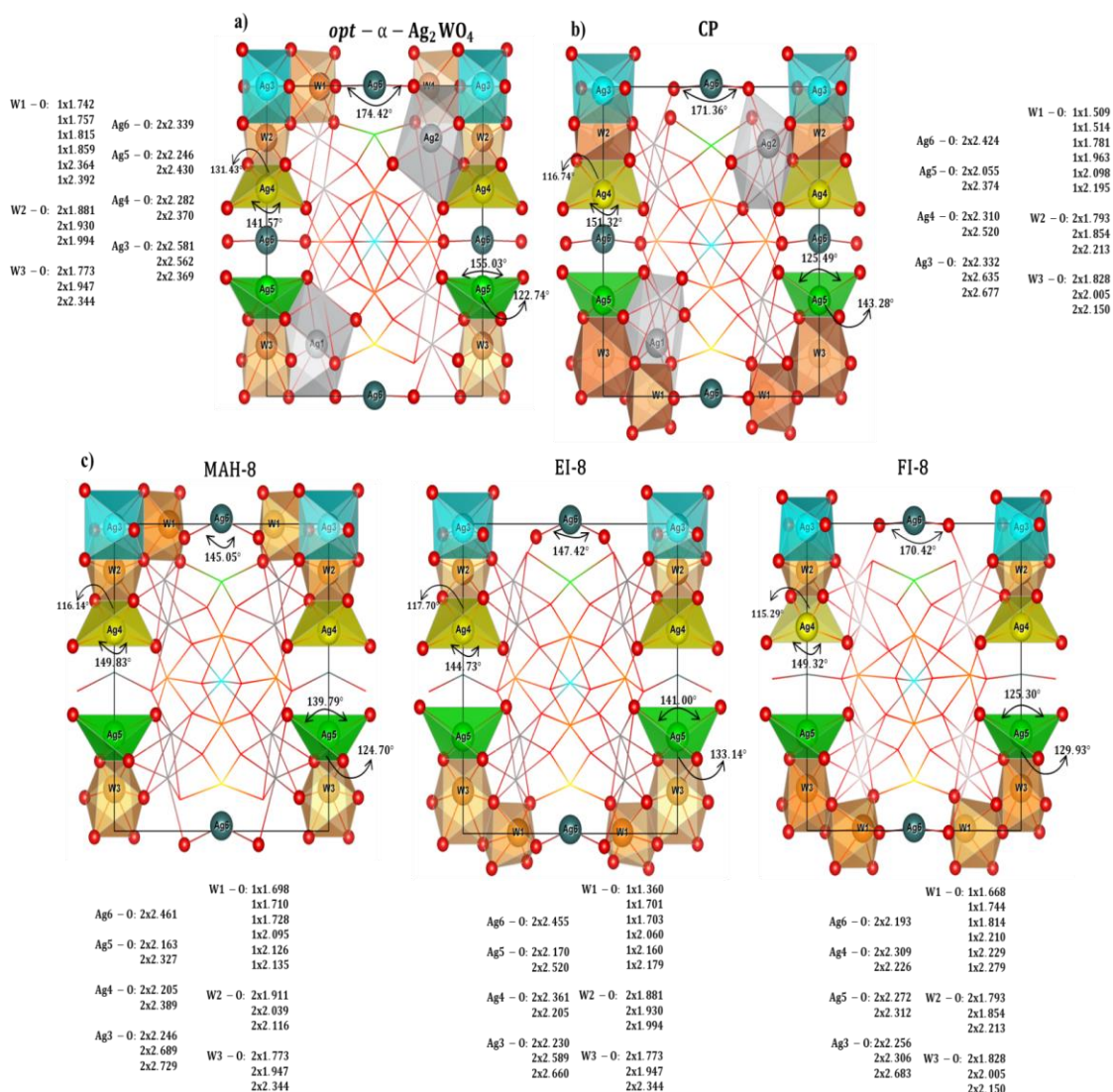


Figure 3.5. The geometry of a) $opt - \alpha - Ag_2WO_4$, b) CP, and c) irradiated (MAH-8, EI-8, and FI-8) structures.

The peak at 531.43 eV, 531.54 eV, and 531.92 eV, respectively, are assigned to oxygen defects in the lattice, such as oxygen vacancies (V_O) [54]. Lastly, the peak in the high binding energy, i.e., above 533 eV, is related to adsorbed oxygen on the surface [54,55]. Changes in the profile of the high-resolution spectrum of O $1s$ indicate a high percentage of adsorbed oxygen on the surface of the EI-8 and FI-8 samples in comparison with MAH-8. Additionally, there is a decrease in the area percentage of the lattice oxygen to 69.97% for MAH-8, 48.00% for EI-8, and 37.66% for FI-8, as well as an increase in the area percentage ascribed to defect oxygen to 20.98%, 27.88%

and 38.10% for the MAH, EI and FI samples, respectively. This indicates a possible formation of oxygen vacancies in the EI and FI samples. The vacancies formed are a charge compensation due to destabilization of the (010) surface along the transformation of morphology from cubes-like into rods-like.

Furthermore, surfaces can be stabilized by reducing surface charge density via different mechanisms: creating surface states, redistributing charge between atoms, removing atoms, adding charged impurities to the surface, or creating faces [56,57]. In the process of electron beam and femtosecond laser irradiations, we observed the destabilization of the surface (010), by the conversion of cubic particles into rods, which was compensated by the removal of surface oxygen atoms and by chemoadsorption of species (O^- and O^{2-}) on the surface, according to the XPS results.

The increment in oxygen vacancies and impurities, via FI, may be related to the fact that the experiment is carried out in an environment, which allows the exchange of charges and species. It is known that the greater exposure of a given crystalline surface influences the properties of materials [58]. An analysis of the theoretical results renders that the (010) surface presents the highest value of surface energy in the rod morphology. Extrapolating this data to the literature [58], we suppose that to compensate for the energetic instability, superficial oxygen vacancies were created.

Figure B.2a shows that the Ag $3d$ spectra were better fitted using one component. The high-intensity peaks located at approximately 368 eV and 374 eV are related to the $3d_{5/2}$ and $3d_{3/2}$ orbitals, respectively, with Ag^+ binding energy. No significant changes were observed among the spectra of the samples.

The XPS technique also provided information on the chemical environment of the W element, which is considered to be the lattice-forming atom. **Figure B.2b** displays the XPS spectra of the W $4f$ for the MAH-8, EI-8, and FI-8 samples. The binding energy corresponds to the $4f_{7/2}$ and $4f_{5/2}$ orbitals of W^{6+} in the α - Ag_2WO_4 lattice [4,59,60]. The XPS spectra reveal a similar profile in all samples, with no changes in the oxidation state or chemical environment of the structural W atom, nor even for the EI and FI samples. Therefore, it can be concluded that the irradiation process changes the environment around oxygen atoms due to the formation of metallic Ag and

V_O vacancies, consequently leading to distortions in the angle and bond distance of the Ag and W clusters (**Table B.2**).

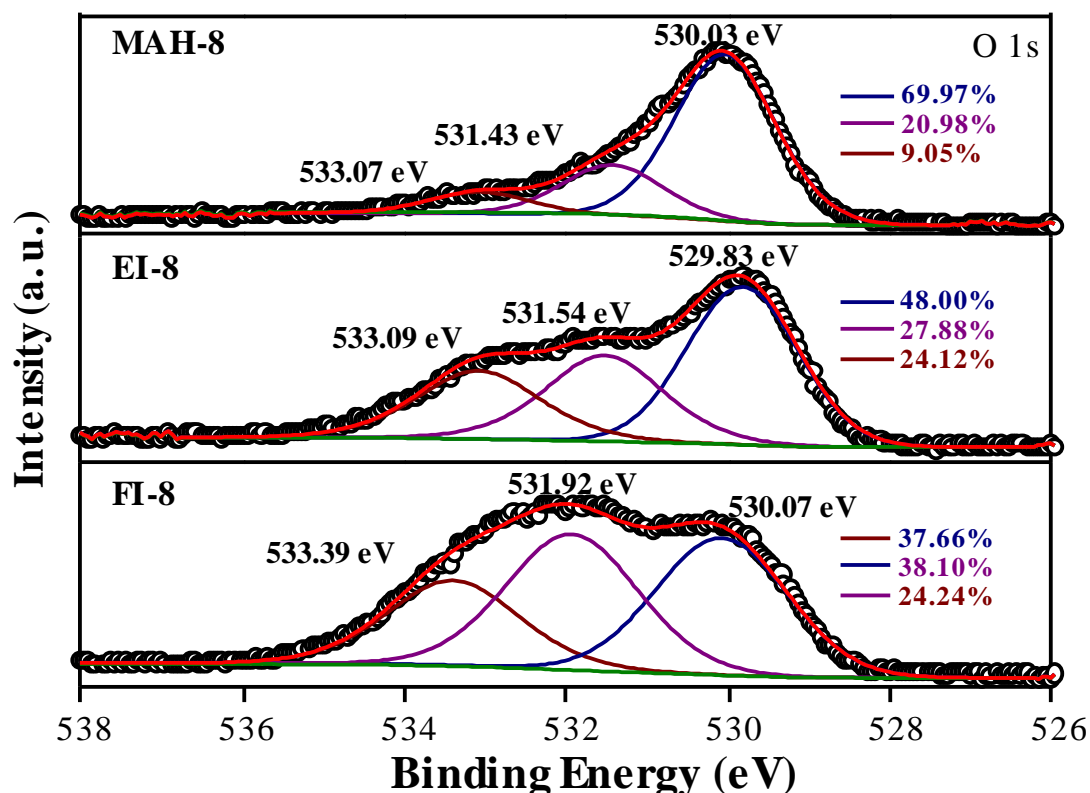


Figure 3.6. High-resolution XPS spectra of O $1s$ for the MAH-8, EI-8, and FI-8 samples.

Figure B.3 displays the Raman spectra in the range of 60-960 cm^{-1} at room temperature. According to Turkovič et al. (1977) [61], there are 21 known Raman modes for $\alpha\text{-Ag}_2\text{WO}_4$ ($6A_{1g}$, $5A_{2g}$, $5B_{1g}$, and $5B_{2g}$). As it can be observed in **Figures B.3a-d**, six Raman modes were detected for all samples ($1A_{1g}$, $1A_{2g}$, $3B_{1g}$, and $1B_{2g}$); the remaining modes were not detectable experimentally because of their low intensities. External vibrational modes of interaction between silver and tungstate ion and $[\text{AgO}_y]$ ($y = 7, 6, 4, 2$) clusters can be identified between 100 and 500 cm^{-1} , whereas internal vibrational modes assigned to the vibrations in the $[\text{WO}_6]$ clusters can be detected between 500 and 1000 cm^{-1} [28,37,62]. It is possible to observe in both materials two intense bands: one at 102 cm^{-1} , attributed to the stretching of $T'(\text{Ag}^+/\text{W}^{6+})$

binding [63], and another at 877 cm^{-1} , assigned to the symmetrical stretching of the W–O bond in the octahedral $[\text{WO}_6]$ cluster [28].

The comparison between the relative experimental and theoretical positions of these vibrational modes is illustrated in **Figure B.3e** and summarized in **Table B.3**, confirming the good agreement between the experimental and theoretical modes.

Following the Raman discussion on the short-range structural disorder, XANES allowed us to visualize a local disorder, which in our case was around the tungsten atom. In the past decade, our research group has employed the XANES technique to study the local structure of various semiconducting metal oxides, such as tungstates, titanates, and vanadates among others [19,64–68].

Herein, we performed XANES measurements to investigate the effect of irradiation on the local structure around W atoms. **Figure B.4a** displays the W-L1 XANES spectra of the as-prepared CP sample and some standards used as reference samples (Na_2WO_4 , WO_2 , and monoclinic WO_3). In **Figure B.4a**, it is possible to observe a pronounced peak (here denoted as P1) in the Na_2WO_4 spectrum, more specifically in the pre-edge region, as well as a shoulder in the m- WO_3 standard and the CP sample spectra. The physical origin of such electronic transition (peak P1) is described elsewhere [19,69,70].

It is well established that an intense pre-peak in the W-L1 edge XANES spectrum has been found in materials constituted by tetrahedral units (WO_4), such as the Na_2WO_4 compound [5,70]. The electronic transition responsible for P1 pre-peak is forbidden in the materials that exhibit regular $[\text{WO}_6]$ units. However, compounds presenting non-regular octahedral symmetry (distorted WO_6 clusters) have been found to present a less intense pre-peak similar to that in the WO_3 spectrum [69,70]. From the analysis of the spectrum of the CP sample, it is possible to observe its similarity with the WO_3 standard spectrum. It is then plausible to affirm the presence of distorted $[\text{WO}_6]$ clusters in the as-prepared CP sample. Furthermore, by comparing the spectra of the $\alpha\text{-Ag}_2\text{WO}_4$ samples (**Figure B.4b**) it is evident the similarity with the XANES spectra (both in the pre- and post-edge regions). Such behavior reveals that the microwave-assisted hydrothermal treatment, as well as the irradiation

processes (EI and FI), resulted in samples constituted by distorted octahedral WO_6 clusters.

The experimental optical band gap was estimated using the Wood-Tauc relation [71,72] and the Kubelka-Munk equation [72,73], evidencing a slight variation from 3.09 to 3.32 eV (**Figure B.5**) for the MAH, EI, and FI samples. The experimental results show that when the CP sample is submitted to MAH treatment for 2 minutes, the band gap value decreases from 3.13 eV to 3.08 eV. In contrast, for the MAH-4, MAH-8, MAH-16, and MAH-32 samples, the band gap increases. Later, when these samples are under EI, is observed that except for the EI-2 sample, the band gap decrease in all cases. For the FI-2 and FI-4 samples present an increase in the band gap, while for the FI-8, FI-16, and FI-32 samples, an opposite effect can be sensed. Structural order-disorder effects induced by the radiation as well as the morphology, time process, and shape powder can explain the band gap decrease/increase of $\alpha\text{-Ag}_2\text{WO}_4$.

The electronic structure of $\alpha\text{-Ag}_2\text{WO}_4$ was analyzed from the partial density of states (PDOS) of the $4d$, $5d$, and $2p$ orbitals of Ag, W, and O atoms, respectively (**Figure 3.7**), where the valence band maximum (VBM) is set to zero. In terms of contributing states, the representation is similar for all samples, according to the composition of the valence band (VB) and conduction band (CB) of the different samples. As already known, for $\alpha\text{-Ag}_2\text{WO}_4$ the VB is formed by the hybridization of $4d_{xy}$ and O $2p_z$ orbitals, whereas the bottom of the CB is mainly composed of W $5d$ orbitals, more specifically $5d_{z^2}$ orbitals. However, differences in topology occur among the PDOS of neutral and irradiated samples. In the PDOS of the neutral sample, there is discontinuation in the VB, leading to two distinct Ag $4d$ blocks. Such characteristic is maintained in the EI-8 sample, while in the PDOS of the MAH-8 and FI-8 samples the double-peak structure disappears.

In the MAH-8 and FI-8 samples (**Figure 3.7c**), localized states of the O $2p_x$, $2p_y$, and $2p_z$ and Ag $4d_{xy}$ orbitals are evidenced in the Fermi region, as well as localized $5d_{x^2-y^2}$ and $5d_{z^2}$ orbitals forming the bottom of the CB in these samples. The localized density of $2p$ and W $5d$ states situated at the Fermi level and the bottom of the CB, respectively, favors the electronic transfer from the O $2p$ to W $5d$ states, which are necessary for the excitation process of the

tungstate groups. These observations in the electronic properties of the different samples are associated with the structural disorder induced by the irradiation in the α - Ag_2WO_4 lattice, as seen in **Figure 3.5**.

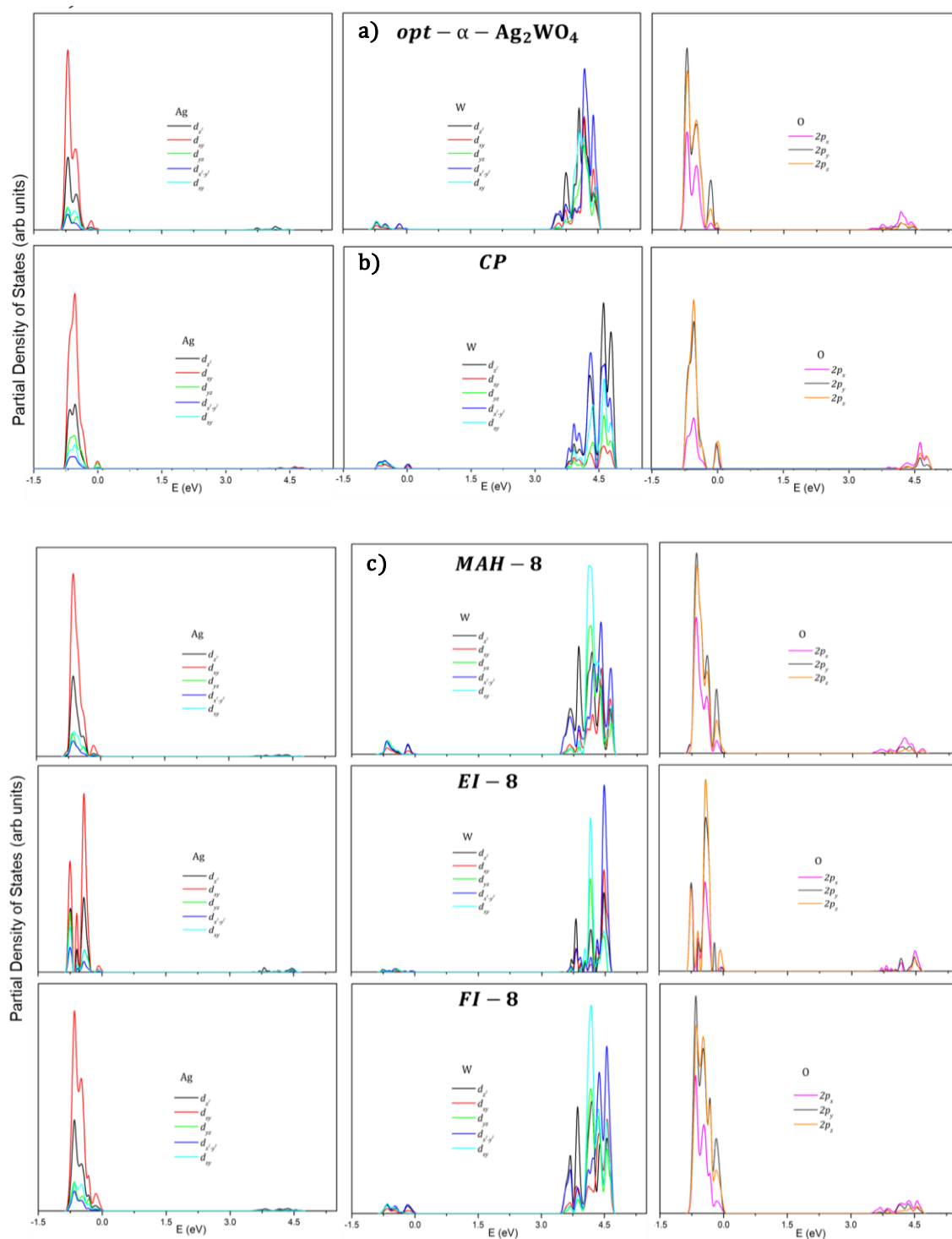


Figure 3.7. Partial density of states projected on the $4d$, $5d$, and $2p$ orbitals of Ag, W, and O atoms, respectively, for a) $\text{opt-}\alpha\text{-Ag}_2\text{WO}_4$, b) CP, and c) irradiated (MAH-8, EI-8, and FI-8) samples.

Figure 3.8 shows the PL spectra of α - Ag_2WO_4 samples measured at room temperature and excited at 355 nm. The PL spectra encompass the whole visible region and part of the near-infrared region, presenting a broadband profile. The small changes in the profile of the PL spectrum between the same group are related to different degrees of order/disorder in the O–Ag and O–W bond lengths. Therefore, by analyzing the PL spectra we can understand how the MAH treatment time, and electron beam and femtosecond laser irradiations affect the emission spectrum of α - Ag_2WO_4 .

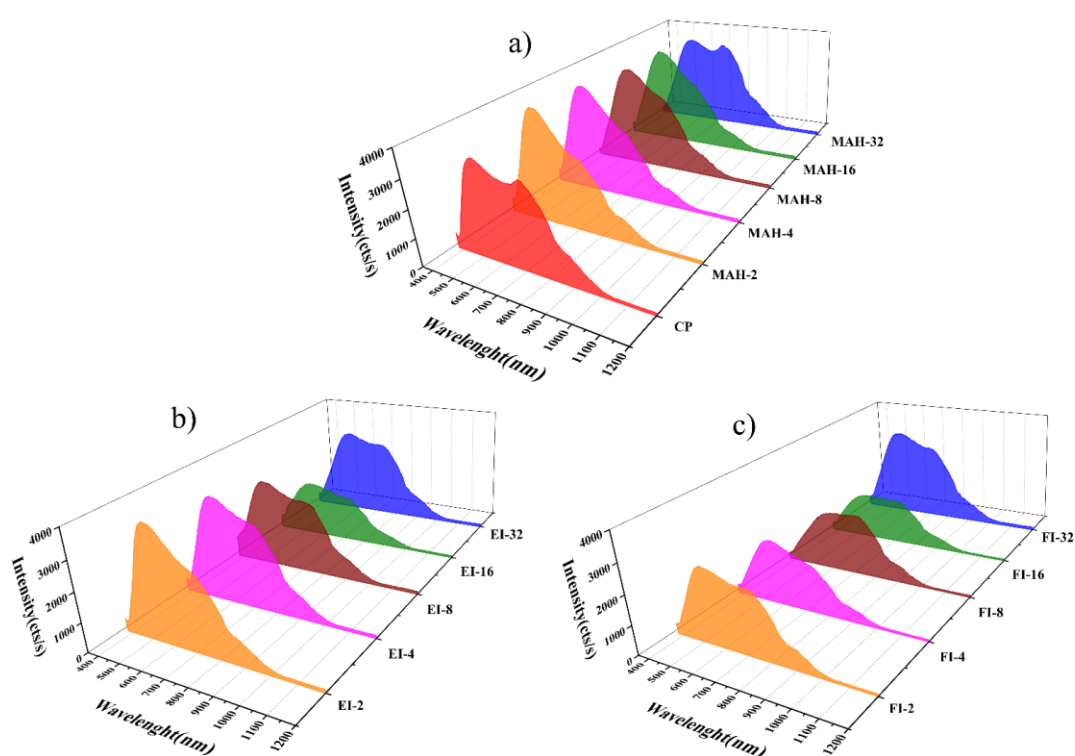


Figure 3.8. PL spectra of the samples obtained by a) the CP method, treated with MAH, and irradiated by b) EI and c) FI.

The CP and EI samples with rod-like morphology (**Figure B2** and **Figure 3.2f-j**) have two maximum emission centers: around the green (550 nm) and the red (733 nm) regions (**Figure 3.8a,b**). The FI sample with rod- and sphere-like morphologies presented the same emission centers (**Figure 3.2k-o** and **Figure 3.8c**). When the sample is submitted to MAH at synthesis times between 2 and 16 min, two types of morphologies are observed (rod- and cube-like, **Figures 3.2a-d**), and the maximum emission center around 550 nm is

avored (**Figure 3.8a**). However, the sample treated with MAH at a prolonged synthesis time of 32 min, in addition to only hexagonal rod-like particle morphology, presents two maximum emission centers similar to those of the CP sample.

It is well known that the PL property of α -Ag₂WO₄ is strongly correlated by photogenerated electron-hole pair processes and in terms of the electronic transition between the VB ($2p$ levels of oxygen atoms and $4d$ level of silver atoms) and the CB ($5d$ levels of tungsten atoms) as well as the contribution of intermediate levels between the VB and CB [22,32,33,66,74].

The blue band is attributed to the radiative transition from the O_{2p} states to the W_{5d} states while the green band is due to the electronic transition from the Ag⁺-V_O defects level to the VB [62]. Blue/Green emission was also related to distorted [WO₆] octahedral, while red emission to the [AgO_y] ($y = 2, 4, 6, \text{ and } 7$) clusters that form complex vacancies, inducing more disorder and deeper defects in the forbidden band gap [32,38,75].

Furthermore, the [AgO_y] ($y = 2, 4, 6, \text{ and } 7$) and [WO₆] clusters in pairs have extrinsic defects, which are linked to order-disorder effects in the electronic structure, surface, and interfaces, which create additional energy states above the VB and below the CB, which decrease the band gap [32,66]. However, a specific assignment of surface and the clusters that are present on each surface that contributes to PL emission has not been observed. Here, we can observe the influence of particle morphology and surface band gap since the distortions in the lattice favor different distributions of electronic state in the surface (**Figure 3.9**).

To analyze the difference between the emission spectrum and the contribution of each surface (**Figure 3.9**), a comparison among the MAH-8, EI-8, and FI-8 samples with the cube-, rod- and sphere-like morphologies, respectively, is presented in **Figure 3.10**. Since each of the surfaces of α -Ag₂WO₄ presents a different band gap energy (E_{gap}^{surf}) value, it is expected that each surface has a specific contribution in the PL property. This can be justified by the fact that each surface is quite different in terms of the coordination number of atoms, the distance between adjacent atoms, and available electron density [22,30].

The theoretical E_{gap} values of surfaces and the rod- and cube-like morphologies of α - Ag_2WO_4 are listed in **Table 3.1**. According to the results, all surfaces studied show E_{gap}^{surf} values reduced in comparison to the E_{gap} value of the bulk.

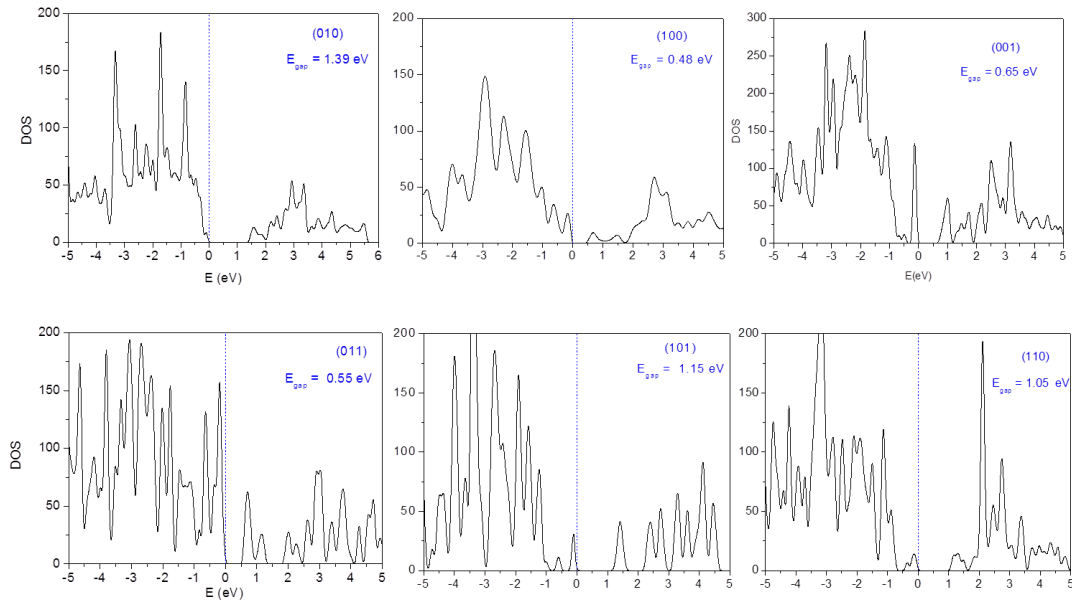


Figure 3.9. The total density of states for the (010), (100), (001), (011), (101), and (110) surfaces of α - Ag_2WO_4 .

The density of defects on the surface can justify the existence of intermediary states in the band region of the bulk, which come from the number of Ag–O and W–O bonds that are broken when a slab surface is created. To quantify the defects on the surface, the density of broken bonds was calculated as $D_b = N_b/A$, where N_b is the number of broken bonds and A is the surface area. The results corroborate that those surfaces with higher D_b values present the lowest band gap (**Table 3.1**) and consequently, intermediary states (**Figure 3.9**).

Regarding the $E_{gap}^{polyhedron}$ for each experimental morphology, the results reveal that in passing from ideal to the experimental rod-like morphology, the $E_{gap}^{polyhedron}$ value increase from 0.99 eV to 1.10 eV due to the appearance of the (101) surface which comes to dominate the Wulff construction (79.4 %) for the rod-like morphology and has a band gap of 1.15 eV. The (010) and (001)

surfaces are also exposed in this morphology in a lower proportion (7.3 % and 13.2%, respectively).

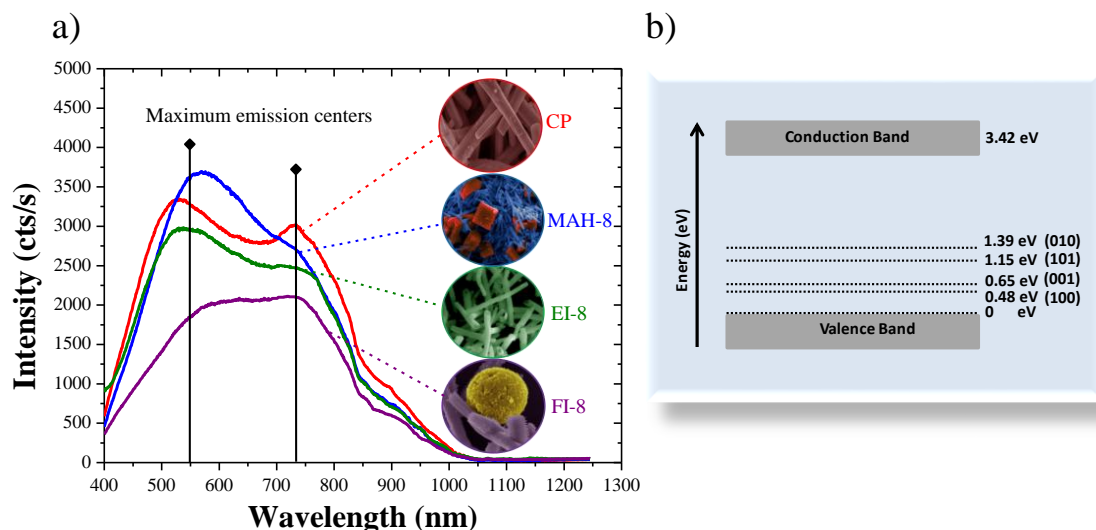


Figure 3.10 (a) PL spectra and maximum emission centers of the CP, MAH-8, EI-8, and FI-8 samples. (b) Comparative diagram of the band gap value of the optimized structure (3.42 eV) and band gap values for (100), (010), (001), and (101) surfaces.

In the case of the passing from ideal to the experimental cube-like morphology, the $E_{gap}^{polyhedron}$ decrease from 0.99 eV to 0.92 eV at the time that (001) and (100) surfaces that have the lower band gap values 0.65 eV and 0.48 eV, respectively, increase their contribution (28.6 % each one) to the cube-like morphology that exposed the (010) surface (42.9 %) which have band gap (1.39 eV). It is worth nothing that theoretical values of band gap energy are not the same that those obtained experimentally because the experimental techniques used for such measurements considering the effect bulk/surface of the material and in the calculations have been considered only the exposed surface structures at the morphology.

Figure 3.10a shows that both CP and EI-8 samples are composed only of rod-like morphologies. The PL spectrum for the CP and EI-8 samples showed two maximum emission centers – around 550 nm and 733 nm – regions. In the case of the MAH-8 sample, it is composed of both cube- and rod-like morphologies and although the PL spectrum also present two

emission centers, is observed that the maximum emission center around 550 nm is favored while the emission center is 733 nm present intensity lower. Finally, the sample irradiated by femtosecond laser (FI-8) with rod- and sphere-like morphologies presented an equilibrium in the maximum emission centers with a slight shift to the red region. Based on these results, we can conclude that (010) and (101) surfaces contribute to the emission centers at 550 nm and 733 nm, respectively.

As previously mentioned, (010) surface has the highest band gap, therefore it tends to contribute to the highest energies emission (**Figure 3.10b**), in addition, is present in both morphologies, see **Table 3.1**, and is the main component of the cube-like morphology, thus, the presence of both cube- and rod-like morphologies in the sample contributed to the emission to 550 nm. In contrast, (101) surface is the main component of the rod-like morphology, and therefore the sample only with rod shows a defined emission at 733 nm. The highest intensity of emission in 550 nm is associated with the presence of localized states in the forbidden band gap due to (010) surface, see **Figure 3.9** and **Figure 3.10b**, which favored the probability of the transition in this surface.

As has been established in the (101) surface are present distorted $[WO_6]_d$ cluster, and the under-coordinated $[AgO_5 \cdot 2V_O^x]$, $[AgO_4 \cdot 3V_O^x]$, and $[WO_5 \cdot V_O^x]$ clusters. The complete distorted $[WO_6]_d$ clusters are considered as a source of electrons due to while the under coordinated $[AgO_5 \cdot 2V_O^x]$, $[AgO_4 \cdot 3V_O^x]$ clusters, and $[WO_5 \cdot V_O^x]$ clusters supporting charge positive are considered a source of the hole [76,77].

In the case of the (010) surface complete distorted $[WO_6]_d$ and $[AgO_4]_d$ clusters present in the surface are a source of electrons while under-coordinated $[AgO_5 \cdot 2V_O^x]$ clusters are a source of holes. Thus, the transfer electron-hole occur from complete distorted clusters to under-coordinated $[AgO_5 \cdot 2V_O^x]$ clusters, the above also explain the contribution of the (010) surface to the PL property [21].

Moreover, the cube- and rod-like morphologies have a stable (001) surface, which has the E_{gap}^{surf} (0.65 eV), see **Table 3.1** and **Figure 3.10b**. The (001) surface has a percentage of total area contribution in both morphologies

of 28.6% and 13.2%, respectively. The (001) surface has $[WO_5 \cdot V_O^x]$, $[AgO_5 \cdot 2V_O^x]$, $[AgO_4 \cdot 3V_O^x]$, and $[AgO_4 \cdot 2V_O^x]$ clusters [21]. The cube-like morphology also has a stable (100) surface, which has the lowest E_{gap}^{surf} (0.48 eV), **Figure 3.10b**. The (100) surface has $[WO_4 \cdot 2V_O^x]$, and two $[AgO_5 \cdot 2V_O^x]$ clusters [21].

In general, the samples with cube-like morphologies showed a maximum center emission in the green region, while those with particles with only rod-like morphology showed two maximum emission centers (in the green and red regions). Differently, the sphere-like morphology presented an equilibrium in the emission centers. The PL behavior demonstrates the influence of many factors, such as the orientation between particles, the variations in the particles size distribution, the morphology of the particles, and surface defects [32].

The XYZ color space created by the International Commission on Illumination (abbreviated as CIE) serves as a standard reference to represent the color emitted by the materials, and this color is expressed by a resulting chromaticity symbolized by the coordinates (x, y) [62]. The chromaticity coordinates x and y under excitation of 355 nm were obtained in the CIE XYZ color space (**Figure B.6**), and the detailed information is shown in **Table B.4**.

The MAH group revealed variation in their color from orange to red (**Figure B.6a**) due to the synthesis time, which disorganized the $[AgO_y]$ clusters. The CIE diagram of the EI and FI groups also showed a color variation from orange to red (**Figure B.6b**). Among the samples submitted to femtosecond laser irradiation, the FI-32 was found to be the most resistant to the laser action, remaining practically unchanged when compared to the MAH-32 (**Figure B.6c** and **Table B.4**). The other samples migrated from orange to red, following what was observed for samples irradiated by electrons. Therefore, the PL measurements demonstrated that microwave, electron beam, and femtosecond laser irradiations altered the electronic density of the bulk and surface since the behavior of the samples changed after irradiation. However, the sample obtained at the longest synthesis time did not show variation in the density of V_{Ag} and V_O vacancies when subjected to electron or

femtosecond irradiation, which is possibly related to its more stable rod-like morphology.

3.4 - Conclusions

In summary, in this work, we discussed the influence of morphology, surface band gap, and microstructure on the PL property of α - Ag_2WO_4 samples obtained by the CP method, followed by treatment with MAH at different synthesis times and two different irradiation processes: electron beam and femtosecond laser. The experimental and theoretical study clarifies the important relationship between the DOS of different surfaces and the PL property. It was observed that the use of different ways of treating the samples successfully changed the surface characteristics, microstructure, and electronic density of the α - Ag_2WO_4 materials. Electron beam and femtosecond laser irradiations were found to cause expansion of the unit cell, form oxygen vacancies on the surface, change the angle and distance between O–Ag and O–W bonds, and modify the particle morphology to rod-, cube- and sphere-like. The theoretical calculations showed how changes in the microstructure, morphology, and surface band gap values can alter the distribution of electron density, and consequently the emission centers. Cube-like morphology shows a high contribution of the (010) surface, while rod-like morphologies showed the contribution of (010) surface and (101) surface. Moreover, the sample submitted to a longer synthesis time of 32 min in the microwave system presented the most stable rod-like morphology and high resistance to the disorder of the network-modifying $[\text{AgO}_y]$ clusters. Therefore, the more ordered the network-forming $[\text{WO}_6]$ clusters, the more difficult it will be to introduce defects. For this reason, no significant changes were observed in the PL property. These results enrich the literature regarding the effect of different techniques associated with microstructure, morphology, and band gap energies on the PL properties of semiconductor materials.

3.5 - References

- [1] Y. Li, Y. Li, S. Ma, P. Wang, Q. Hou, J. Han, S. Zhan, Efficient water disinfection with Ag₂WO₄-doped mesoporous g-C₃N₄ under visible light, *Journal of Hazardous Materials*. 338 (2017) 33–46. doi:10.1016/j.jhazmat.2017.05.011.
- [2] M. Pirhashemi, A. Habibi-Yangjeh, Preparation of novel nanocomposites by deposition of Ag₂WO₄ and AgI over ZnO particles: Efficient plasmonic visible-light-driven photocatalysts through a cascade mechanism, *Ceramics International*. 43 (2017) 13447–13460. doi:10.1016/j.ceramint.2017.07.049.
- [3] Y. Li, B. Zhu, J. Yu, W. Ho, P. Xia, Fabrication and photocatalytic activity enhanced mechanism of direct Z-scheme g-C₃N₄/Ag₂WO₄ photocatalyst, *Applied Surface Science*. 391 (2016) 175–183. doi:10.1016/j.apsusc.2016.07.104.
- [4] H. Li, Y. Zhou, L. Chen, W. Luo, Q. Xu, X. Wang, M. Xiao, Z. Zou, Rational and scalable fabrication of high-quality WO₃/CdS core/shell nanowire arrays for photoanodes toward enhanced charge separation and transport under visible light, *Nanoscale*. 5 (2013) 11933–11939. doi:10.1039/c3nr03493c.
- [5] A. Kuzmin, J. Purans, Local atomic and electronic structure of tungsten ions in AWO₄ crystals of scheelite and wolframite types, *Radiation Measurements*. 33 (2001) 583–586. doi:10.1016/S1350-4487(01)00063-4.
- [6] N.F.A. Neto, P.M. Oliveira, M.R.D. Bomio, F. V Motta, Effect of temperature on the morphology and optical properties of Ag₂WO₄ obtained by the co-precipitation method : Photocatalytic activity, *Ceramics International*. 45 (2019) 15205–15212. doi:10.1016/j.ceramint.2019.05.006.
- [7] H.P. Marques, A.R. Canário, A.M.C. Moutinho, O.M.N.D. Teodoro, Shaping Ag clusters on Titania, *Journal of Physics: Conference Series*. 61 (2007) 775–779. doi:10.1088/1742-6596/61/1/155.
- [8] B. Liu, Z. Hu, Y. Chen, K. Sun, X. Pan, Y. Che, Ultrafast pulsed laser ablation for synthesis of nanocrystals, *Nanoengineering: Fabrication, Properties, Optics, and Devices IV*. 6645 (2007) 66450R. doi:10.1117/12.736522.
- [9] K.J.Rao, B.Vaidhyanathan, M.Ganguli, P.A.Ramakrishnan. Synthesis of Inorganic Solids Using Microwaves. *Chem. Mater.*, 11 (1999) 882–895. doi: 10.1021/cm9803859
- [10] M.A. San-Miguel, E.Z. Da Silva, S.M. Zanetti, M. Cilense, M.T. Fabbro, L. Gracia, J. Andrés, E. Longo, In situ growth of Ag nanoparticles on α -Ag₂WO₄ under electron irradiation: Probing the physical principles, *Nanotechnology*. 27 (2016). doi:10.1088/0957-4484/27/22/225703.
- [11] J.C. Sczancoski, S.M. Johnson, S. Pereira, E. Longo, E.R. Leite, Atomic diffusion induced by electron-beam irradiation : An in situ study of Ag structures grown from α - Ag₂WO₄, *Crystal Growth & Design* (2018). doi:10.1021/acs.cgd.8b01076.

- [12] Y.J. Zhu, F. Chen, Microwave-assisted preparation of inorganic nanostructures in liquid phase, *Chemical Reviews*. 114 (2014) 6462–6555. doi:10.1021/cr400366s.
- [13] A. Mirzaei, G. Neri, Microwave-assisted synthesis of metal oxide nanostructures for gas sensing application: A review, *Sensors and Actuators, B: Chemical*. 237 (2016) 749–775. doi:10.1016/j.snb.2016.06.114.
- [14] S.C. Motshekga, S.K. Pillai, S. Sinha Ray, K. Jalama, R.W.M. Krause, Recent trends in the microwave-assisted synthesis of metal oxide nanoparticles supported on carbon nanotubes and their applications, *Journal of Nanomaterials*. 2012 (2012). doi:10.1155/2012/691503.
- [15] D. Zhang, Y. Zhang, Y. Fan, N. Luo, Z. Cheng, J. Xu, Micro-spherical ZnSnO₃ material prepared by microwave-assisted method and its ethanol sensing properties, *Chinese Chemical Letters*. 31 (2020) 2087–2090. doi:10.1016/j.cclet.2020.01.004.
- [16] R.E. Newnham, S.J. Jang, M. Xu, F. Jones, This Paper Is a Component Part of the Following Compilation Report : Authored Sections of Proceeding , Annals , Symposia , Etc . However , the Component Should Be Considered Within The Context of the Overall Compilation Report and Fundamental Interaction, *Ceramic Transactions. Volume 21. Proceedings of the Symposium on Microwave Theory and Application in Materials Processing Annual Meetings of the American Ceramic Society (23rd)*. 21 (1991).
- [17] T. Sin Tee, T. Chun Hui, C. Wu Yi, Y. Chi Chin, A.A. Umar, G. Riski Titian, L. Hock Beng, L. Kok Sing, M. Yahaya, M.M. Salleh, Microwave-assisted hydrolysis preparation of highly crystalline ZnO nanorod array for room temperature photoluminescence-based CO gas sensor, *Sensors and Actuators, B: Chemical*. 227 (2016) 304–312. doi:10.1016/j.snb.2015.12.058.
- [18] H.W. Kim, Y.J. Kwon, A. Mirzaei, S.Y. Kang, M.S. Choi, J.H. Bang, S.S. Kim, Synthesis of zinc oxide semiconductors-graphene nanocomposites by microwave irradiation for application to gas sensors, *Sensors and Actuators, B: Chemical*. 249 (2017) 590–601. doi:10.1016/j.snb.2017.03.149.
- [19] L. Cruz, M.M. Teixeira, V. Teodoro, N. Jacomaci, L.O. Laier, M. Assis, N.G. Macedo, A.C.M. Tello, L.F. da Silva, G.E. Marques, M.A. Zaghete, M.D. Teodoro, E. Longo, Multi-dimensional architecture of Ag/ α -Ag₂WO₄ crystals: insights into microstructural, morphological, and photoluminescence properties , *CrystEngComm*. 22 (2020) 7903–7917. doi:10.1039/d0ce00876a.
- [20] L.O. Laier, M. Assis, C.C. Foggi, A.F. Gouveia, C.E. Vergani, L.C.L. Santana, L.S. Cavalcante, J. Andrés, E. Longo, Surface-dependent properties of α -Ag₂WO₄: a joint experimental and theoretical investigation, *Theoretical Chemistry Accounts*. 139 (2020) 1–11. doi:10.1007/s00214-020-02613-z.
- [21] N.G. Macedo, A.F. Gouveia, R.A. Roca, M. Assis, L. Gracia, J. Andrés, E.R. Leite, E. Longo, Surfactant-Mediated Morphology and Photocatalytic Activity of α -Ag₂WO₄ Material, *Journal of Physical Chemistry C*. 122 (2018) 8667–8679. doi:10.1021/acs.jpcc.8b01898.
- [22] M. Assis, R.A. Pontes Ribeiro, M.H. Carvalho, M.M. Teixeira, Y.G.

Gobato, G.A. Prando, C.R. Mendonça, L. De Boni, A.J. Aparecido De Oliveira, J. Bettini, J. Andrés, E. Longo, Unconventional Magnetization Generated from Electron Beam and Femtosecond Irradiation on α -Ag₂WO₄: A Quantum Chemical Investigation, *ACS Omega*. 5 (2020) 10052–10067. doi:10.1021/acsomega.0c00542.

[23] E. Longo, W. Avansi, J. Bettini, J. Andrés, L. Gracia, In situ Transmission Electron Microscopy observation of Ag nanocrystal evolution by surfactant free electron-driven synthesis, *Scientific Reports*. 6 (2016) 1–8. doi:10.1038/srep21498.

[24] E. Longo, L.S. Cavalcante, D.P. Volanti, A.F. Gouveia, V.M. Longo, J.A. Varela, M.O. Orlandi, J. Andrés, Direct in situ observation of the electron-driven synthesis of Ag filaments on α -Ag₂WO₄ crystals, *Scientific Reports*. 3 (2013) 4–7. doi:10.1038/srep01676.

[25] J. Andrés, L. Gracia, P. Gonzalez-Navarrete, V.M. Longo, W. Avansi, D.P. Volanti, M.M. Ferrer, P.S. Lemos, F.A. La Porta, A.C. Hernandez, E. Longo, Structural and electronic analysis of the atomic scale nucleation of Ag on α -Ag₂WO₄ induced by electron irradiation, *Scientific Reports*. 4 (2014) 1–7. doi:10.1038/srep05391.

[26] W. da S. Pereira, J. Andrés, L. Gracia, M.A. San-Miguel, E.Z. da Silva, E. Longo, V.M. Longo, Elucidating the real-time Ag nanoparticle growth on α -Ag₂WO₄ during electron beam irradiation: experimental evidence and theoretical insights, *Physical Chemistry Chemical Physics*. 17 (2015) 5352–5359. doi:10.1039/c4cp05849f.

[27] J. Andrés, A.F. Gouveia, L. Gracia, E. Longo, G. Manzeppi Faccin, E.Z. da Silva, D.H. Pereira, M.A. San-Miguel, Formation of Ag nanoparticles under electron beam irradiation: Atomistic origins from first-principles calculations, *International Journal of Quantum Chemistry*. 118 (2018) 1–15. doi:10.1002/qua.25551.

[28] M. Longo, C.C. De Foggi, M.M. Ferrer, A.F. Gouveia, R.S. Andre, W. Avansi, C.E. Vergani, A.L. Machado, J. Andre, A.C. Hernandez, E. Longo, P.O. Box, Potentiated Electron Transference in α - Ag₂WO₄ Microcrystals with Ag Nanofilaments as Microbial Agent. *The Journal of Physical Chemistry A* (2014). doi:10.1021/jp410564p.

[29] M. Assis, E. Cordoncillo, R. Torres-mendieta, H. Beltrán-mir, G. Mínguez-vega, R. Oliveira, E.R. Leite, C.C. Foggi, C.E. Vergani, E. Longo, J. Andrés, Towards the scale-up of the formation of nanoparticles on α - Ag₂WO₄ with bactericidal properties by femtosecond laser irradiation, (2018) 1–11. doi:10.1038/s41598-018-19270-9.

[30] N.G. Macedo, T.R. Machado, R.A. Roca, M. Assis, C.C. Foggi, V. Puerto-Belda, G. Mínguez-Vega, A. Rodrigues, M.A. San-Miguel, E. Cordoncillo, H. Beltrán-Mir, J. Andrés, E. Longo, Tailoring the Bactericidal Activity of Ag Nanoparticles/ α -Ag₂WO₄ Composite Induced by Electron Beam and Femtosecond Laser Irradiation: Integration of Experiment and Computational Modeling, *ACS Applied Bio Materials*. 2 (2019) 824–837. doi:10.1021/acsbm.8b00673.

[31] M. Assis, T. Robeldo, C.C. Foggi, A.M. Kubo, G. Mínguez-Vega, E.

- Condoncillo, H. Beltran-Mir, R. Torres-Mendieta, J. Andrés, M. Oliva, C.E. Vergani, P.A. Barbugli, E.R. Camargo, R.C. Borra, E. Longo, Ag Nanoparticles/ α -Ag₂WO₄ Composite Formed by Electron Beam and Femtosecond Irradiation as Potent Antifungal and Antitumor Agents, *Scientific Reports*. 9 (2019) 1–15. doi:10.1038/s41598-019-46159-y.
- [32] E. Longo, D.P. Volanti, V.M. Longo, L. Gracia, I.C. Nogueira, M.A.P. Almdeira, A.N. Pinheiro, M.M. Ferrer, L.S. Cavalcante, J. Andrés, Toward an understanding of the growth of Ag filaments on α -Ag₂WO₄ and their photoluminescent properties: A combined experimental and theoretical study, *Journal of Physical Chemistry C*. 118 (2014) 1229–1239. doi:10.1021/jp408167v.
- [33] A. Sreedevi, K.P. Priyanka, K.K. Babitha, S. Ganesh, T. Varghese. Influence of electron beam irradiation on structural and optical properties of α -Ag₂WO₄ nanoparticles, *Micron*. 88 (2016) 1–6. doi:10.1016/j.micron.2016.05.003.
- [34] C.C. dos Santos, M. de Assis, T.R. Machado, P.F. dos Santos Pereira, G. Minguez-Vega, E. Cordoncillo, H. Beltran-Mir, C. Doñate-Buendía, J. Andrés, E. Longo, Proof-of-Concept Studies Directed toward the Formation of Metallic Ag Nanostructures from Ag₃PO₄ Induced by Electron Beam and Femtosecond Laser, *Particle and Particle Systems Characterization*. 36 (2019) 1–9. doi:10.1002/ppsc.201800533.
- [35] P.S. Lemos, G.S. Silva, R.A. Roca, M. Assis, R. Torres-Mendieta, H. Beltrán-Mir, G. Minguez-Vega, E. Cordoncillo, J. Andrés, E. Longo, Laser and electron beam-induced formation of Ag/Cr structures on Ag₂CrO₄, *Physical Chemistry Chemical Physics*. 21 (2019) 6101–6111. doi:10.1039/c8cp07263a.
- [36] C.H.B. Ng, W.Y. Fan, Preparation of highly uniform 1-dimensional α -Ag₂WO₄ nanostructures with controllable aspect ratio and study of the growth mechanism, *CrystEngComm*. 18 (2016) 8010–8019. doi:10.1039/c6ce01298a.
- [37] Z. Lin, J. Li, Z. Zheng, J. Yan, P. Liu, C. Wang, G. Yang, Electronic Reconstruction of α -Ag₂WO₄ Nanorods for Visible-Light Photocatalysis, *ACS Nano*. 9 (2015) 7256–7265. doi:10.1021/acsnano.5b02077.
- [38] P.F.S. Pereira, A.F. Gouveia, M. Assis, R.C. De Oliveira, I.M. Pinatti, M. Penha, R.F. Gonçalves, L. Gracia, J. Andrés, E. Longo, ZnWO₄ nanocrystals: Synthesis, morphology, photoluminescence and photocatalytic properties, *Physical Chemistry Chemical Physics*. 20 (2018) 1923–1937. doi:10.1039/c7cp07354b.
- [39] I.M. Pinatti, I.C. Nogueira, W.S. Pereira, P.F.S. Pereira, R.F. Gonçalves, J.A. Varela, E. Longo, I.L.V. Rosa, Structural and photoluminescence properties of Eu³⁺ doped α -Ag₂WO₄ synthesized by the green coprecipitation methodology, *Dalton Transactions*. 44 (2015) 17673–17685. doi:10.1039/c5dt01997d.
- [40] C.C. de Foggi, R.C. de Oliveira, M.T. Fabbro, C.E. Vergani, J. Andres, E. Longo, A.L. Machado, Tuning the Morphological, Optical, and Antimicrobial Properties of α -Ag₂WO₄ Microcrystals Using Different

Solvents, *Crystal Growth & Design*. 17 (2017) 6239–6246.
doi:10.1021/acs.cgd.7b00786.

[41] A.C.M. Tello, M. Assis, R. Menasce, A.F. Gouveia, V. Teodoro, N. Jacomaci, M.A. Zaghete, J. Andrés, G.E. Marques, M.D. Teodoro, A.B.F. Da Silva, E. Longo, Microwave-Driven Hexagonal-to-Monoclinic Transition in BiPO₄: An In-Depth Experimental Investigation and First-Principles Study, *Inorganic Chemistry*. 59 (2020) 7453–7468.
doi:10.1021/acs.inorgchem.0c00181.

[42] R. Dovesi, A. Erba, R. Orlando, C.M. Zicovich-Wilson, B. Civalleri, L. Maschio, M. Rérat, S. Casassa, J. Baima, S. Salustro, B. Kirtman, Quantum-mechanical condensed matter simulations with CRYSTAL, *Wiley Interdisciplinary Reviews: Computational Molecular Science*. 8 (2018) 1–36.
doi:10.1002/wcms.1360.

[43] A. D. Becke, A new mixing of Hartree–Fock and local density-functional theories, *The Journal of Chemical Physics*, 98(2) (1993) 1372–1377. doi:10.1063/1.464304

[44] E. Aprà, E. Stefanovich, R. Dovesi, C. Roetti, An ab initio Hartree-Fock study of silver chloride, *Chemical Physics Letters*. 186 (1991) 329–335.
doi:10.1016/0009-2614(91)90187-E.

[45] F. Corà, A. Patel, N.M. Harrison, R. Dovesi, C.R.A. Callow, An ab initio Hartree-Fock study of the cubic and tetragonal phases of bulk tungsten trioxide, *Journal of the American Chemical Society*. 118 (1996) 12174–12182. doi:10.1021/ja961514u.

[46] L. Valenzano, F.J. Torres, K. Doll, F. Pascale, C.M. Zicovich-Wilson, R. Dovesi, Ab initio study of the vibrational spectrum and related properties of crystalline compounds; the case of CaCO₃ calcite, *Zeitschrift Fur Physikalische Chemie*. 220 (2006) 893–912.
doi:10.1524/zpch.2006.220.7.893.

[47] K. Momma, F. Izumi, VESTA: A three-dimensional visualization system for electronic and structural analysis, *Journal of Applied Crystallography*. 41 (2008) 653–658. doi:10.1107/S0021889808012016.

[48] R.A. Roca, J.C. Sczancoski, I.C. Nogueira, M.T. Fabbro, H.C. Alves, L. Gracia, L.P.S. Santos, C.P. de Sousa, J. Andrés, G.E. Luz, E. Longo, L.S. Cavalcante, Facet-dependent photocatalytic and antibacterial properties of α -Ag₂WO₄ crystals: combining experimental data and theoretical insights, *Catal. Sci. Technol.* 5 (2015) 4091–4107. doi:10.1039/C5CY00331H.

[49] R.F. Egerton, P. Li, M. Malac, Radiation damage in the TEM and SEM, *Micron*. 35 (2004) 399–409. doi:10.1016/j.micron.2004.02.003.

[50] M. Assis, N.G. Macedo, T.R. Machado, M.M. Ferrer, A.F. Gouveia, E. Cordoncillo, R. Torres-Mendieta, H. Beltrán-Mir, G. Mínguez-Vega, E.R. Leite, J.R. Sambrano, J. Andrés, E. Longo, Laser/Electron Irradiation on Indium Phosphide (InP) Semiconductor: Promising Pathways to In Situ Formation of Indium Nanoparticles, *Particle and Particle Systems Characterization*. 35 (2018) 1–10. doi:10.1002/ppsc.201800237.

[51] R.O. Torres-Mendieta, M.M. Teixeira, G. Mínguez-Vega, D. De Souza, Y.G. Gobato, M. Assis, H. Beltrán-Mir, E. Cordoncillo, J. Andrés, M. Černík,

- E. Longo, Toward Expanding the Optical Response of Ag₂CrO₄ and Bi₂O₃ by Their Laser-Mediated Heterojunction, *Journal of Physical Chemistry C*. 124 (2020) 26404–26414. doi:10.1021/acs.jpcc.0c08301.
- [52] V.N. Rai, S.N. Thakur, *Physics and dynamics of plasma in laser-induced breakdown spectroscopy*, 2nd ed., Elsevier B.V., 2020. doi:10.1016/b978-0-12-818829-3.00004-6.
- [53] P.M. Skarstad, S. Geller, (W4016)8- polyion in the high temperature modification of silver tungstate, *Mat.Res.Bull.* 10(8), (1975) 791–799. doi:10.1016/0025-5408(75)90193-2.
- [54] L. Yang, J. Wang, Y. Wan, Y. Li, H. Xie, H. Cheng, H.J. Seo, Structure and effective visible-light-driven photocatalytic activity of α -NiMoO₄ for degradation of methylene blue dye, *Journal of Alloys and Compounds*. 664 (2016) 756–763. doi:10.1016/j.jallcom.2015.10.037.
- [55] W. Zhu, X. Feng, Z. Wu, Z. Man, On the annealing mechanism in PbWO₄ crystals, *Physica B: Condensed Matter*. 324 (2002) 53–58. doi:10.1016/S0921-4526(02)01269-3.
- [56] O. Dulub, U. Diebold, G. Kresse, Novel Stabilization Mechanism on Polar Surfaces: ZnO(0001)-Zn, *Physical Review Letters*. 90 (2003) 4. doi:10.1103/PhysRevLett.90.016102.
- [57] A. Barbier, G. Renaud, A. Stierle, The NiO (111)-(1×1) surface, *Surface Science*. 402–404 (1998) 757–760. doi:10.1016/S0039-6028(97)01020-0.
- [58] C. Ren, R. Yang, Y. Li, H. Wang, Modulating of facets-dependent oxygen vacancies on ceria and its catalytic oxidation performance, *Research on Chemical Intermediates*. 45 (2019) 3019–3032. doi:10.1007/s11164-019-03776-6.
- [59] H. He, S. Xue, Z. Wu, C. Yu, K. Yang, G. Peng, W. Zhou, D. Li, Sonochemical fabrication, characterization and enhanced photocatalytic performance of Ag₂S/Ag₂WO₄ composite microrods, *Cuihua Xuebao/Chinese Journal of Catalysis*. 37 (2016) 1841–1850. doi:10.1016/S1872-2067(16)62515-9.
- [60] F.Y. Xie, L. Gong, X. Liu, Y.T. Tao, W.H. Zhang, S.H. Chen, H. Meng, J. Chen, XPS studies on surface reduction of tungsten oxide nanowire film by Ar + bombardment, *Journal of Electron Spectroscopy and Related Phenomena*. 185 (2012) 112–118. doi:10.1016/j.elspec.2012.01.004.
- [61] A. Turkovič, D.L. Fox, J.F. Scott, S. Geller, G.F. Ruse, High temperature Raman spectroscopy of silver tetratungstate, Ag₈W₄O₁₆, *Materials Research Bulletin*. 12 (1977) 189–195. doi:10.1016/0025-5408(77)90163-5.
- [62] S.K. Gupta, K. Sudarshan, P.S. Ghosh, S. Mukherjee, R.M. Kadam, Doping-Induced Room Temperature Stabilization of Metastable β -Ag₂WO₄ and Origin of Visible Emission in α - And β -Ag₂WO₄: Low Temperature Photoluminescence Studies, *Journal of Physical Chemistry C*. 120 (2016) 7265–7276. doi:10.1021/acs.jpcc.6b00078.
- [63] I.M. Pinatti, G.R. Fern, E. Longo, T.G. Ireland, P.F.S. Pereira, I.L.V. Rosa, J. Silver, Luminescence properties of α -Ag₂WO₄ nanorods co-doped

- with Li⁺ and Eu³⁺ cations and their effects on its structure, *Journal of Luminescence*. 206 (2018) 442–454. doi:10.1016/j.jlumin.2018.10.104.
- [64] A.C. Catto, T. Florido, É.L.S. Souza, W. Avansi, J. Andres, K. Aguir, E. Longo, L.S. Cavalcante, L.F. da Silva, Improving the ozone gas-sensing properties of CuWO₄ nanoparticles, *Journal of Alloys and Compounds*. 748 (2018) 411–417. doi:10.1016/j.jallcom.2018.03.104.
- [65] A.C. Catto, L.F.D. Silva, M.I.B. Bernardi, S. Bernardini, K. Aguir, E. Longo, V.R. Mastelaro, Local Structure and Surface Properties of Co_xZn_{1-x}O Thin Films for Ozone Gas Sensing, *ACS Applied Materials and Interfaces*. 8 (2016) 26066–26072. doi:10.1021/acsami.6b08589.
- [66] L.S. Cavalcante, M.A.P. Almeida, W. Avansi, R.L. Tranquilin, E. Longo, N.C. Batista, V.R. Mastelaro, M.S. Li, Cluster coordination and photoluminescence properties of α-Ag₂WO₄ microcrystals, *Inorganic Chemistry*. 51 (2012) 10675–10687. doi:10.1021/ic300948n.
- [67] M.M. Teixeira, Y.G. Gobato, L. Gracia, L.F. da Silva, W. Avansi, M. Assis, R.C. de Oliveira, G.A. Prando, J. Andrés, E. Longo, Towards a white-emitting phosphor Ca₁₀V₆O₂₅ based material, *Journal of Luminescence*. 220 (2020) 116990. doi:10.1016/j.jlumin.2019.116990.
- [68] L.F. Da Silva, A.C. Catto, W. Avansi, A. Mesquita, L.J.Q. Maia, O.F. Lopes, M.S. Li, M.L. Moreira, E. Longo, J. Andrés, V.R. Mastelaro, Unveiling the efficiency of microwave-assisted hydrothermal treatment for the preparation of SrTiO₃ mesocrystals, *Physical Chemistry Chemical Physics*. 21 (2019) 22031–22038. doi:10.1039/c9cp02893e.
- [69] S. Yamazoe, Y. Hitomi, T. Shishido, T. Tanaka, XAFS study of tungsten L₁- And L₃-edges: structural analysis of WO₃ species loaded on TiO₂ as a catalyst for photo-oxidation of NH₃, *Journal of Physical Chemistry C*. 112 (2008) 6869–6879. doi:10.1021/jp711250f.
- [70] G. Poirier, F.C. Cassanjes, Y. Messaddeq, S.J.L. Ribeiro, A. Michalowicz, M. Poulain, Local order around tungsten atoms in tungstate fluorophosphate glasses by X-ray absorption spectroscopy, *Journal of Non-Crystalline Solids*. 351 (2005) 3644–3648. doi:10.1016/j.jnoncrysol.2005.08.038.
- [71] D. Wood, J. Tauc, Weak Absorption Tails in Amorphous Semiconductors, 5(8) *Physical Review B* (1972), 3144–3151. doi:10.1103/physrevb.5.3144.
- [72] B. Philips-Invernizzi, Bibliographical review for reflectance of diffusing media, *Optical Engineering*. 40 (2001) 1082. doi:10.1117/1.1370387.
- [73] L. Yang, B. Kruse, Revised Kubelka–Munk theory I Theory and application, *Journal of the Optical Society of America A*. 21 (2004) 1933. doi:10.1364/josaa.21.001933.
- [74] A. Sreedevi, K.P. Priyanka, K.K. Babitha, N. Aloysius Sabu, T.S. Anu, T. Varghese, Chemical synthesis, structural characterization and optical properties of nanophase α- Ag₂WO₄. *Indian Journal of Physics*. 89 (2015) 889–897. doi:10.1007/s12648-015-0664-1.
- [75] M. Li, T. Takei, Q. Zhu, B. Kim, J. Li, Morphology Tailoring of ZnWO₄

Crystallites / Architectures and Photoluminescence of the Doped RE 3+ Ions (RE = Sm , Eu , Tb , and Dy), *Inorganic Chemistry*. 58 (2019) 9432–9442. doi:10.1021/acs.inorgchem.9b01271.

[76] R. Alvarez-Roca, A.F. Gouveia, C.C. De Foggi, P.S. Lemos, L. Gracia, L.F. Da Silva, C.E. Vergani, M. San-Miguel, E. Longo, J. Andrés, Selective Synthesis of α -, β -, and γ -Ag₂WO₄ Polymorphs: Promising Platforms for Photocatalytic and Antibacterial Materials, *Inorganic Chemistry*. 60 (2021) 1062–1079. doi:10.1021/acs.inorgchem.0c03186.

[77] A. Sreedevi, K.P. Priyanka, K.K. Babitha, S.I. Sankararaman, V. Thomas, Synthesis and characterization of silver tungstate/iron phthalocyanine nanocomposite for electronic applications, *European Physical Journal B*. 90 (2017) 1–10. doi:10.1140/epjb/e2017-80149-9.

Capítulo 4

Conclusions

The use of ethylenediamine complexing agent and irradiation (electron beam and femtosecond laser) were effective in altering the photoluminescent property of α -Ag₂WO₄. This change is closely related to the formation of silver nanoparticles on the surface of α -Ag₂WO₄, which caused: structural disorders, morphological variation (cubes, rods, spheres, multidimensional structures) and alteration in oxygen vacancies (increase or decrease). Through these works, it was possible to elucidate the mechanism of particle growth. Two processes occur when employing En: Ostwald ripening (particle growth) and self-assembly (particle organization). Depending on En concentration, there is formation of α -Ag₂WO₄ nanorods or microrods, organized in hollow or solid microflowers. En acts as a complexing agent and thus controls nucleation rate, guides growth and acts as a reducing agent of silver ion. Theoretical calculations show that the surface band gap values alter the distribution of electronic density and thus, the emission centers. While the use of En shifted the emission center from red to blue due to structural disorder, irradiation altered the contribution of the surfaces and thus, there is a relationship between the surfaces and emission centers.

Apêndice A

Supplementary Information for "Multi-Dimensional Architecture of Ag/ α -Ag₂WO₄ Crystals: Insights into Microstructural, Morphology, and Photoluminescent Properties"

SUPPORTING INFORMATION

A.1 - Characterizations

Figure A.1 shows the results by the Rietveld method and **Table A.1** corroborates the statistical parameters that guarantee the quality of the refinement (GOF, R_{Bragg} , R_{exp} , R_{wp}), which have few deviations, suggesting that the refinement of the structure and the numerical results are reliable.

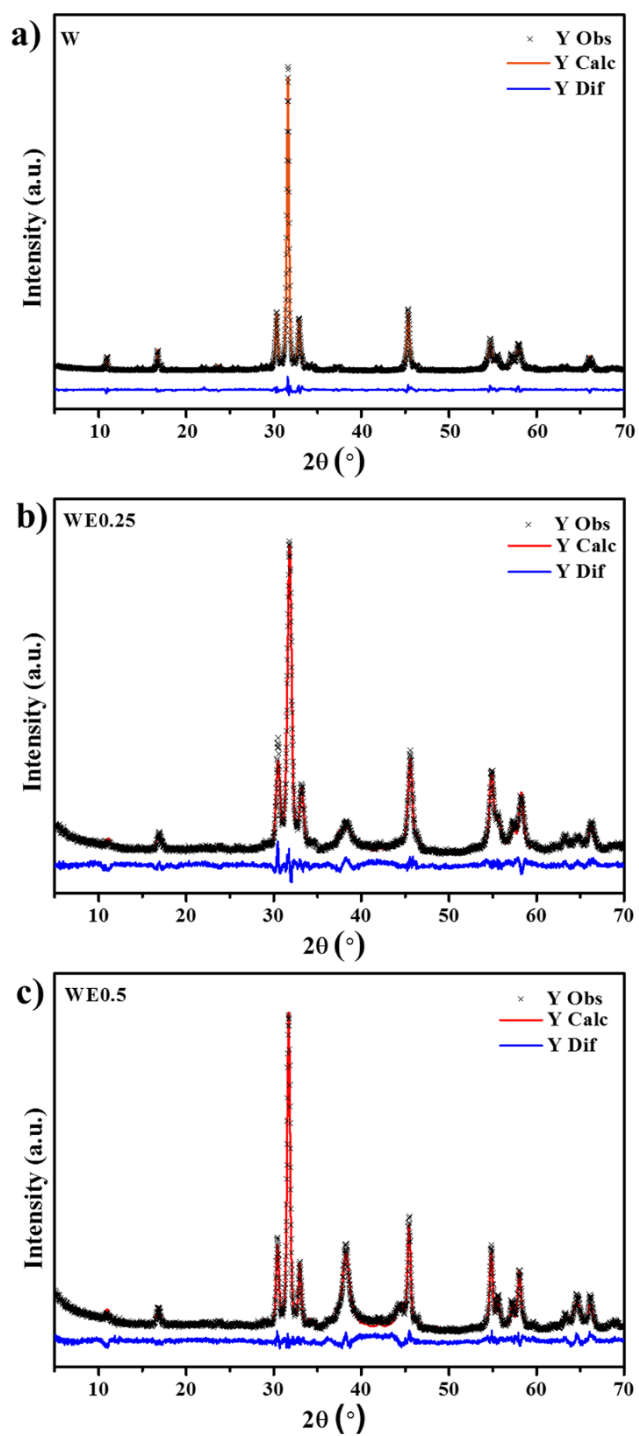


Figure A.2 Rietveld refinement plot of α - Ag_2WO_4 samples prepared by the MAH method: a) W, b) WE0.25 and c) WE0.5.

Table A.1 Statistical parameters obtained by Rietveld refinement of the Ag/ α -Ag₂WO₄ samples.

Samples	α -Ag ₂ WO ₄				Ag ⁰
	GOF	R _{BRAGG}	R _{EXP}	R _{WP}	R _{BRAGG}
W	2.13	2.22	3.44	7.34	*
WE0.25	1.66	2.18	4.83	7.99	1.29
WE0.5	1.81	3.05	4.86	8.80	1.10

Deviations at the binding angle of the O-Ag-O and O-W-O can be confirmed in **Tables A.2** and **A.3**.

Table A.2 Bond angles of [AgO_y] (Card ICSD n^o. 4165)^{1, 2, 3}.

	Ref	W	WE0.25	WE0.5	Ref-W	Ref-WE0.25	Ref-WE0.5
O6Ag3O6	174.6	174.6	174.6	174.6	0.02	0.01	0.01
O6Ag3O2	67.6	67.8	67.7	67.9	0.20	0.09	0.26
O6Ag3O2	115.2	115.1	115.2	115.0	0.12	0.01	0.18
O6Ag3O1	66.1	66.3	66.1	66.3	0.16	0.04	0.21
O6Ag3O1	110.7	110.6	110.7	110.5	0.12	0.02	0.18
O1Ag3O2	62.4	62.4	62.5	62.5	0.06	0.17	0.10
O2Ag3O2	121.4	121.3	121.2	121.3	0.06	0.17	0.11
O1Ag3O1	113.9	113.9	113.7	113.8	0.05	0.16	0.09
O4Ag4O7	94.7	94.6	94.7	94.6	0.13	0.01	0.16
O4Ag4O4	110.7	110.6	110.5	110.5	0.13	0.22	0.19
O4Ag4O7	99.5	99.6	99.5	99.6	0.10	0.03	0.15
O7Ag4O7	154.9	155.0	154.9	155.0	0.07	0.02	0.06

O3Ag508	89.9	89.8	89.9	89.8	0.12	0.02	0.15
O3Ag508	106.4	106.6	106.5	106.6	0.13	0.07	0.18
O3Ag503	130.1	130.0	129.9	130.0	0.09	0.16	0.14
O8Ag508	141.0	141.1	140.9	141.1	0.08	0.06	0.07
O5Ag605	170.4	170.4	170.4	170.4	0.04	0.01	0.03
O1Ag102	139.0	139.0	139.0	139.0	0.04	0.00	0.04
O1Ag103	104.4	104.2	104.3	104.1	0.23	0.06	0.29
O1Ag104	97.3	97.5	97.4	97.6	0.22	0.11	0.28
O1Ag105	63.8	64.0	63.8	64.0	0.15	0.03	0.18
O1Ag107	141.0	141.0	140.9	140.9	0.04	0.08	0.07
O1Ag108	87.7	87.8	87.9	87.8	0.08	0.15	0.10
O1Ag202	140.6	140.6	140.6	140.6	0.13	0.02	0.02
O1Ag203	57.9	57.8	57.9	57.8	0.07	0.02	0.11
O1Ag204	83.0	83.1	82.9	83.1	0.08	0.07	0.10
O1Ag205	127.1	127.1	127.2	127.0	0.05	0.12	0.06
O1Ag207	57.7	57.6	57.5	57.6	0.08	0.20	0.12
O1Ag208	76.3	76.4	76.4	76.4	0.05	0.13	0.09

Table A.3 Bond angles of [WO₆] (Card ICSD n^o. 4165)^{1, 2, 3}.

	Ref	W	WE0.25	WE0.5	Ref- W	Ref- WE0.25	Ref- WE0.5
O8W107	106.2	106.2	106.3	106.3	0.01	0.10	0.04
O8W105	99.3	99.1	99.2	99.1	0.18	0.12	0.23
O8W102	80.1	80.1	79.9	80.1	0.03	0.18	0.07
O8W106	93.1	93.3	93.2	93.3	0.13	0.03	0.16
O8W101	159.3	159.3	159.4	159.3	0.02	0.01	0.02
O7W105	109.2	109.1	109.17	109.0	0.14	0.06	0.19
O5W102	84.8	85.0	84.9	85.0	0.15	0.03	0.19
O2W106	71.4	71.2	71.4	71.2	0.19	0.06	0.23
O6W107	92.2	92.3	92.3	92.4	0.12	0.02	0.16
O1W107	90.2	90.1	90.0	90.07	0.04	0.18	0.09
O1W105	86.8	87.0	86.9	87.0	0.16	0.05	0.21
O1W102	80.8	80.8	81.0	80.8	0.02	0.15	0.01
O1W106	73.2	73.1	73.2	73.0	0.15	0.00	0.19
O6W204	158.8	158.8	158.8	158.8	0.02	0.01	0.02
O6W204	89.1	89.1	89.2	89.2	0.06	0.18	0.10
O6W202	76.0	75.8	75.9	75.8	0.14	0.06	0.18
O6W206	72.2	72.2	72.0	72.1	0.04	0.18	0.07
O6W202	85.6	85.7	85.5	85.7	0.12	0.02	0.15
O2W204	99.9	99.7	99.8	99.6	0.17	0.013	0.22
O4W202	93.0	93.2	93.1	93.3	0.18	0.08	0.24
O4W204	111.0	110.9	110.8	110.8	0.08	0.19	0.13
O3W306	166.1	166.1	166.1	166.2	0.01	0.00	0.01
O3W301	96.2	96.4	96.1	96.4	0.14	0.17	0.20

O3W3O3	100.7	100.6	100.4	100.5	0.08	0.21	0.13
O3W3O1	96.1	95.9	96.3	96.0	0.22	0.13	0.27
O3W3O6	92.6	92.6	92.7	92.6	0.04	0.18	0.09
O6W3O1	86.7	86.8	86.7	86.8	0.06	0.08	0.10
O1W3O6	78.0	77.9	78.0	77.8	0.16	0.08	0.21
O6W3O6	74.7	74.6	74.5	74.6	0.11	0.25	0.14

All vibrational modes (Raman) of the samples and reference are shown in **Table A.4**.

Table A.4 Peak locations relative to the α -Ag₂WO₄ micro-Raman spectroscopy analysis.

	W	WE0.25	WE0.5	Ref
A_{1g}				44
A_{1g}				60
B_{1g}	104	104	104	92
A_{2g}				116
A_{2g}				182
A_{1g}		206		208
B_{1g}				248
A_{2g}	308	308	308	306
B_{2g}	331	331	331	336
A_{2g}	380	380	380	366
B_{2g}				488
B_{2g}	500	500		510
B_{2g}				546
A_{1g}	575	575		590
B_{1g}				629
B_{1g}	660	660	660	667

B_{1g}			723	730
B_{2g}	731	731	731	754
A_{1g}	770	771		778
A_{2g}				800
WO₄²⁻ (v₃)			828	832*
A_{1g}	877	877	877	884
WO₄²⁻ (v₁)			949	922*

References*2, 4, *5

The literature shows that for different synthetic routes, without using surfactants or complexing agents, the α -Ag₂WO₄ shows a preferential formation of the eight-faceted hexagonal base rod-like morphology, which is composed by the (101), (010), and (001) surfaces, which are similar to those obtained by Cavalcante et al.⁶ by the SC, CP, and CH methods, with only small modifications in the rod lengths. **Figure A.2** presents the TEM images of the particles obtained by the MAH method. **Figure A.2 (a-b)** show the microrods of the W sample. It can be observed that this sample displays (**Figure A.2 (a)**) only some NPs on this surface, especially at the rods; however, this amount increases with the electron beam, as shown in **Figure A.2 (b)**. Although it is possible to have some NPs before the exposure to the electron microscope, they are mainly caused by the being exposed to the high-energy electron beam, as shown in **Figure. A.2 (b)**. A few seconds after the beam in the TEM, it is possible to observe several filaments of metallic Ag, as reported by Longo et al.⁷⁻¹². In **Figure A.2 (c-d)**, which refers to the WE0.25 sample, note the hollow structures consisting of nanorods and NPs. In this case, the NPs were already formed before the TEM analysis and they changed minimally with the increase in electron beam exposure time, as can be observed from the pictures in **Figure A.2 (c-d)**. Finally, note the flower-like structures consisting of microrods and NPs in the WE0.5 sample shown in **Figure A.2 (e-f)**. This sample was very unstable under the electron beam irradiation and the NPs on

the surface started to grow, forming filaments by sintering and making the visualization of the planes of the NPs in the high-resolution TEM analysis difficult because the particles are constantly growing, as shown in **Figure A.3 (a-b)**. The differences of growth, shape, and stability are due to the morphologic aspects, as the NPs growth is a surface dependent property, as shown by Macedo et al.¹³, comparing the differences of preferential Ag growth on two morphologies of α -Ag₂WO₄.

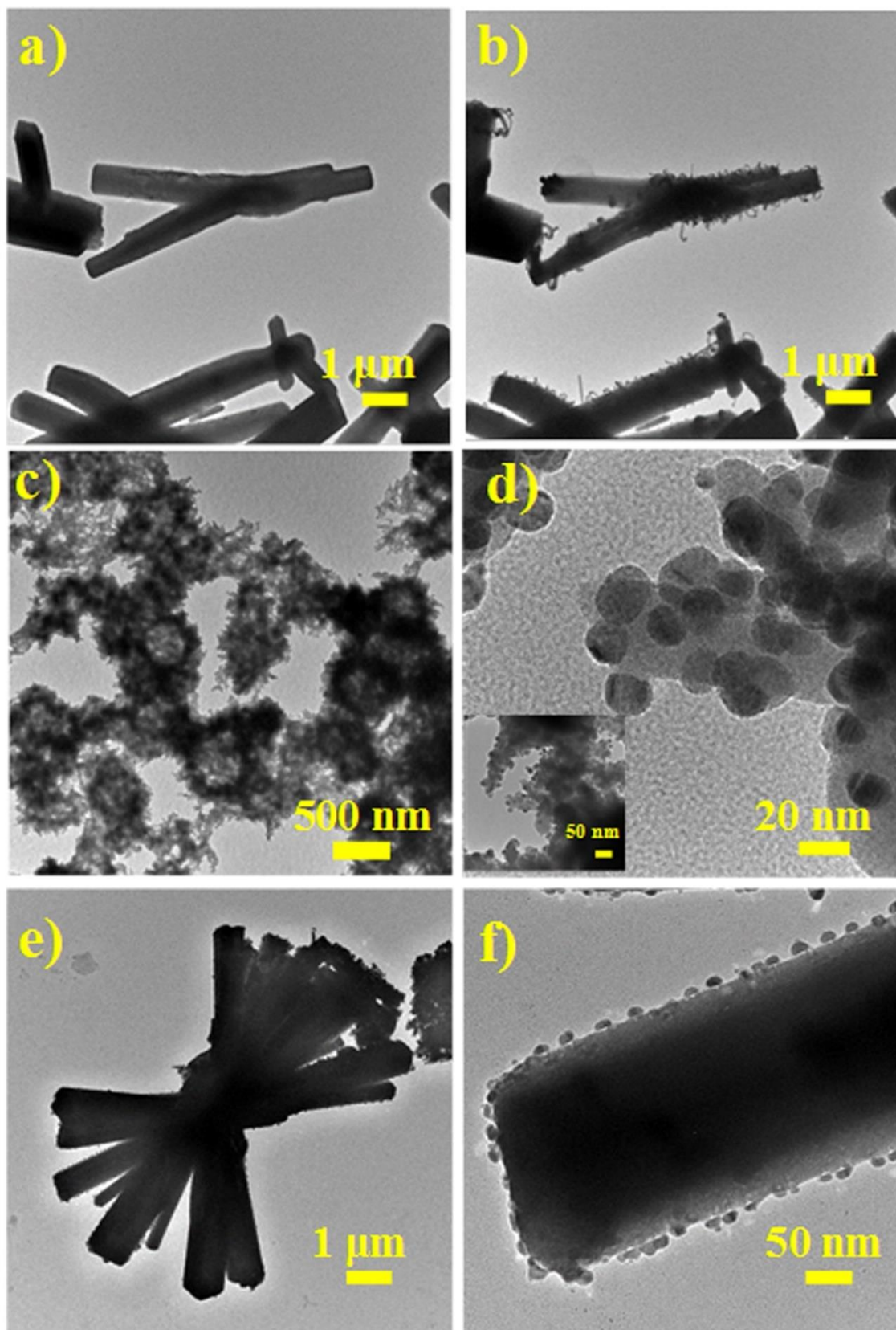


Figure A.2 TEM images of samples exposed to a 200 kV electron beam. a, b) W; c, d) WE0.25 and e, f) WE0.5.

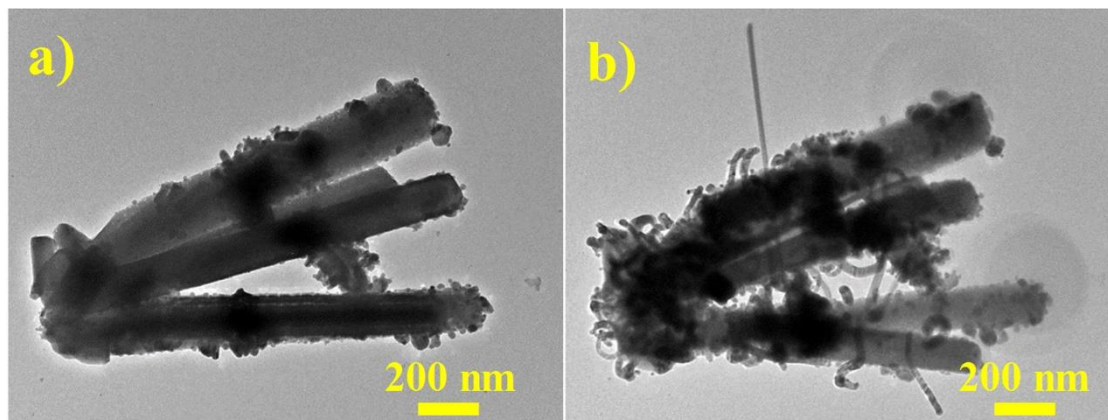


Figure A.3 Low-resolution TEM analysis of the WE0.5 sample of the α - Ag_2WO_4 and Ag NPs at a) at time zero and b) 10 seconds later.

A.2 - REFERENCES

- (1) Skarstad, P. M.; Geller, S. (W_4O_{16}) 8- Polyion in the High Temperature Modification of Silver Tungstate. *Mat. Res. Bull* **1975**, *10*, 791–799.
- (2) Stone, D.; Liu, J.; Singh, D. P.; Muratore, C.; Voevodin, A. A.; Mishra, S.; Rebholz, C.; Ge, Q.; Aouadi, S. M. Layered Atomic Structures of Double Oxides for Low Shear Strength at High Temperatures. *Scr. Mater.* **2010**, *62* (10), 735–738.
- (3) Silva, M. D. P.; Gonçalves, R. F.; Nogueira, I. C.; Longo, V. M.; Mondoni, L.; Moron, M. G.; Santana, Y. V; Longo, E. Microwave-Assisted Hydrothermal Synthesis of $\text{Ag}_2(\text{W}_{1-x}\text{Mo}_x)\text{O}_4$ Heterostructures: Nucleation of Ag, Morphology, and Photoluminescence Properties. *Spectrochim. Acta Part A Mol. Biomol. Spectrosc.* **2016**, *153*, 428–435.
- (4) Turkovic, A.; Fox, L.; Scott, J. F.; Geller, S.; Ruse, G. F. High Temperature Raman Spectroscopy of Silver Tetratungstate, $\text{Ag}_8\text{W}_4\text{O}_{16}$. *Mat. Res. Bull* **1977**, *12*, 189–196.

- (5) Feilchenfeld, H.; Siiman, O. Adsorption and Aggregation Kinetics and Its Fractal Description for Chromate, Molybdate, and Tungstate Ions on Colloidal Silver from Surface Raman Spectra. *J. Phys. Chem.* **1986**, *90* (19), 4590–4599.
- (6) Cavalcante, L. S.; Almeida, M. A. P.; Avansi, W.; Tranquilin, R. L.; Longo, E.; Batista, N. C.; Mastelaro, V. R.; Li, M. S. Cluster Coordination and Photoluminescence Properties of α -Ag₂WO₄ Microcrystals. *Inorg. Chem.* **2012**, *51* (20), 10675–10687.
- (7) Da Silva, L. F.; Catto, A. C.; Avansi, W.; Mesquita, A.; Maia, L. J. Q.; Lopes, O. F.; Li, M. S.; Moreira, M. L.; Longo, E.; Andrés, J.; Mastelaro, V. R. Unveiling the Efficiency of Microwave-Assisted Hydrothermal Treatment for the Preparation of SrTiO₃ Mesocrystals. *Phys. Chem. Chem. Phys.* **2019**, *21* (39), 22031–22038.
- (8) Pereira, W. da S.; Andrés, J.; Gracia, L.; San-Miguel, M. A.; da Silva, E. Z.; Longo, E.; Longo, V. M. Elucidating the Real-Time Ag Nanoparticle Growth on α -Ag₂WO₄ during Electron Beam Irradiation: Experimental Evidence and Theoretical Insights. *Phys. Chem. Chem. Phys.* **2015**, *17* (7), 5352–5359.
- (9) Longo, E.; Cavalcante, L. S.; Volanti, D. P.; Gouveia, A. F.; Longo, V. M.; Varela, J. A.; Orlandi, M. O.; Andrés, J. Direct in Situ Observation of the Electron-Driven Synthesis of Ag Filaments on α -Ag₂WO₄ Crystals. *Sci. Rep.* **2013**, *3*, 4–7.
- (10) Longo, E.; Avansi, W.; Bettini, J.; Andrés, J.; Gracia, L. In Situ Transmission Electron Microscopy Observation of Ag Nanocrystal Evolution by Surfactant Free Electron-Driven Synthesis. *Sci. Rep.* **2016**, *6* (January), 1–8.

(11) Longo, E.; Volanti, D. P.; Longo, V. M.; Gracia, L.; Nogueira, I. C.; Almeida, M. A. P.; Pinheiro, A. N.; Ferrer, M. M.; Cavalcante, L. S.; Andrés, J. Toward an Understanding of the Growth of Ag Filaments on α -Ag₂WO₄ and Their Photoluminescent Properties: A Combined Experimental and Theoretical Study. *J. Phys. Chem. C* **2014**, *118* (2), 1229–1239.

(12) Longo, V. M.; De Foggi, C. C.; Ferrer, M. M.; Gouveia, A. F.; André, R. S.; Avansi, W.; Vergani, C. E.; Machado, A. L.; Andrés, J.; Cavalcante, L. S.; Hernandez, A. C.; Longo E. Potentiated Electron Transference in α -Ag₂WO₄ Microcrystals with Ag Nanofilaments as Microbial Agent. *J. Phys. Chem. A* **2014**, *118* (31), 5769–5778.

(13) Macedo, N. G.; Machado, T. R.; Roca, R. A.; Assis, M.; Foggi, C. C.; Puerto-Belda, V.; Mínguez-Vega, G.; Rodrigues, A.; San-Miguel, M. A.; Cordoncillo, E.; Beltrán-Mir, H.; Andrés, J.; Longo, E. Tailoring the Bactericidal Activity of Ag Nanoparticles/ α -Ag₂WO₄ Composite Induced by Electron Beam and Femtosecond Laser Irradiation: Integration of Experiment and Computational Modeling. *ACS Appl. Bio Mater.* **2019**, *2* (2), 824–837.

Apêndice B

Supplementary Information for “ α -Ag₂WO₄ under microwave, electron beam and femtosecond laser irradiation: Unveiling the relationship between morphology and photoluminescence emissions”

SUPPORT INFORMATION

B.1 - Characterizations

The samples obtained in this study were characterized by X-ray diffraction (XRD) using a Rigaku (DMax 2500PC, Japan) diffractometer operating with Cu-K α radiation in 2θ range of 10° to 70° with a scanning speed of $2^\circ/\text{min}$. Surface properties were investigated using X-ray photoelectron spectroscopy (XPS), performed in a Scienta Omicron ESCA spectrometer, Germany, with monochromatic Al K α (1486.7 eV). The calibration was made by C 1s peak at 284.8 eV. Morphological characteristics were investigated using a field emission scanning electron microscope (FE-SEM, Carl Zeiss, Supra 35) operated at an accelerating voltage of 10 kV in different magnifications. The energy-dispersive X-ray spectroscopy (EDS) mapping was made in a Philip XL-30 FEG. Room temperature Raman spectroscopy was carried out using an iHR550 spectrometer Horiba Jobin Yvon coupled to a Silicon Charged Coupled Device (CCD) detector and an argon-ion laser (Melles Griot) operating at 514.5 nm with a maximum power of 200 mW and a fiber-based microscope. The electronic and local atomic structures around the W atoms were probed using X-ray absorption near-edge structure (XANES) spectroscopy. The W-L1 edge XANES spectra of the samples were collected at

the XAFS2 beamline at the Brazilian Synchrotron Light Laboratory (LNLS, project XAFS2-20180338). Room-temperature XANES measurements were performed at the W-L1 edge in a transmission mode. The spectra were recorded using energy steps of 1.0 eV before and after the edge, and 0.7 and 0.9 eV near the edge-region for the L1 edge. For the spectra analysis, their background was removed, and then normalized using as the unit of measurement the first EXAFS oscillation, using MAX software [1]. Ultraviolet-visible (UV-Vis) diffuse reflectance measurements were obtained using a Cary 5G spectrophotometer (Varian, USA) in diffuse reflection mode. Room temperature photoluminescence measurements were performed using a laser (Cobol/Zouk, $\lambda_{\text{exc}} = 355 \text{ nm}$) focused on a $200 \mu\text{m}$ spot with a constant power of 5 mW. The signal was dispersed by a 19.3 cm spectrometer (Andor Kymera) and detected by a Silicon CCD (Andor/Idus BU2).

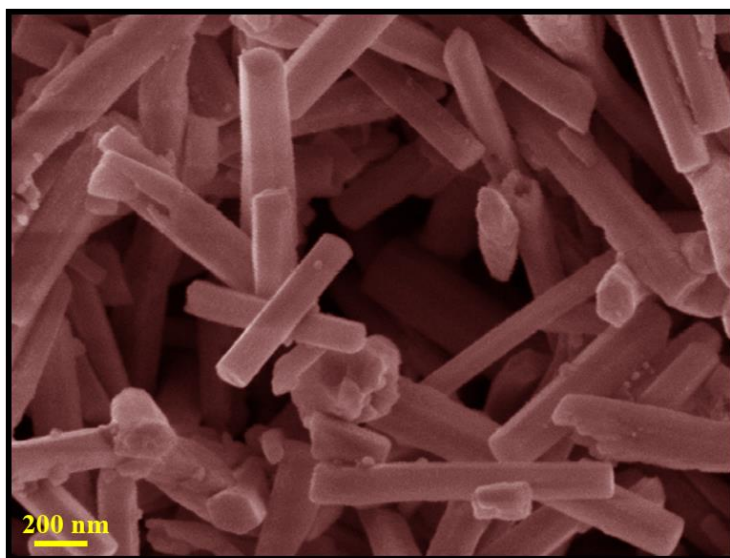





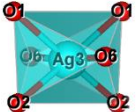
Figure B.1 Micrograph of the CP sample obtained by the CP method.

Table B.1 Rietveld refinement and unit cell parameters of CP, MAH, EI, and FI samples.^[a]


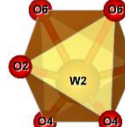
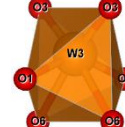
Sample	Cell			Volume (Å ³)	W _{Rp}	R _p	χ^2	R _{Bragg}
	a	b	c					
Theo.	11.127	12.335	5.825		-	-	-	-
CP	10.87645	12.0247	5.90091	771.758	0.0648	0.0509	3.723	0.0351
MAH-2	10.87257	12.00221	5.89195	768.8692	0.0647	0.0497	4.054	0.0394
EI-2	10.88660	12.01960	5.90150	772.2265	0.0867	0.0657	5.101	0.0568
FI-2	10.91010	12.05520	5.91090	777.4219	0.1708	0.1292	3.351	0.0908
MAH-4	10.87492	12.01987	5.89764	770.9108	0.0695	0.0538	4.562	0.0716
EI-4	10.89800	12.04050	5.90826	775.2663	0.0774	0.0601	4.254	0.0558
FI-4	10.9028	12.0594	5.90927	776.96(4)	0.0756	0.0572	3.604	0.0776
MAH-8	10.90134	12.03280	5.90697	774.8387	0.0667	0.0507	4.306	0.0352
EI-8	10.88685	12.01740	5.89973	771.8713	0.0710	0.0554	3.614	0.0595
FI-8	10.90090	12.05140	5.90610	775.8909	0.1549	0.1181	2.331	0.0798
MAH-16	10.89358	12.03580	5.90384	774.0699	0.0703	0.0536	4.600	0.0885
EI-16	10.89190	12.04020	5.90568	774.4748	0.0758	0.0577	4.191	0.0487
FI-16	10.90277	12.05749	5.90632	776.4451	0.1068	0.0790	1.172	0.0469
MAH-32	10.88152	12.01763	5.89648	771.0832	0.0624	0.0488	3.669	0.0334
EI-32	10.88728	12.01700	5.89847	771.7113	0.0690	0.0536	2.974	0.0483
FI-32	10.89470	12.02850	5.90384	773.6799	0.0850	0.0603	4.569	0.0573

^[a]Bond angle: $\alpha = \beta = \gamma = 90^\circ$

Table B.2 Ag–O bond distances (Å) on the [Ag(6)O₂], [Ag(4)O₄], [Ag(5)O₄], [Ag(3)O₆], and [WO₆] clusters.

clusters								
Sample	Ag(6)–O5	Ag(4)–O4	Ag(4)–O7	Ag(5)–O3	Ag(5)–O8	Ag3–O1 (Å)	Ag3–O2 (Å)	Ag3–O6 (Å)
Theo.	2.246	2.37099	2.28258	2.24620	2.43018	2.591	2.562	2.369
CP	2.42362(6)	2.51999(6)	2.30985(6)	2.05456(6)	2.37393(6)	2.67697(6)	2.63517(6)	2.33158(7)
MAH-2	2.25348(5)	2.35126(5)	2.32244(5)	2.21888(5)	2.35318(5)	2.79386(5)	2.27682(5)	2.69480(6)
MAH-4	2.39369(6)	2.71156(8)	2.41226(6)	2.12652(6)	2.41000(4)	2.57570(6)	2.55227(6)	2.21854(8)
MAH-8	2.46072(6)	2.20530(6)	2.38917(6)	2.16288(6)	2.32707(6)	2.72896(6)	2.68863(6)	2.24560(8)
MAH-16	2.31630(5)	2.35991 (6)	2.42840 (6)	2.26050 (6)	2.29353 (6)	2.76323(6)	2.58850(5)	2.32075(7)
MAH-32	2.44961(5)	2.46151(5)	2.30851(5)	2.02165(5)	2.42783(5)	2.79317(5)	2.71520(5)	2.13253(6)
EI-2	2.46352(9)	2.30395(9)	2.02459(7)	2.03804(11)	2.46184(8)	2.82310(10)	2.55588(9)	1.98049(12)
EI-4	2.40978(7)	2.25895(6)	2.46737(7)	2.16120(6)	2.4300(4)	2.61504(6)	2.72054(7)	2.14849(7)
EI-8	2.35477(6)	2.40811(7)	2.36146(6)	2.17338(7)	2.52000(4)	2.66023(6)	2.58945(7)	2.23051(8)
EI-16	2.45300(7)	2.42852(7)	2.36875(7)	2.19875(7)	2.49336(8)	2.62250(7)	2.59046(7)	2.13645(8)
EI-32	2.35692(6)	2.44561(6)	2.45169(6)	2.02504(6)	2.64255(7)	2.61564(6)	2.54272(6)	2.12661(7)
FI-2	2.19496(15)	2.32461(18)	2.28294(16)	2.27447(19)	2.31994(17)	2.75457(18)	2.68478(18)	2.25800(3)
FI-4	2.335320(8)	2.28801(7)	2.31552(8)	2.28292(8)	2.59000(5)	2.70659(8)	2.15731(9)	2.14849(7)
FI-8	2.19314(15)	2.25926(17)	2.30891(16)	2.27281(19)	2.31813(16)	2.30649(15)	2.68290(17)	2.25620(3)
FI-16	2.02330(4)	2.45390(4)	2.28409(5)	2.47480(4)	2.62000(3)	2.72419(4)	2.56782(4)	2.25565(4)
FI-32	2.29948(9)	2.32809(8)	2.44771(11)	2.01564(8)	2.04842(11)	2.34053(8)	3.05384(10)	2.14566(8)

Continue Table B.2

clusters												
	Sample	W(1)-O1	W(1)-O2	W(1)-O5	W(1)-O6	W(1)-O7	W(1)-O8	W(2)-O2	W(2)-O4	W(2)-O6	W(3)-O1	W(3)-O3
Theo.	2.36406	2.39245	1.81587	1.85924	1.74179	1.75718	1.82762	1.73116	2.48354	1.83101	1.72897	2.48183
CP	2.09802	2.19519	1.50896	1.96307	1.78124	1.51399	1.91595	2.11817	2.26934	2.11953	2.16383	2.22446
MAH-2	2.05096	2.15015	1.70176	2.02610	1.73201	1.64160	1.86212	1.84543	2.26448	1.94063	1.73559	2.21318
MAH-4	2.11081	2.13035	1.55178	2.09399	1.78496	1.54000	1.90514	1.69334	2.10774	2.03312	1.88165	2.45340
MAH-8	2.13497	2.12643	1.69755	2.09523	1.72788	1.71036	1.91153	2.03947	2.11638	1.9474	1.77308	2.34427
MAH-16	2.06017	2.21008	1.63965	2.01367	1.85729	1.62373	1.87317	1.80283	2.30229	1.89563	1.78020	2.13493
MAH-32	2.00494	2.12873	1.48436	2.12113	1.83161	1.47047	1.92580	1.89108	2.32800	2.27104	2.08919	2.03696
EI-2	2.02738	2.12531	1.56107	2.39683	1.94639	1.39331	2.09455	2.19019	2.00307	1.92899	1.94425	2.47096
EI-4	1.98643	2.30368	1.59188	2.22095	1.55305	1.48000	1.78297	2.10554	1.98608	2.06241	1.90916	2.53861
EI-8	2.06081	2.17865	1.70711	2.16012	1.70294	1.36000	1.92969	1.88135	1.99394	2.06795	2.00201	2.50158
EI-16	1.94795	2.17889	1.58493	2.22452	1.69246	1.37887	2.05084	2.01477	2.53411	2.05084	2.01477	2.53411
EI-32	2.24526	2.25016	1.60881	2.08612	1.75700	1.16008	2.00148	1.89080	2.37704	2.34433	2.36640	2.36640
FI-2	2.11978	2.24576	1.67013	2.21794	1.77731	1.79350	1.83638	1.86233	2.12171	1.87103	1.82870	2.15142
FI-4	1.92644	2.28464	1.65286	2.30127	1.73927	1.26000	1.85055	2.10749	1.93333	2.35681	2.37732	2.70872
FI-8	2.20699	2.27892	1.66767	2.22918	1.74418	1.81379	1.85431	1.79292	2.21319	2.00548	1.82757	2.15034
FI-16	2.48224	2.10377	1.86476	2.14890	1.76701	1.43000	1.98462	1.71478	2.19115	1.47433	1.45374	2.13416
FI-32	1.98961	2.17564	1.61779	2.13117	1.59589	2.56135	1.96443	1.69652	2.30027	2.42951	2.72549	2.21612

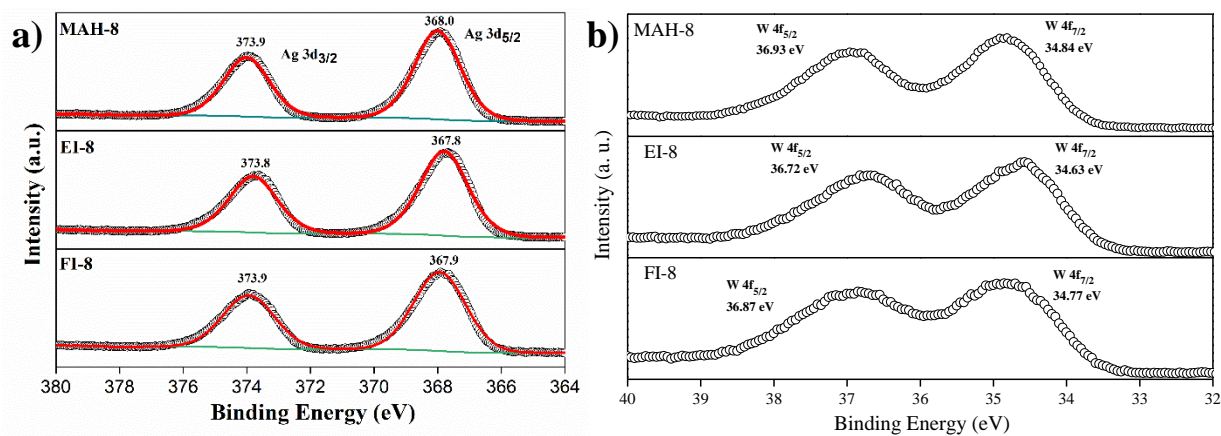


Figure B.2 High-resolution XPS spectra of a) $Ag\ 3d$ and b) $W\ 4f$ of the α - Ag_2WO_4 samples obtained by the MAH method in the synthesis time of 8 min (MAH-8), and treated by electron irradiated (EI-8) and femtosecond laser irradiated (FI-8).

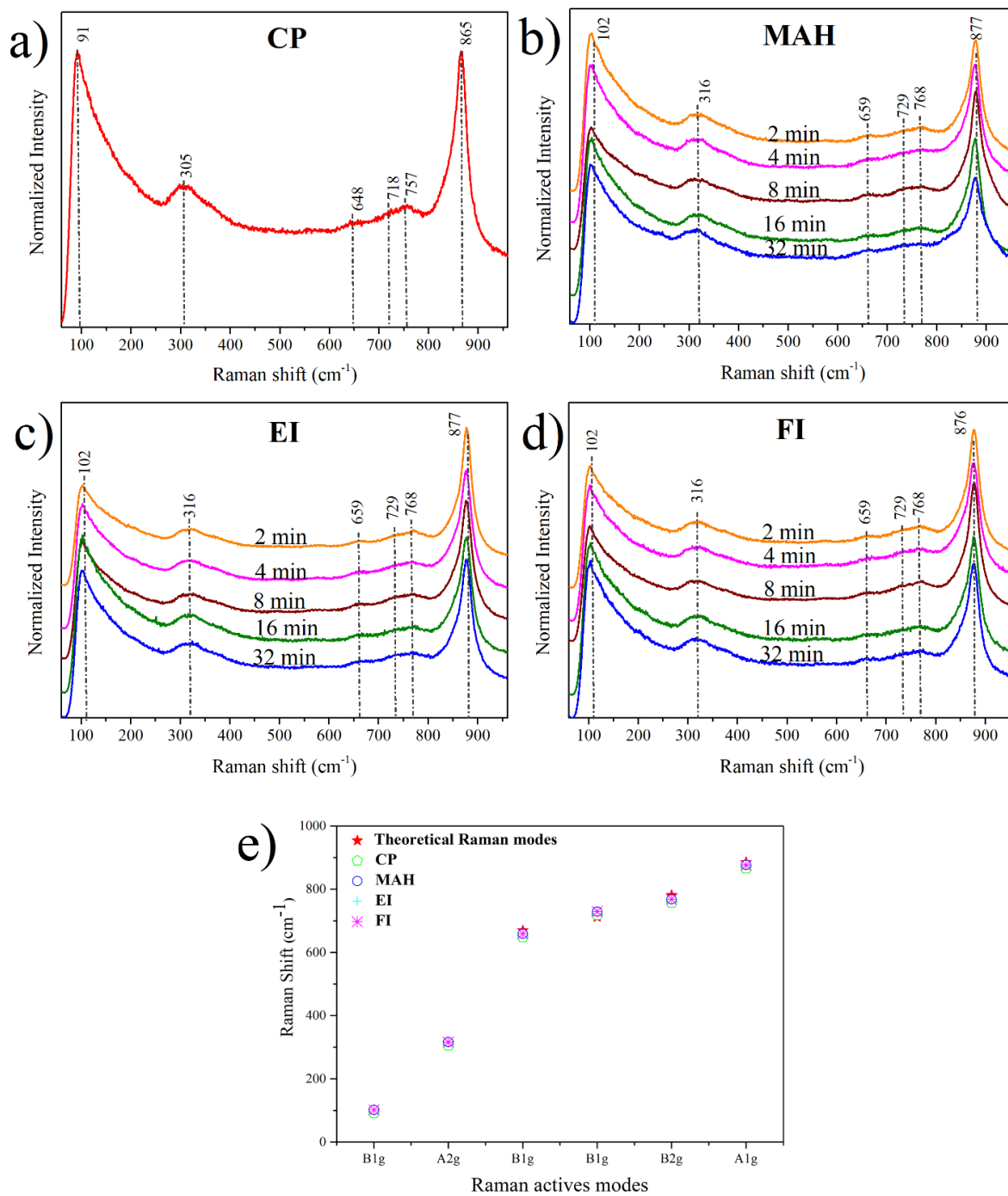


Figure B.3 Raman spectra of the α - Ag_2WO_4 samples obtained by a) CP method and treated by b) MAH method and irradiated by c) EI and d) FI. e) Comparison the theoretical and experimental Raman mode.

Table B.3 Theoretical and Experimental Raman modes (in cm^{-1}) of $\alpha\text{-Ag}_2\text{WO}_4$, compared to the literature.

Mode	This work					Literature
	CP	MAH	EI	FI	Theoretical	Turkovič, A., et al
B_{1g}	91	102	102	102	99.7	92
A_{2g}	305	316	316	316	313	306
B_{1g}	648	659	659	659	669	667
B_{1g}	718	729	729	729	712	730
B_{2g}	757	768	768	768	781	754
A_{1g}	865	877	877	876	885	884

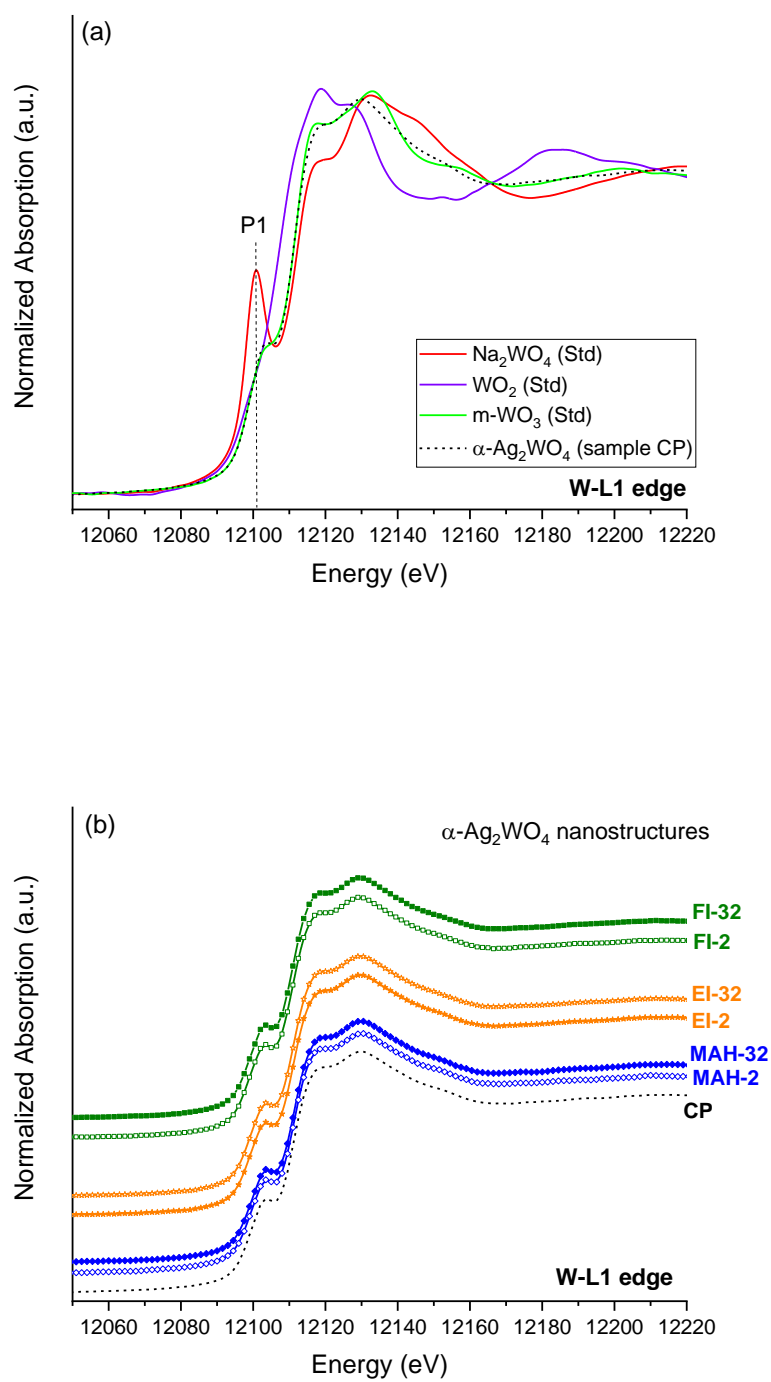


Figure B.4 XANES spectra W L₁-edge of the samples a) CP, MAH, EI, FI, and b) MAH-2 sample and patterns (Na₂WO₄, WO₂, and m-WO₃).

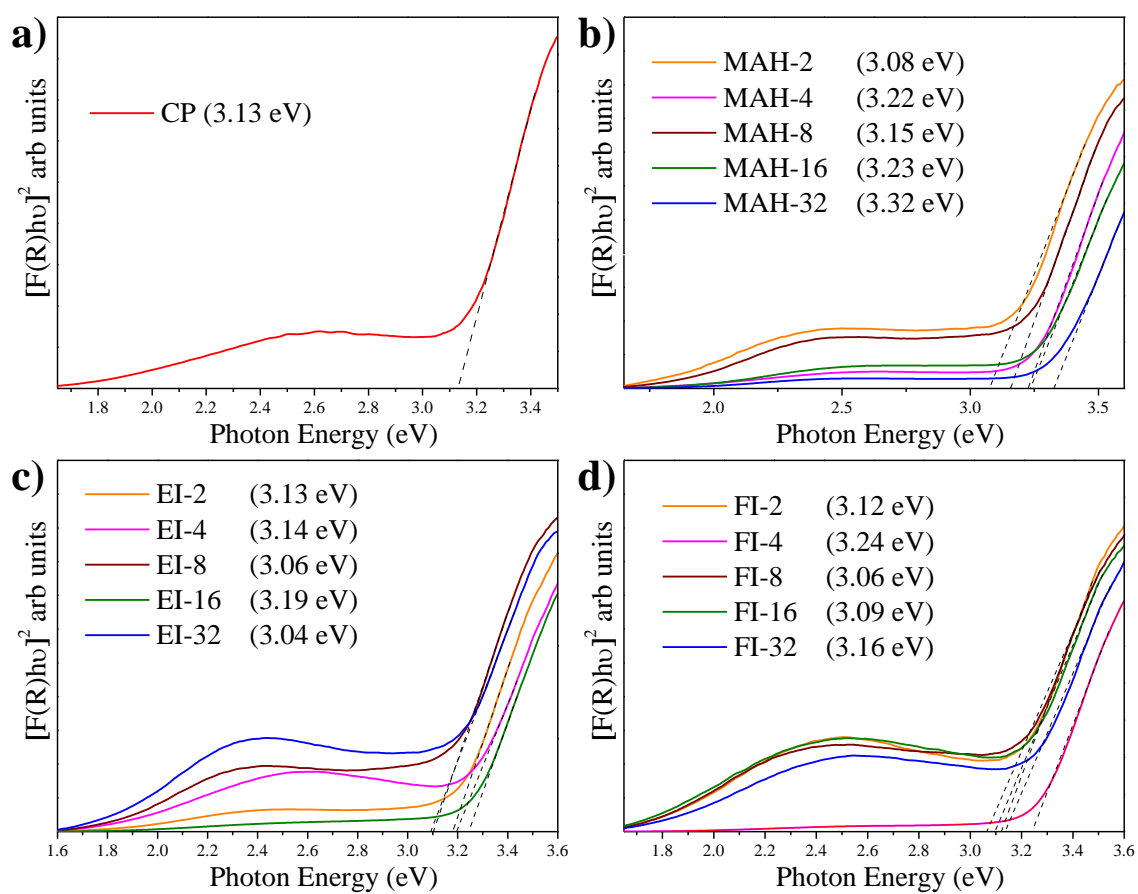


Figure B.5 UV-vis diffused reflectance spectroscopy of the α - Ag_2WO_4 samples obtained by a) CP sample and treated by b) MAH method and irradiated by c) EI, and d) FI.

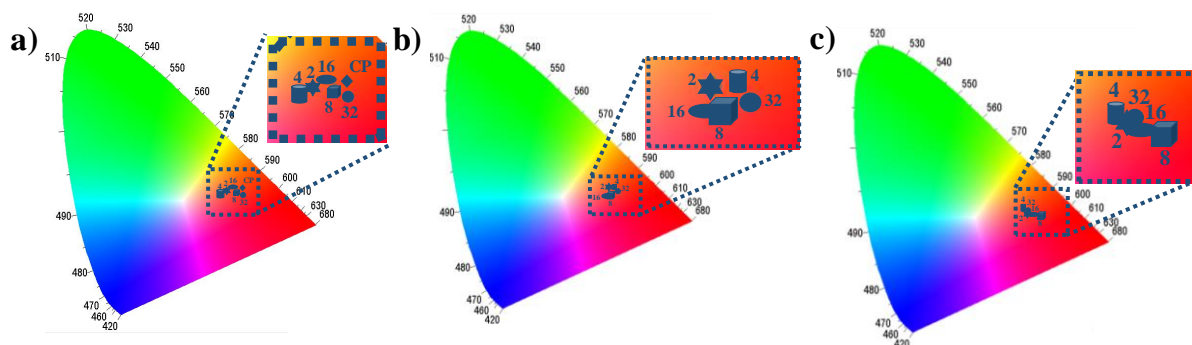


Figure B.6 CIE chromaticity diagram at the sample obtained by a) CP method and treated by MAH method at the times: 2, 4, 8, 16, and 32 min, and irradiated by b) EI, and c) FI.

Table B.4 CIE chromaticity coordinates x and y for the CP, MAH, EI, and FI samples.

Samples	x coordinate	y coordinate
CP	0.50	0.35
MAH-2	0.48	0.36
MAH-4	0.47	0.36
MAH-8	0.51	0.36
MAH-16	0.49	0.36
MAH-32	0.52	0.35
EI-2	0.48	0.36
EI-4	0.50	0.36
EI-8	0.49	0.35
EI-16	0.48	0.34
EI-32	0.51	0.35
FI-2	0.50	0.35
FI-4	0.49	0.35
FI-8	0.54	0.34
FI-16	0.51	0.34
FI-32	0.50	0.35

B.2 - Referênces

- [1] M. Alain, M. Jacques, M.B. Diane, P. Karine, MAX: Multiplatform applications for XAFS, J. Phys. Conf. Ser. 190 (2009) 8–12. doi:10.1088/1742-6596/190/1/012034.